NOVEL APPLICATIONS OF A THERMALLY TUNABLE BISTABLE BUCKLING SILICON-ON-INSULATOR (SOI) MICROFABRICATED MEMBRANE

DISSERTATION

Robert A. Lake, Captain, USAF

AFIT-ENG-DS-15-S-013

DEPARTMENT OF THE AIR FORCE
AIR UNIVERSITY

AIR FORCE INSTITUTE OF TECHNOLOGY

Wright-Patterson Air Force Base, Ohio

DISTRIBUTION STATEMENT A. APPROVED FOR PUBLIC RELEASE;

DISTRIBUTION UNLIMITED

The views expressed in this document are those of the author(s) and do not reflect the official policy or position of the United States Air Force, Department of Defense, or the United States Government. This material is declared a work of the U.S. Government and is not subject to copyright protection in the United States.

AFIT-ENG-DS-15-S-013

NOVEL APPLICATIONS OF A THERMALLY TUNABLE BISTABLE BUCKLING SILICON-ON-INSULATOR (SOI) MICROFABRICATED MEMBRANE

DISSERTATION

Presented to the Faculty

Graduate School of Engineering and Management

Air Force Institute of Technology

Air University

Air Education and Training Command

in Partial Fulfillment of the Requirements for the

Degree of Doctor of Philosophy

Robert A. Lake, BEET, BSEE, MSEE

Captain, USAF

September 2015

DISTRIBUTION STATEMENT A. APPROVED FOR PUBLIC RELEASE;

DISTRIBUTION UNLIMITED

AFIT-ENG-DS-15-S-013

NOVEL APPLICATIONS OF A THERMALLY TUNABLE BISTABLE BUCKLING SILICON-ON-INSULATOR (SOI) MICROFABRICATED MEMBRANE

DISSERTATION

Robert A. Lake, BEET, BSEE, MSEE
Captain, USAF

Committee Membership:

Ronald A. Coutu, Jr., Ph.D.
Chairman

Brett J. Borghetti, Ph.D.
Member

Anthony N. Palazotto, Ph.D.
Member

ADEDEJI B. BADIRU, Ph.D.
Dean, Graduate School of Engineering and Management

AFIT-ENG-DS-15-S-013

Abstract

Buckled membranes are commonly used microelectromechanical systems (MEMS) structures. Recent work has demonstrated that the deflection and stiffness of these membranes can be tuned through localized joule heating. These devices were implemented into the design and fabrication of two novel device applications, a tunable pressure sensor and a steerable micromirror. A differential pressure across the membrane causes deflection, up or down, which can be measured and related to a specific pressure. By tuning the stiffness of the membrane, its pressure response is varied providing a wider range of application for the pressure sensor. A 2.0mm by 2.0mm square membrane demonstrated a 60 percent decrease in pressure sensitivity from 1.433μm/psi to 0.55μm/psi. A steerable micromirror was realized by selectively heating a single quadrant of a buckled membrane, localized heating results in membrane deflection constrained to that quadrant.

Acknowledgements

I would like to offer my sincere thanks to my advisor, Dr. Coutu for his guidance and friendship. Without his assistance, none of this would have been possible. Next, thank you to all my fellow MEMS group students, past and present. Having good friends around to bounce ideas off of and serve as a sanity check made this experience much more enjoyable. I would also like to thank the AFIT cleanroom technician as well as the crew over at AFRL and the University of Michigan LNF staff for their help with the fabrication of my devices. Finally, none of this would have been possible without the love, support, and patience of my wife and boys. Over the past three years, they have never once complained or questioned the need for the long days, late nights, or missed weekends with them and I am looking forward to making up for all that time with them.

Robert A. Lake

Table of Contents

Page

Abstract iv

Acknowledgements v

List of Figures ix

List of Tables xviii

List of Abbreviations xx

I. Introduction 1

II. Background 3

2.1 MEMS Overview 3
2.1.1 Photolithography 4
2.1.2 Surface Micromachining 6
2.1.3 Bulk Micromachining 10
2.1.4 Micromolding 13
2.1.5 Hybrid MEMS Fabrication 14
2.1.6 Device Bonding and Packaging 16
2.1.7 Plasma Etching 17
2.1.8 Reactive Ion Etching 18
2.1.9 Deep Reactive Ion Etching 20
2.2 Membrane Theory 22
2.2.1 Residual Stress 22
2.2.2 Buckling 23
2.2.3 Springs 31
2.2.4 Compliant, Bistable Mechanisms 34
2.2.5 MEMS Pressure Sensors 37
2.3 Heat Transfer 39
2.4 Previous Work and Applications 43
2.5 Statistical Analysis Tools 47
2.6 Summary 48

III. Methodology 50

3.1 Membrane Fabrication 50
3.2 Heater Fabrication 52
3.3 Bonding and Integration 54
3.3.1 Test Structure Fabrication 55
3.3.2 Flip Bonding and Test Structure 57
3.3.3 Seperation Force Testing 58

Page

3.3.4 Epoxy Bonding 60
3.4 Membrane Testing Equipment 63
3.5 Finite Element Modeling of Buckled Membrane 66
3.5.1 Mesh Convergence 67
3.5.2 Buckling Simulation 68
3.6 Summary 69

IV. Results 71

4.1 Analytic Results 71
4.2 FEA Results 74
4.2.1 Membrane Edge Length vs. Deflection 74
4.2.2 Heater Temperature 76
4.2.3 Temperature vs. Deflection 77
4.3 Measured Results 78
4.3.1 Membrane Deflection vs Membrane Edge Length Measurement 78
4.4 Buckled Membrane Stiffness Measurement 79
4.5 Tunable Pressure Sensor Measurements 80
4.5.1 Deflection vs. Pressure 80
4.5.2 Deflection vs. Temperature 82
4.5.3 Deflection vs. Pressure and Temperature 86
4.5.4 Pressure Sensitivity 93
4.5.5 Volume Actuation 97
4.6 Bonding and Integration Results 102
4.6.1 SU-8 Bonding Results 102
4.6.2 Etch Resiliency of Cross-linked SU-8 103
4.7 Multidirectional actuator 103
4.7.1 Thermal Results 103
4.7.2 Actuation Results 105
4.8 Summary 109

V. Analysis 110

5.1 Modeling vs. Measured Data 110
5.1.1 Deflection vs. Pressure 112
5.1.2 Deflection vs. Temperature 114
5.1.3 Pressure Sensor Sensitivity 115
5.2 Bonding and Integration Analysis 116
5.2.1 SU-8 Bonding Analysis 116
5.2.2 Etch Resiliency of Cross-linked SU-8 119
5.3 Multidirectional actuator 121
5.4 Summary 122

Page

VI. Conclusions and Recommendations 123

6.1 Contributions 123
6.1.1 Tunable Pressure Sensor 123
6.1.2 Volumetric Actuator 123
6.1.3 Multidirectional Thermal Actuator 124
6.1.4 MEMS Bonding and Packaging with SU-8 124
6.2 Future Work Recommendations 124
6.2.1 Micromirror Actuator Optimization 124
6.3 Summary 125

Appendix A. 126

A-1 Heater Fabrication Process Follower 126
A-2 Membrane Fabrication Process Follower 127
A-3 Mask Fabrication Process Follower 128

Appendix B. 129

B-1 1.0mm, 1.5mm, and 2.0mm Heater Mask 129
B-2 1.0mm, 1.5mm, and 2.0mm Membrane Mask 130
B-3 Multidirectional Heater Mask 131
B-4 Spacer Assembly Method Mask 132
B-5 Pillar Mask 133

Appendix C. 134

C-1 Solvent Hood 134
C-2 Heidelberg μPG 101 Mask Writer 135
C-3 Karl Suss MJB-3 Mask Aligner 136
C-4 STS Pegasus Deep Reactive Ion Etcher 137
C-5 Anatech USA SP-100 Plasma Asher 138
C-6 Semiconductor Equipment Corp. 860 Eagle Bonder 139
C-7 Quanta 3D 200i Scanning Electron Microscope 140

Appendix D. 141

D-1 Visual Bibliography 141

Appendix E. 142

E-1 Mass-Deflection Study 142
Bibliography 143

Vita 152

List of Figures

Figure Page

1. Photolithography process showing both positive photoresist and negative photoresist. 5

2. Step by step diagram of the liftoff process. Starting with a clean silicon-on-insulator (SOI) wafer (1) a layer of photoresist is applied (2). The photoresist is patterned with a mask and UV light (3) and developed (4). A layer of metal is evaporated on to the surface providing a uniform coating (5). Finally, the unwanted metal is lifted off and remaining photoresist is removed (6). 6

3. Cross sectional view of all seven layers of the PolyMUMPS process. 8

4. Scanning electron microscope (SEM) image of a MEMS corner cube reflector fabricated using the PolyMUMPS process. 9

5. Cross sectional view of all the layers used in the SUMMiT V fabrication process. Typically MMPOLY2 is deposited directly on to MMPOLY1 to form one structural layer. 10

6. Scanning electron microscope (SEM) image of a MEMS gear chain fabricated using the SUMMiT V process. 11

7. Isotropic etching without agitation (top) and with agitation (bottom.) In each case the mask material is undercut during the etching process. 12

8. SEM image of inverted pyramid cavity as a result of anisotropic etching of silicon with potassium hydroxide (KOH). 13

9. A tall, high aspect ratio gear made using LIGA technology. 14

10. Step by step process of the LIGA process. 15

11. Step by step process of the SOI fabrication process. 16

Figure Page

12. Plasma etch process. A plasma is generated, creating ionized gas molecules. These ionized molecules diffuse to the surface of the target where they are adsorbed and chemically react. The resulting compounds desorb from the target material and are pumped away. 18

13. Diagram of a reactive ion etching (RIE) chamber. 19

14. SEM image of a high aspect ratio MEMS structure fabricated using the Bosch DRIE process. 20

15. SEM image of scalloping on the side of a pillar fabricated using deep reactive ion etching (DRIE). 21

16. Illustration of stress induced the the Si/SiO_2 layers as a result of their mismatched thermal expansion coefficients, ultimately leading to buckling upon release. 23

17. Left: A slender coumn under an axial compressive load will eventually buckle. Right: Buckled train rails as a result of thermal expansion of the metal causing a compressive load in the rail. 24

18. Matlab generation of the shape of a buckled membrane clamped on all sides under uniform compressive stress. 25

19. Membrane profile through the center of the membrane along the x-axis. The volume under the membrane can be determined by integrating this area around the z-axis. 26

20. Plot of total internal strain energy of the membrane vs. its deflection. 28

21. Plot of the internal strain energy of the membrane, the restoring force acting upon the membrane, and the stiffness of the membrane all with respect to the deflection of the membrane. 30

22. Fixed-free cantilever beam with loading force normal to the beam. 32

23. Force vs. Displacement for a spring demonstrating both positive and negative stiffness regimes. 33

Figure Page

24. Analgous "ball on a hill" representation of a bistable system. 35

25. SEM image of a MEMS fully compliant tensural bistamble mechanism. 36

26. Predicted and measured force-displacement curve of the compliant bistable mechanism fabricated by Wilcox *et al.*. 37

27. Diagram of a MEMS pressure sensor with piezoresistive elements located at the positions of highest stress along the edge of the membrane. 38

28. Revenue from the MEMS pressure sensor market from 2013 projected to 2017. 38

29. Illustration of the three methods of heat transfer. 39

30. Model of the components of heat transfer including the two-dimensional conduction within the membrane and two dimensional conduction within the gas flow developed by Bouwstra *et al.* 41

31. Nonvolatile memory cell utilizing a buckled beam. 44

32. Pneumatically coupled microvalve created with two buckled Si/SiO_2 membranes. 46

33. Illustration showing the fabrication process for the buckled membrane. 52

34. Scanning electron microscope images of the two heater designs used. The single heater design (left) is used for the tunable pressure sensor design and the multiple heater design (right) is used for the multi-directional electrothermal actuator. 54

35. Process Flow for SU-8 fabrication as outlined by Microchem SU-8 datasheet. 55

36. A representative step height measurement, using a KLA Tencor Alpha IQ Step profilometer, of an SU-8 test ring with a step height of 4.7μm. 56

Figure Page

37. (a)Optical image of fabricated bond pad consisting of a square ring measuring 2mm by 2mm with a width of 200μm. (b) Cross-sectional diagram of the fully assembled structure ready for tensile load testing. 57

38. Fully assembled mechanism for testing the seperation force of the bonded sample. 59

39. Graph of the applied force vrsus clamp displacement showing an SU-8 bonded structure that separated with approximately 1.13N of applied force. 60

40. Cross sectional diagram of assembly used for DRIE processing after bonding. 61

41. Optical microscope image of the application of epoxy to the membrane. The epoxy is applied by using a pneumatically driven syringe (left) leaving a controlled amount of epoxy in the center of the membrane (right) 62

42. SEM image of the the samples fabricated for epoxy bonding to the buckled membrane. The 300μm x 300μm x 200μm pillars are centered on a 1mm x 1mm square silicon. 63

43. Zygo interface screen showing the measurement controls, surface profile, 3D model, profile data, and optical image. 64

44. Platform for holding samples in place while applying pressurized N_2 to the back of the pressure sensor during deflection measurement with the Zygo. 65

45. Testing bench with the Zygo white light interferometer, dc power supply, and pressure regulator. 66

46. Plot of four models of different mesh size and their respective modal frequency. 68

47. Example of a simulated undisturbed membrane under compressive stress resting in its unstable equilibrium point. 69

48. Example of a simulated post-buckled membrane in its stable equilibrium position. 70

Figure Page

49. Plot of the internal strain energy of a 1.5mm by 1.5mm membrane. The two local energy minimas shown represent a total buckled deflection of approximately 18μm. 72

50. Plot of total internal strain energy of a 1.5mm x 1.5mm membrane for increasing temperature from 300K to 1000K. 72

51. Plot showing the membrane deflection vs. applied temperature. A 1.5mm x 1.5mm membrane will have an initial deflection of approximately 18/mum at room temperature and increase to approximately 31μm at 1000 K. 73

52. Plot showing the relation between membrane edge length and deflection for 1.0mm, 1.5mm, and 2.0mm membranes. A thinner, 5μm thick membrane will deflect more than a thicker 6μm thick membrane of the same size due to the thicker membranes increased flexural rigidity. 74

53. Plot of the FEM simulation initial membrane deflection with respect to membrane size and mechanical layer thickness. 75

54. Plot of the measured membrane temperature vs. the applied voltage to the heater. 76

55. Cross-sectional profile of buckled membrane at different temperature applications ranging from 300K to 1200K. 77

56. Plot of the initial membrane deflection vs. its size for 1.0mm, 1.5mm, and 2.0mm square membrane with 5μm (blue) and 6μm (red) thick silicon mechanical layers. 79

57. Plot of the force vs. displacement curve of a 1.5mm membrane showing regions of positive (1) and negative stiffness (2) as well as the snap through point (3). 80

58. Plot of the deflection vs. applied pressure 5μm thick, 1.0mm, 1.5mm, and 2.0mm membranes. The 2.0mm membrane exhibits the largest range of deflection across the same applied pressures, demonstrating its lower overall stiffness 81

Figure Page

59. Plot of the deflection vs. applied pressure 6μm thick, 1.0mm, 1.5mm, and 2.0mm membranes. The 2.0mm membrane exhibits the largest range of deflection across the same applied pressures, demonstrating its lower overall stiffness 82

60. Deflection vs. temperature data for 1.0mm x 1.0mm membrane with 5μm and 6μm thick device layer. 83

61. Deflection vs. temperature data for 1.5mm x 1.5mm membrane with 5μm and 6μm thick device layer. 84

62. Deflection vs. temperature data for 2.0mm x 2.0mm membrane with 5μm and 6μm thick device layer. 86

63. Deflection data for a 5μm thick, 1.0mm x 1.0mm membrane. 87

64. Deflection data for a 6μm thick, 1.0mm x 1.0mm membrane. 88

65. Deflection data for 5μm thick, 1.5mm x 1.5mm membrane. 89

66. Deflection data for a 6μm thick, 1.5mm x 1.5mm membrane. 90

67. Deflection data for 2mm x 2mm membrane with 5μm thick device layer. 92

68. Deflection data for a 6μm thick, 2.0mm x 2.0mm membrane. 93

69. Plot of the sensitivity of a 1.0mm x 1.0mm membrane with a 5.0μm and 6.0μm thick device layer. 94

70. Plot of the sensitivity of a 1.5mm x 1.5mm membrane with a 5.0μm and 6.0μm thick device layer. 95

71. Plot of the sensitivity of a 2.0mm x 2.0mm membrane with a 5.0μm and 6.0μm thick device layer. 97

72. Plot of the membrane volume vs. temperature for a 1.0mm x 1.0mm membrane. 98

Figure Page

73. Plot of the membrane volume vs. temperature for a 1.5mm x 1.5mm membrane. 100

74. Plot of the membrane volume vs. temperature for a 2.0mm x 2.0mm membrane. 101

75. A predictor trend-line fitted to raw data from the separation testing was found to be non-zero with 90% confidence. 102

76. Plot of the average SU-8 thicknesses with respect to UV exposure time for the initial thickness, following a 5 minute plasma etch, and following a 15 minute plasma etch. 103

77. Thermal camera imaging of the multidirectional heater with 7 volts applied to the lower left heater. 104

78. Plot of the average temperatures in each quadrant of the multidirectional membrane. The "hot" quadrant (blue) increases from 301K to 434K. The "cold" quadrant increases from 301K to 317K. 105

79. Screenshot of Zygo software measuring the deflection of the multidirectional thermal actuator with no voltage applied. A top view image of the membrane is shown in (a) while a plot of the surface profile of the membrane is shown in (b). 106

80. Screenshot of Zygo software measuring the deflection of the multidirectional thermal actuator with seven volts applied. A top view image of the membrane is shown in (a) while a plot of the surface profile of the membrane is shown in (b). 107

81. Plot of the multidirectional micromirror tilt angle vs. applied voltage. 109

82. Plot of the analytic modeling (blue), FEM modeling (red), and measured deflections (green) for the 5μm thick, 1.0mm x 1.0mm, 1.5mm x 1.5mm, and 2.0 x 2.0mm membranes. 111

Figure Page

83. Plot of the analytic modeling (blue), FEM modeling (red), and measured deflections (green) for the 6μm thick, 1.0mm x 1.0mm, 1.5mm x 1.5mm, and 2.0 x 2.0mm membranes. 112

84. Plot of the pressure sensitivity vs. applied pressure 5μm and 6μm thick, 1.0mm, 1.5mm, and 2.0mm membranes. 116

85. Plot of the semi-studentized residuals versus the predictor variable of UV exposure time indicate a non-constant error variance. 117

86. A predictor trend-line fitted to the transformed data of the separation testing was found to be non-zero with 95% confidence. 117

87. Plot of the semi-studentized residuals of the transformed data versus the predictor variable of UV exposure. 119

88. Distribution plot of the residuals of the transformed data. 120

89. Plot of the thickness delta as it relates to UV exposure time. 120

90. Figure illustrating the calculation of the expected tilt angle of the micromirror based on the measured profiled of the membrane under localized heating. 121

91. Diagram of a multipillar micromirror with pillars located over the points of maximum deflection of the multidirectional actuated membrane. 125

A-1. Process follower for heater fabrication 126

A-2. Process follower for membrane fabrication 127

A-3. Process follower for photomask fabrication 128

B-1. Mask pattern for fabrication of 1.0mm, 1.5mm, and 2.0mm Heaters 129

B-2. Mask pattern for fabrication of 1.0mm, 1.5mm, and 2.0mm Membranes 130

B-3. Mask pattern for fabrication of multidirectional heaters and membranes. 131

Figure Page

B-4. Mask pattern for spacer assembly. 132

B-5. Mask pattern for the fabrication of 300μm pillars. 133

C-1. Solvent hood used for photolithography steps and any use of solvents for cleaning. 134

C-2. Heidelberg μPG 101 direct write mask writer used for making 4" photomasks used during photolithography. 135

C-3. MJB-3 mask aligner used for exposing photoresist during the lithographic process. Exposure time is variable depending on the type and thickness of photoresist being exposed. 136

C-4. STS Pegasus deep reactive ion etcher at the University of Michigan, Lurie Nanofabrication Facility. 137

C-5. This tool is used to clean samples to prepare them for subsequent steps such as photolithography or metal evaporation. 138

C-6. This tool is used for flip bonding two samples together. It is capable of providing precise alignment, variable bond pressure, and variable temperature. 139

C-7. Quanta 3D 200i scanning electron microscope used to provide SEM images of devices. 140

D-1. Visual Bibliography 141

List of Tables

Table Page

1. Mesh element size with corresponding modal frequency and error measurement. 68

2. FEM Simulation results of initial membrane deflection 75

3. Measured values of initial membrane deflection with at room temperature with no external force applied. 78

4. Measured deflections for 1.0mm, 1.5mm, and 2.0mm membranes with 5μm and 6μm thicknesses 82

5. Deflection vs. Applied Temperature for 1.0mm x 1.0mm membranes. 83

6. Deflection vs. Applied Temperature for 1.50mm x 1.50mm membranes. 84

7. Deflection vs. Applied Temperature for 2.00mm x 2.00mm membranes. 85

8. Table of measured deflections for a 5μm thick, 1.0mm x 1.0mm membrane. 87

9. Table of measured deflections for a 6μm thick, 1.0mm x 1.0mm membrane. 88

10. Table of measured deflections for a 5μm thick, 1.5mm x 1.5mm membrane. 89

11. Table of measured deflections for a 6μm thick, 1.5mm x 1.5mm membrane. 90

12. Table of measured deflections for a 5μm thick, 2.0mm x 2.0mm membrane. 91

13. Table of measured deflection of 6μm thick, 2.0mm x 2.0mm membrane. 92

14. Sensitivity vs. Applied Temperature for both 5μm and 6μm thick, 1.0mm x 1.0mm membranes. 94

15. Sensitivity vs. Applied Temperature for both 5μm and 6μm thick, 1.5mm x 1.5mm membranes. 95

Table Page

16. Sensitivity vs. Applied Temperature for both 5μm and 6μm thick, 2.00mm x 2.00mm membranes. 96

17. Volume vs. Temperature of a 5μm and 6μm thick, 1.0mm x 1.0mm membrane. 98

18. Volume vs. Temperature of a 5μm and 6μm thick, 1.5mm x 1.5mm membrane. 99

19. Volume vs. Temperature of a 5μm and 6μm thick, 2.0mm x 2.0mm membrane. 101

20. Summary of applied voltage, current, power, and temperature for the hot and cold quadrants of the multidirectional actuator. 105

21. Tilt angle vs. applied voltage 108

22. Table of membrane deflection results for analytic modeling, FEM modeling, and measured data. 113

23. Deflection ranges between 0 psi and 10 psi for all membranes. 113

24. Deflection ranges over applied temperature range for each different membrane. 114

25. Summary of the relation between membrane size and deflection for the same applied temperature. 114

26. Summary of the relation between membrane thickness and deflection for the same applied temperature. 115

List of Abbreviations

Abbreviation		Page
MEMS	Microelectromechanical Systems	1
IC	integrated circuit	3
MAP	manifold absolute pressure	3
UV	ultraviolet	4
RIE	reactive ion etching	6
LPCVD	Low pressure chemical vapor deposition	7
HF	hydroflouric	7
PolyMUMPS	Polysilicon Multi User MEMS Process	7
SUMMiT	Sandia Ultra-planar Multi-level MEMS Technology	7
CMP	chemical mechanical polishing	9
LIGA	Lithographie Galvanoformung Adformung	13
SOI	Silicon on insulator	14
IC	integrated circuit	14
CMP	chemical mechanical polishing	15
RIE	Reactive ion etching	18
DRIE	deep reactive ion etch	20
SF_6	sulfur hexafluoride	20
C_4F_8	octaflourocyclobutane	20
CTE	coefficient of thermal expansion	22
DIW	deionized water	50
BOE	buffered oxide etch	50
PEB	post exposure bake	51

Abbreviation		Page
BOE	buffered oxide etch	55
IPA	isopropyl alcohol	57

NOVEL APPLICATIONS OF A THERMALLY TUNABLE BISTABLE BUCKLING SILICON-ON-INSULATOR (SOI) MICROFABRICATED MEMBRANE

I. Introduction

Microelectromechanical Systems (MEMS) buckled membranes are used in a wide range of applications ranging from stiffness tuning, contact actuation, pressure actuation, and pressure sensing. Buckling can be an undesirable failure mechanism in some mechanical structures, however, the ability of MEMS membranes to buckle under a compressive stress provides some advantageous characteristics. A buckled membrane can be treated as a spring that will exhibit regions of positive and negative stiffness depending on its deflection due to it's internal energy. The mechanical characteristics of these membranes are demonstrated to be tunable. With the introduction of additional stress, through localized heating, it has been demonstrated that the membrane will increase it's initial deflection which, in turn, alters it's stiffness.

This research investigates two applications of these buckled membranes. The first is a tunable pressure sensor. It is demonstrated through theory and experimentation that the stiffness of a buckled membrane can be increased by applying thermal stress to the membrane. The increased stiffness of the membrane shows a diminishing effect on the membranes mechanical response to an applied pressure. The mechanical response of a typical pressure sensor is determined by physical factors such as surface area and thickness as well as mechanical properties like the Young's modulus and Poisson's ratio of the material of the sensor. These fixed values result in a single pressure response profile which is unable to adapt to its environment. With a tun-

able pressure sensor, the response profile can be adjusted to accommodate different environmental conditions, giving the sensor a broader range of application.

The second application is a multidirectional electrothermal actuator. By introducing a localized heat source to one quadrant of the membrane, the stress induced is kept within that local region causing a confined area of deflection. By bonding a micromirror structure to the membrane, it is shown that the tilt angle can be varied along the different axes of the membrane.

The fabrication and characterization of these membranes combined with the ability to integrate them into fully realized devices are the two keys to successful completion of this research area. Chapter II will provide detailed background information to include a overview of MEMS, fabrication techniques, related membrane theory, and previous work and related applications in the areas of buckled membranes.

Chapter III will discuss the fabrication of the devices studied in this research including the membrane fabrication, heater fabrication, and bonding and integration of the devices. Additionally, a description of the tools used for measuring and testing is given followed by a discussion on modeling simulation techniques used for this research.

Chapter IV presents the results of simulation and measurement of the membranes and Chapter V provides detailed analysis of those results and how they compare to theory. Finally, the conclusions and recommendations are provided in Chapter VI. A description of the contributions provided by this research is provided followed by recommendations for future work relating to buckled membrane applications.

II. Background

This chapter provides relevant background on the fabrication and uses of buckled membranes. The first section provides a brief introduction to MEMS to include a description of what MEMS are as well as a discussion on the basic principles of MEMS fabrication, specifically those methods used in this research. The next section covers the relevant theory related to this work such as basic spring theory as well as related topics such as bi-stability and negative stiffness. Lastly, an overview of previous work in related areas is given.

2.1 MEMS Overview

MEMS are mechanical and electrical devices that are fabricated on the micro-scale. This relatively new field came about around the early eighties and grew out of, and continues to grow with, the same technology used in the integrated circuit (IC) industry [1].

The first mass-produced MEMS devices were the manifold absolute pressure (MAP) sensor and disposable medical blood pressure sensor, which both hit the market in 1982 [2]. Since then, MEMS technology has undergone rapid growth and maturation. MEMS devices are found in many commercially available products today with an estimated market value at $7 billion [3].

In order to fully understand how MEMS devices function, a basic understanding of the processes used in fabricating them is required. There are three common methods of fabricating MEMS structures; surface micromachining, bulk micromachining, and micromolding. The following section will provide a description of these three MEMS processing techniques.

2.1.1 Photolithography.

Photolithography is an important processing step that is used in any MEMS fabrication. This process, shown by Figure 1, is used to pattern the features of a MEMS device.

The first step of this process is the spin deposition of a layer of photoresist at a certain speed for a certain time to achieve the desired thickness. For example, S1818 photoresist will have a thickness of 1.8μm if spun at 4000 RPM for 30 seconds. Following the deposition is "soft baking" it at a specific temperature and time (e.q. S1818 photoresist is soft baked at 110 C for 75 seconds) [4]) This step removes a portion of the solvent from this layer to establish firmness [1]. When exposed to ultraviolet (UV)) light one of two things will happen depending on the type of photoresist being used. With positive photoresist, the UV light causes polymer chains to break down. With negative photoresist, the UV light causes cross-linking polymerization to occur [5]. In each case, the UV light is shown through a mask which establishes the desired pattern.

2.1.1.1 Liftoff.

Liftoff is a process for patterning a deposited material such as metal. This process illustrated by Figure 2 begins with the application of a layer of photoresist such as S1818. This photoresist has a typical thickness of 1.8μm once applied. Following the photoresist application it is patterned to remove photoresist in areas where the metal layers of the heater are desired on the substrate. The heater material is then deposited using electron beam evaporation. Due to the evaporation process, the metal is deposited uniformly across the surface with minimal side wall coating which makes it an ideal process for the liftoff procedure. Once the deposition is complete, the

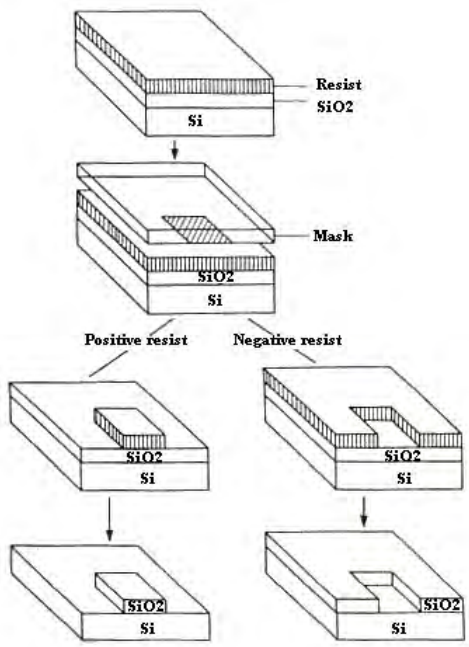

Figure 1. Photolithography process showing both positive photoresist and negative photoresist [6].

remaining metal is removed by simply lifting it off of the substrate and removing the underlying photoresist leaving only the heater.

2.1.1.2 SU-8 Photoresist.

Following the UV exposure, the photoresist is submerged in a developer solution. The developer washes away any non cross-linked photoresist. If positive photoresist is used, the photoresist that was exposed to the UV light will be developed. If negative photoresist is used, the photoresist that was masked will be developed.

SU-8 is a thick, high contrast, epoxy-based, negative tone photoresist commonly used in micromachining high-aspect ratio microelectromechanical systems (MEMS) devices and other microelectronics applications [7]. Through UV exposure and post exposure bake steps, SU-8 layers become cross-linked, robust and very resistant to standard developers and also a wide range of etching methods (e.g. O_2 plasma ash-

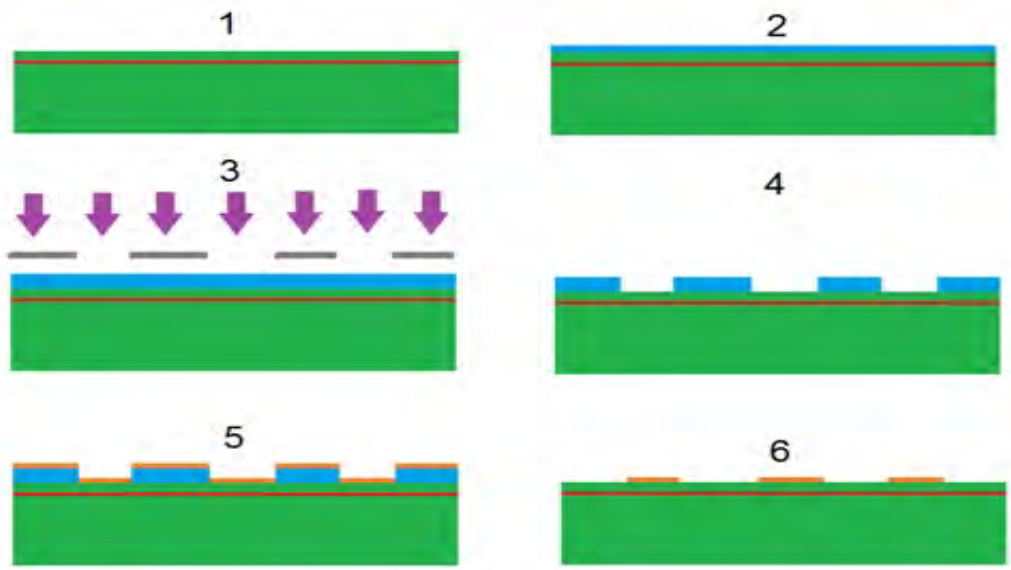

Figure 2. Step by step diagram of the liftoff process.Starting with a clean SOI wafer (1) a layer of photoresist is applied (2). The photoresist is patterned with a mask and UV light (3) and developed (4). A layer of metal is evaporated on to the surface providing a uniform coating (5). Finally, the unwanted metal is lifted off and remaining photoresist is removed (6).

ing, reactive ion etching (RIE), corrosive chemistry etches, etc), thus making SU-8 an excellent masking material during fabrication and adhesive material when assembling and packaging MEMS devices. The exposure step creates an acid and the post exposure bake thermally activates the acid to cross-link the exposed SU-8 areas [8]. The challenge is determining the optimum level of SU-8 cross-linking to maximize bond strength. SU-8 is used in microfluidics, nanoimprint lithography, and other applications that require advanced photolithography techniques. The advantages of using SU-8 include: biocompatibility, low levels of out gassing when used in vacuum, thermal stability, and highly robust films/structures suitable for harsh, corrosive environments [9].

2.1.2 Surface Micromachining.

Surface micro-machined is an additive process in which features are built up layer by layer upon the surface of a substrate [10, 11]. Surface deposition processes such

as Low pressure chemical vapor deposition (LPCVD), sputtering, or evaporation of materials are used to build the many layers of the MEMS structures. Typically these layers are very thin (0.5–4μm) and flat. After each deposition process, the previously deposited layer is profiled to the desired shape with photolithography and selective etching methods. In between the structural layers, sacrificial layers are deposited. These layers, which are removed during the final release process, provide separation between structural layers and allow for suspended devices such as beams and cantilevers. The release process involves the removal of the sacrificial layer by chemical etching. A common material for a sacrificial layer is SiO_2. It is etched with hydroflouric (HF) acid. Because of HF acid's high selectivity between Si and SiO_2 the sacrificial layer is etched while the structural polysilicon layers remain untouched. Two processes, Polysilicon Multi User MEMS Process (PolyMUMPS) and Sandia Ultra-planar Multi-level MEMS Technology (SUMMiT), are available that use these surface micromachining techniques to fabricate MEMS devices [12, 13].

2.1.2.1 PolyMUMPS.

PolyMUMPS is a commercial MEMS fabrication process which allows for up to two releasable or structural mechanical layers. The advantages of this method is that it is simple, has a rapid turn-around time (two months) is relatively inexpensive, and allows for a certain degree in flexibility with its design rules. Some disadvantages of this method are that the minimum feature dimensions and spacing between features are generally two to three microns in size, the designer is restricted to two structural layers, and all layers are conformal to the underlying topography. Because of these restrictions, there are certain limitations to design possibilities such as having to have all mechanical structures on the same layer [12].

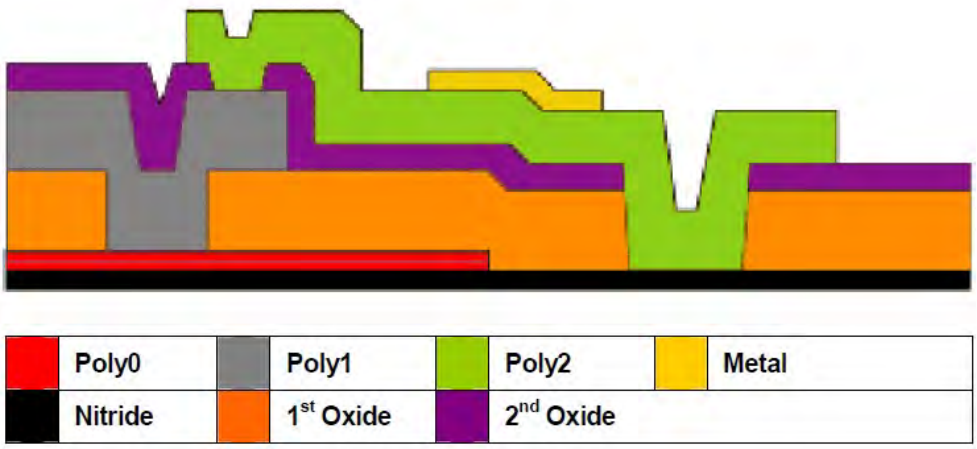

Figure 3. Cross sectional view of all seven layers of the PolyMUMPS process. [12]

The fabrication process begins, illustrated by Figure 3 with a (100) n-type doped silicon substrate. A 0.6μm thich layer of silicon nitried is deposited on the surface using LPCVD. This layer provides electrical isolation between the substrate and the MEMS devices. This is followed by a 0.5μm thick layer of polysilicon called Poly0 beind deposited and patterned. A 2.0μm SiO_2 layer called 1st oxide is then deposited and anealed for 1050°C. This annealing both dopes the polysilicon and reduces the residual film stress. The next step etches anchors and dimples into the sacrificial oxide layer. The anchors allow the subsequent polysilicon layer a way to be mechanically connected to the Poly0 or bottom layer. The dimples are etched partially through the sacrificial oxide layer which will provide a small bearing surface for the mechanical polysilicon layer in order to avoid stiction. Following the anchor and dimple etches, a 2.0μm thick layer of polysilicon is deposited known as Poly1. This polysilicon layer is patterned and a second sacrificial oxide layer, 0.75μm thick, is deposited and vias are once again etched. A third 1.5μm thick polysilicon layer, Poly2, is deposited and patterned [12]. Figure 4 shows an SEM image of a corner cube reflector fabricated using the PolyMUMPS process. This images illustrates the ability to fabricate hinges for self-assembling structures with this process.

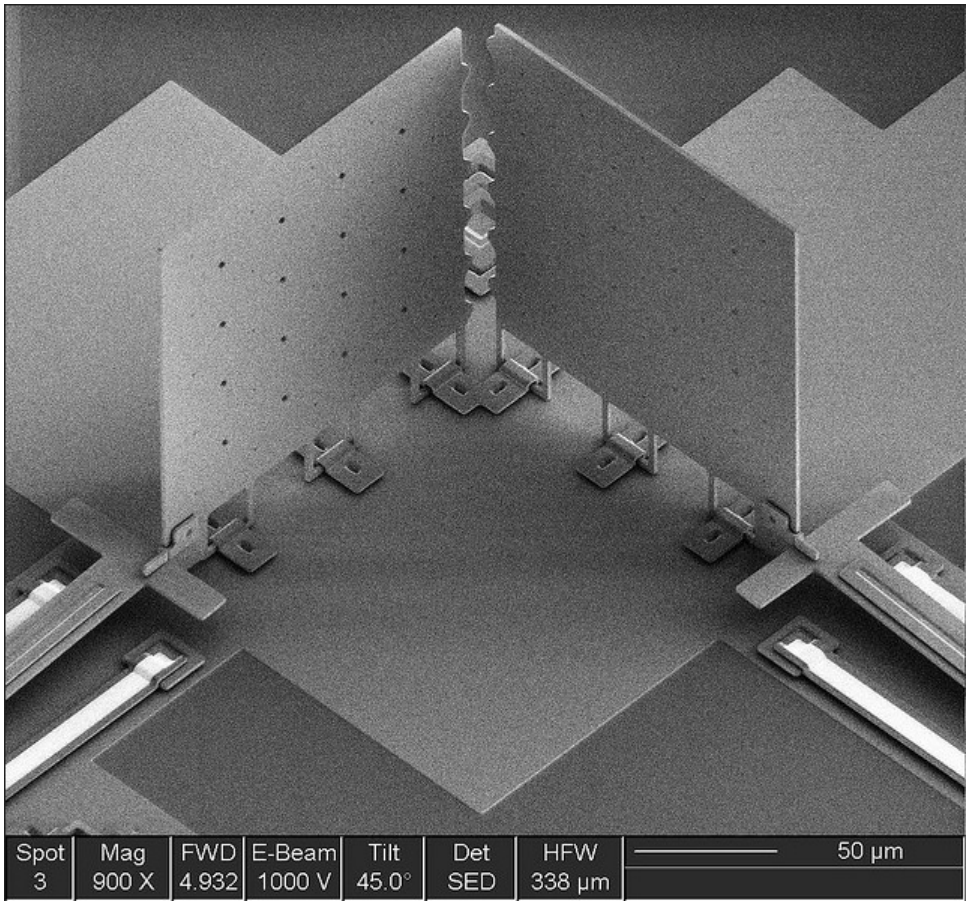

Figure 4. Scanning electron microscope (SEM) image of a MEMS corner cube reflector fabricated using the PolyMUMPS process [12].

2.1.2.2 SUMMiT V.

SUMMiT V is a MEMS fabrication process invented at Sandia National Labs. It offers several advantages over the PolyMUMPS process such as tighter tolerances, smaller feature size and spacing, (typically one half to one micron,) and an additional two releasable structural layers which allow for more complex designs that would not be possible to fabricate using the PolyMUMPS process [13]. In addition, the top two layers of this process are planarized using chemical mechanical polishing (CMP). This removes all of the conformality of the underlying layers which provides a tremendous advantage when creating structures on top of other structures. With two completely flat structures there is no risk of getting caught on each other as

they would if the structures were conformal to each other such as with PolyMUMPS. Additional benefits include the *in situ* doping of its polysilicon layers which results in minimal residual stresses in the devices upon release.

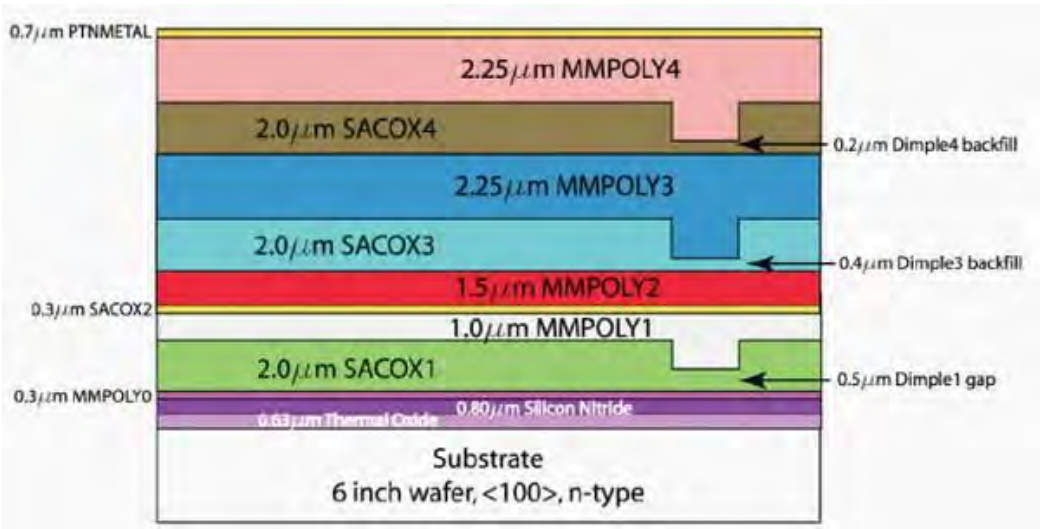

Figure 5. Cross sectional view of all the layers used in the SUMMiT V fabrication process. Typically MMPOLY2 is deposited directly on to MMPOLY1 to form one structural layer. [12]

There are, however, some disadvantages of the SUMMiT V process. For starters, the turn-around time on a V run is typically six months and is four times as expensive than a PolyMUMPS die site. Also, because of the added complexity of designs possible, the SUMMiT V process allows for minimal flexibility with its design rules.

2.1.3 Bulk Micromachining.

In contrast to surface micromachining, which is an additive process, bulk micromachining involves selectively removing portions of substrate material to form three dimensional features. Bulk micromachining is a subtractive process which does not require any additional deposition to a substrate other than masking layers for selective etching [14, 15]. There are different ways in which the substrate may be removed. Wet chemical etching involves submerging the sample in a chemical solution to remove

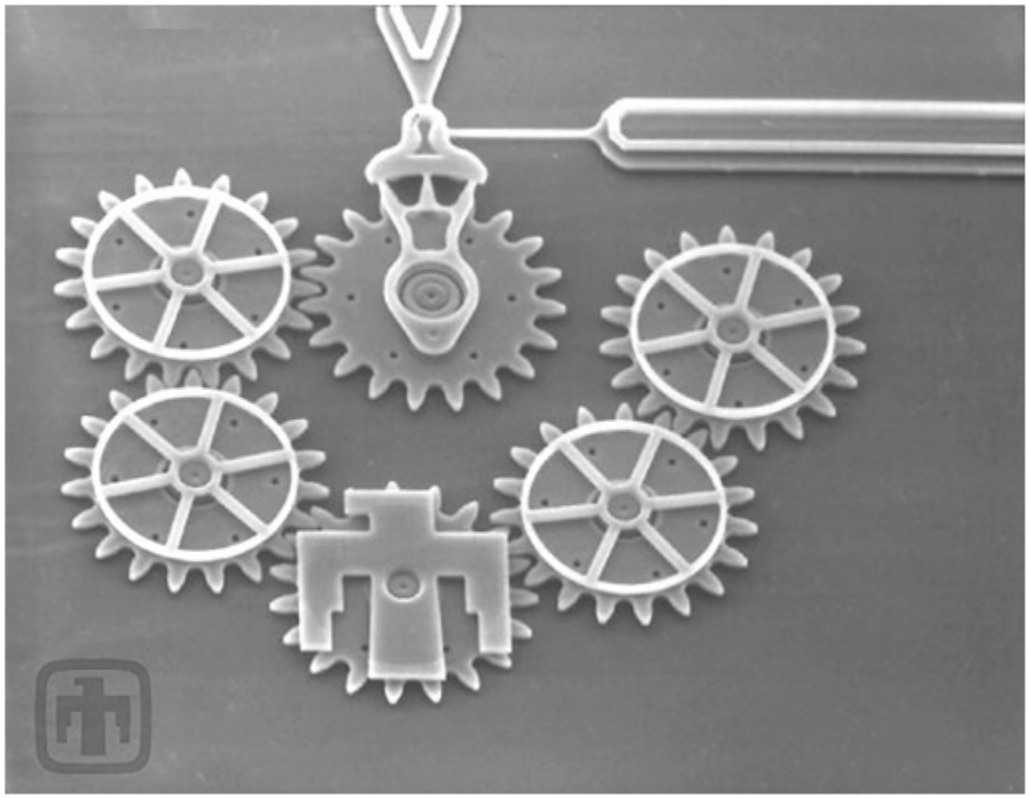

Figure 6. Scanning electron microscope (SEM) image of a MEMS gear chain fabricated using the SUMMiT V process [13].

selected regions of the substrate. This process can either be isotropic or anisotropic depending on the material being etched and the etchant.

Isotropic etching will etch material in all directions at an equal rate. This process will undercut the mask material as illustrated by Figure 7. Common isotropic etchants are hydroflouric acid (HF) for silicon dioxide and nitric acid (HNO_3). [5]

Anisotropic etching is a process where certain crystal planes of a material etch much faster than other crystal planes. This gives the etch directionality. For example with silicon, the (111) plane has more bonds per area than the (110) plane or the (100) plane. As a result, the etch rate is slower for the (111) plane. Potassium hydroxide (KOH) is a commonly used isotropic etchant for silicon. The etch selectivity between the (100), (110), and (111) planes for KOH is 100:16:1. [5]. Because of the orientation

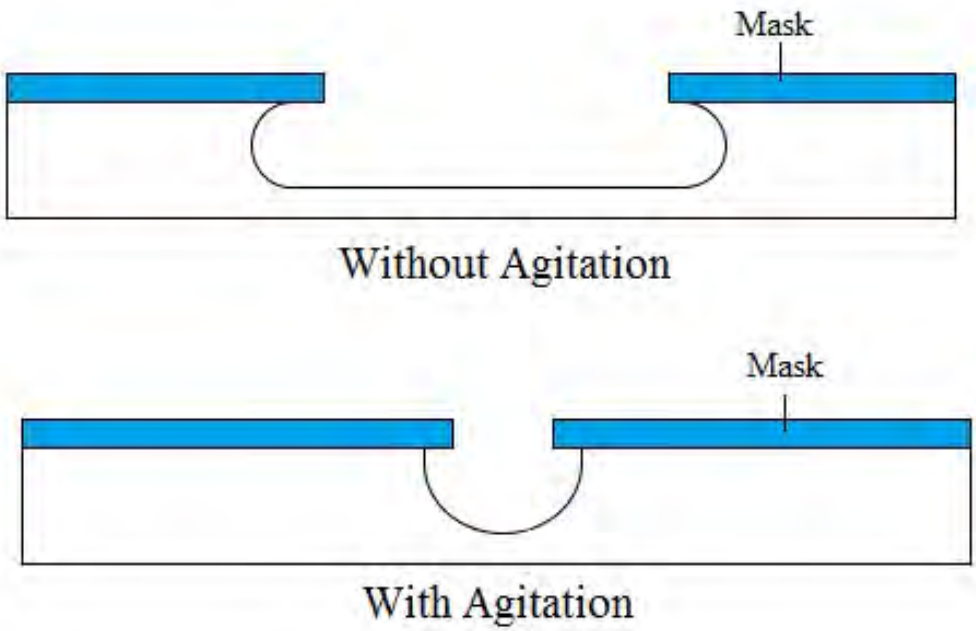

Figure 7. Isotropic etching without agitation (top) and with agitation (bottom.) In each case the mask material is undercut during the etching process.

of the planes to one another, this process results in V shaped grooves or inverted pyramids depending on the mask pattern illustrated by Figure 8.

On a (100) silicon wafer, the (100) crystal plane is parallel to the surface of the wafer. The (111) crystal planes are at 54.74° angle with respect to the (100) plane. Because of the 100:1 etch selectivity between the (100) and (111) planes, the KOH etches the (111) plane very little compared to the (100) crystal plane and the (111) surfaces remain, creating the V shaped grooves and pyramids.

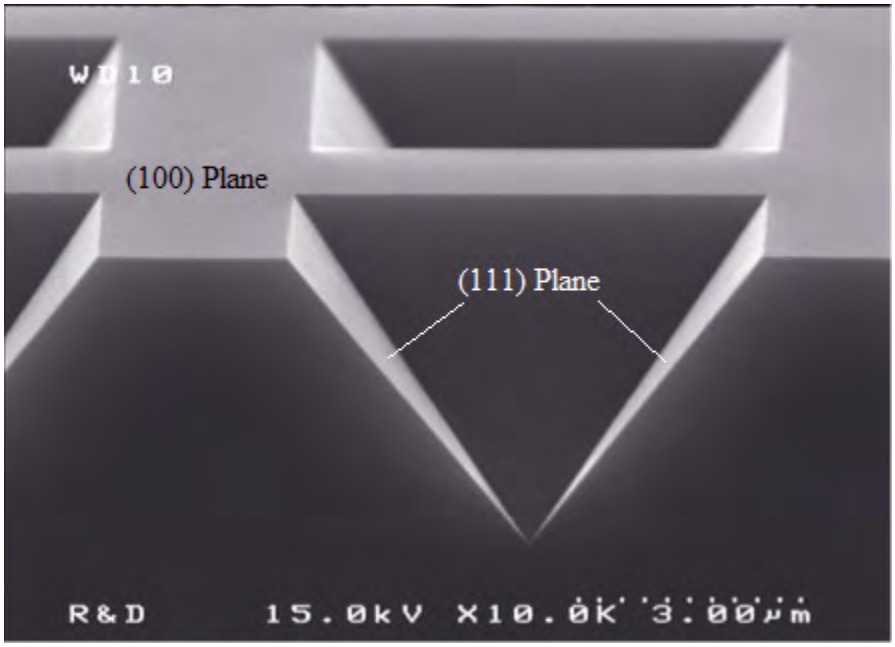

Figure 8. SEM image of inverted pyramid cavity as a result of anisotropic etching of silicon with potassium hydroxide (KOH).

2.1.4 Micromolding.

In addition to surface micromachining and bulk micromachining, there is a third type of microfabrication known as micromolding. Also known as the Lithographie Galvanoformung Adformung (LIGA), it is capable of producing microstructures with aspect ratios on the order of 100:1 with sidewall angles of 90° such as the gear shown in Figure 9 [16, 17]. The process beings by coating an electrically conductive surface with a thick layer (300μm to 500μm) x-ray resist. The resist is then exposed to x-ray radiation through a mask, allowing only certain areas of the resist to be exposed. These x-rays break the bonds in the resist polymer. The penetration depth of the x-rays into the resist is very deep and allows for the exposure of very thick layers up to and exceeding 1mm [17].Following exposure, the resist is developed which causes the exposed resist to be developed away. Metal is then electroplated on to the electrically conductive surface exposed during the development step. Finally, the remaining resist is removed leaving behind a high aspect ratio metal structure.

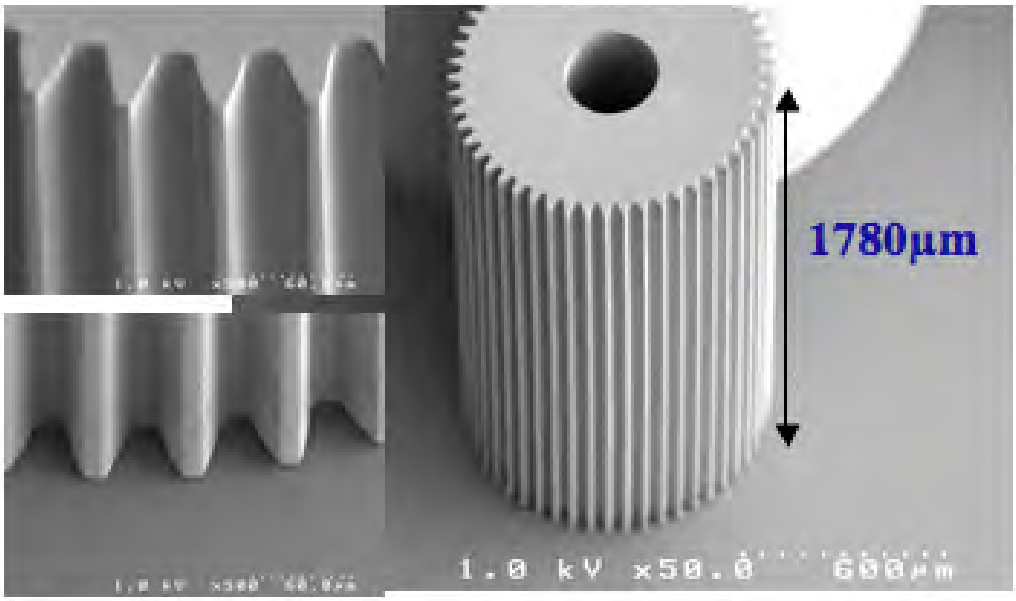

Figure 9. A tall, high aspect ratio gear made using LIGA technology [17].

Because LIGA requires special mask and a synchrotron x-ray source, the cost of this process is relatively expensive when compared to other MEMS fabrication techniques. A variation of this process reuses the fabricated metal part to create a polymer mold, eliminating the need for an x-ray radiation source each time the part is made. The entire process is illustrated by Figure 10 [18].

2.1.5 Hybrid MEMS Fabrication.

Silicon on insulator (SOI) is a method of both integrated circuit (IC) and MEMS fabrication which bulk silicon wafers are replaced with wafers that have three layers. These layers are a thin silicon layer ranging from a few nanometers to several microns thick, a thin underlying layer of an insulating material, and a thick suppor layer known as a handle. The insulating layer is commonly made of SiO_2 and is referred to as a buried oxide [10].

SOI technology offers several advantages such as CMOS compatability, excellent mechanical properties of a single crystalline surface layer, the buried SiO_2 layer pro-

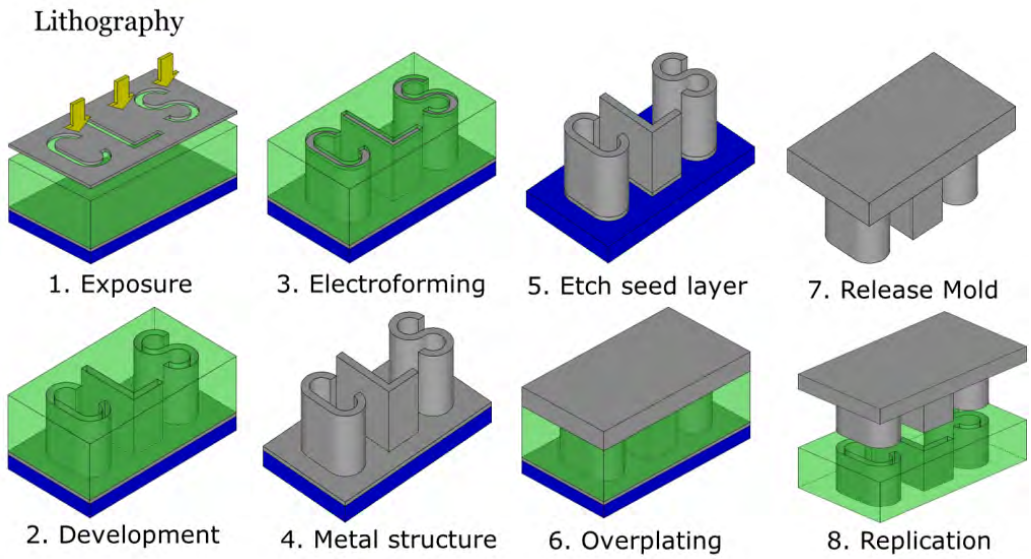

Figure 10. Step by Step process of the LIGA process. The x-ray resist is exposed through a mask (1) and developed (2). Metal is deposited on to the now exposed electrically conductive surface (3). The remaining resist is removed leaving behind a metal structure (4). The original seed layer is etched (5) and a cap is plated on top of the metal structure (6). This new structure is used as a mold for replication (7,8) [18].

vides an insulating layer as well as excellent etch stop, and high temperature operation [19, 20].

SOI wafers are fabricated by a wafer bonding process. First, an oxide layer of the desired thickness (typically 0.25 to 2 microns) is grown on a standard silicon wafer. Following the oxide growth, a second silicon wafer is bonded on to at high temperatures (1100°C) leaving the oxide layer sandwiched between the two silicon wafers. Once the bonding process is complete, one of the silicon layers is thinned down to a desired thickness by chemical mechanical polishing (CMP) [20]. This process is iullstrated by Figure 11. As a result of the high temperatures involved in the processing of SOI wafers along with the mis-matched thermal expansion coefficients between silicon and SiO_2, residual stresses will form within the SOI structure. This will be explained in further deatil in the next section.

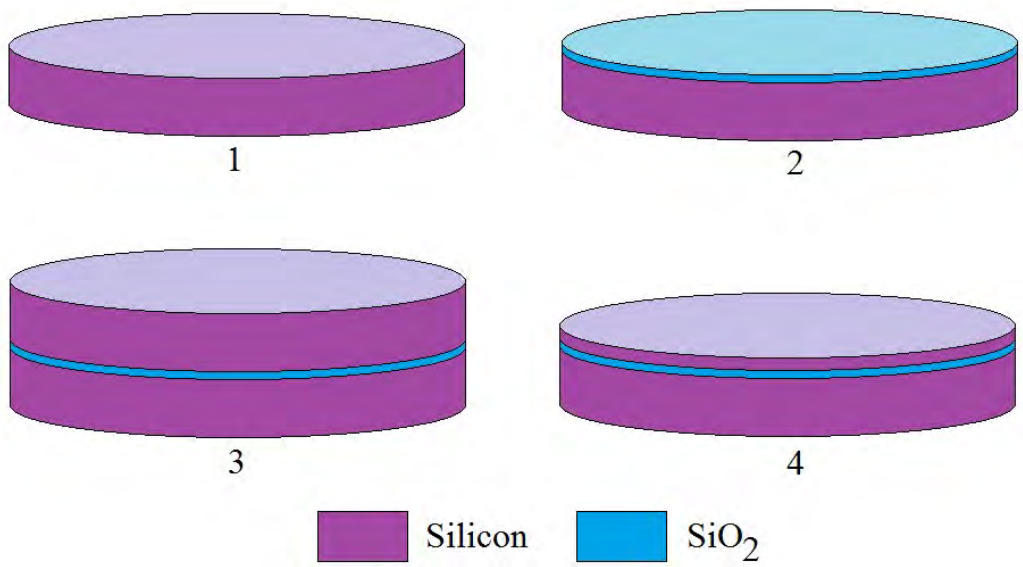

Figure 11. Step by step process of the SOI fabrication process. Starting with a plain silicon wafer (1), a thin oxide layer is grown to the desired thickness (2). Following the oxide growth, a second silicon wafer is bonded on top of the oxide layer at high temperature (3). Finally, the bonded silicon wafer is thinned to the desired thickness via chemical mechanical polishing (CMP).

2.1.6 Device Bonding and Packaging.

Many MEMS devices, especially those with complex mechanisms, require protection or operation within a vacuum or hermetic environment. Due to their fragile, movable parts or specific operation atmosphere requirements, standard microelectronics packaging technologies cannot typically be used with MEMS [21]. Wafer bonding is a common technique for packaging of MEMS devices. This technique encompasses many different methodologies such as fusion bonding [22], anodic bonding [23], eutectic bonding [24, 25], glass frit bonding [26], and polymer bonding [27]. The main difference in these methods is the material used as the bonding agent. A common trait to all of these methods, however, is the need for high pressures and temperatures to make a successfully make the bond. Some of these methods require temperatures over 1000°C to attain adequate bond strengths necessary for device packaging. These high temperatures can damage MEMS and other devices while they are being encap-

sulated or packaged [28]. Low temperature bonding methods are needed to minimize component damage due to the packaging process.

Besides its application as a masking material when forming structural device layers, SU-8 can also be used as a bonding material for packaging. The advantages offered when using SU-8 as a bonding material include: low bonding temperature, ease of processing, low cost, near hermetic seal, and conformal sealing [29]. Additionally, bonding with a patternable polymer such as SU-8 reduces residual stress in packaged micro-components, damages from high electric fields, and high-temperature processing effects [30]. Two prior research efforts have investigated using SU-8 as an adhesive material in flip-chip bonding [31, 32]. The first study, by Ochoa *et al.*, found that varying the post exposure bake (PEB) temperature of 2μm thick, 50mm x 50mm SU-8 bond pads resulted in improved bond strength. The highest bond strength was achieved using a 135C PEB with a 1-kg bonding load applied. The bond strengths, however, cannot be compared to other work since they were not quantified during this study [31]. Glauvitz *et al.* investigated SU-8 cross-linking and its effect of flip-chip bond strength by varying the hard bake time while maintaining a constant temperature of 110°C [32]. Glauvitz *et al.* discovered a loose correlation between hard bake time, cross-linking, and bond strength after testing their SU-8 bonded structures with applied tensile loads. The results showed that a hard bake time of three minutes yielded the highest separation load of 190 grams [32].

2.1.7 Plasma Etching.

Plasma etching, or dry etching, uses an ionized gas to perform the etching of a material. The plasma is first produced by applying an RF electric field to a gas. The ionized gas molecules are highly chemically reactive with the material to be etched. Flourine or chlorine free radicals are created in the plasma. These free radicals have

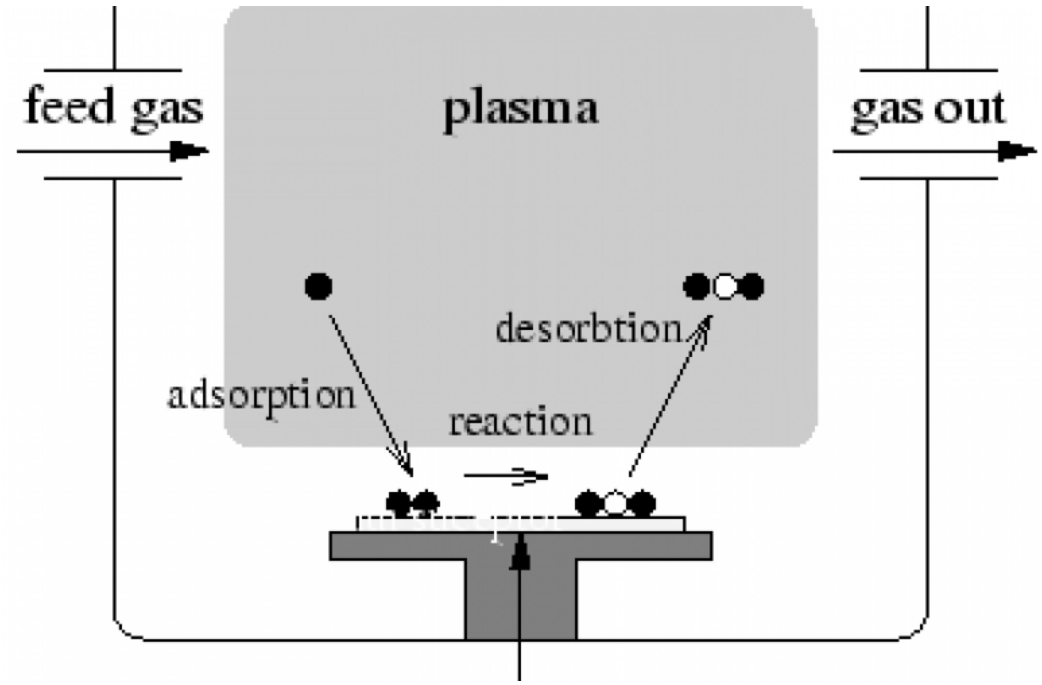

Figure 12. Plasma etch process. A plasma is generated, creating ionized gas molecules. These ionized molecules diffuse to the surface of the target where they are adsorbed and chemically react. The resulting compounds desorb from the target material and are pumped away.

at least one unpaired electron causing them to be chemically reactive. These ions are transported to the surface by diffusion. Here, they are adsorbed on the surface of the target material. This is followed by a chemical reaction between the target material and free radicals which forms volatile compounds. Finally, these compounds are desorbed from the surface. This process is illustrated by Figure 12. This method of etching typically exhibits an isotropic profile as the plasma reacts with the target material in all directions [5, 33].

2.1.8 Reactive Ion Etching.

Reactive ion etching (RIE) is a method of plasma etching which utilizes both chemical and physical etch mechanisms. The RIE reaction chamber (Figure 13) is configured so that two electrodes in the chamber create an electric field which accelerates ionized gas molecules toward the target material. These ions have sufficient

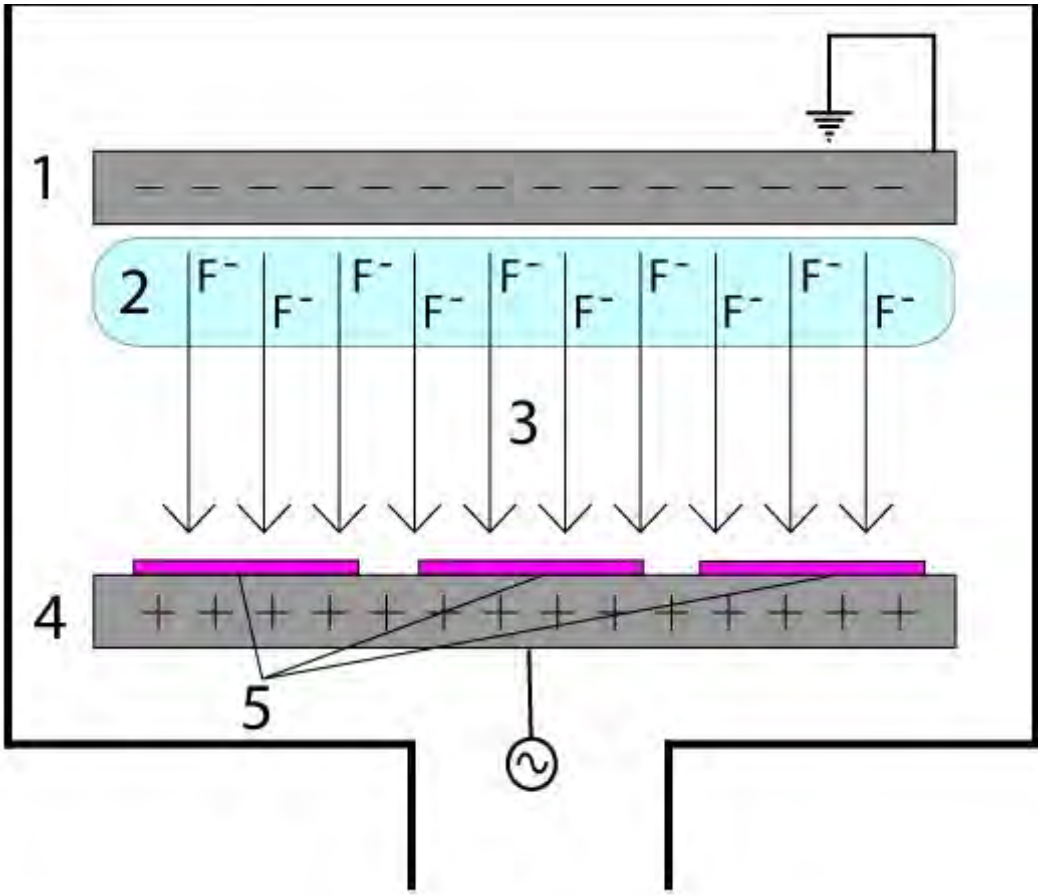

Figure 13. Diagram of a reactive ion etching (RIE) chamber. An RF field generates a plasma of ionized gas. These ions are accelerated toward the samples due to their attraction to the charge build up on the sample chuck. Additionally, free radicals within the plasma react chemically with the material [34].

energy to physically sputter atoms out of the target material by kinetic energy transfer. This process has a higher degree of anisotropy than a simple plasma etch. In addition to the physical etching process of an RIE, the chemical reaction is also taking place between reactive ions and the target material. While the RIE process offers several advantages over a plasma etch such as anisotropic etch profiles and higher etch rates, the etch selectivity suffers as a result of the physical etch process taking place which does not discriminate between target material and mask material [5, 33].

2.1.9 Deep Reactive Ion Etching.

A specialized method of reactive ion etching known as deep reactive ion etch (DRIE) is used to produce very deep, high aspect ratio structures. Etch rates of 20μm/min with high degrees of anisotropy up to 90° have been reported [35]. This process, developed by Robert Bosch, involves repeated cycles of shallow etches. In the case of silicon, sulfur hexafluoride (SF_6) is used as the active gas for the plasma etches of the silicon substrate. In between these shallow etch cycles, a passivation layer is deposited on all of the exposed silicon. This polyymer passivation layer results from the silicons reaction to octaflourocyclobutane (C_4F_8) and protects the sidewalls from the isotropic etch of the SF_6.

The passivation layer on the bottom of the trench is selectively removed by the vertical ion bombardment, while leaving the sidewalls intact. Once this protective layer has been removed from the bottom of the etch, the SF_6 begins to isotropically etch the freshly exposed silicon at the bottom and the entire process repeats itself over again until the desired depth has been reached [33, 36]. This process is illustrated in Figure 14.

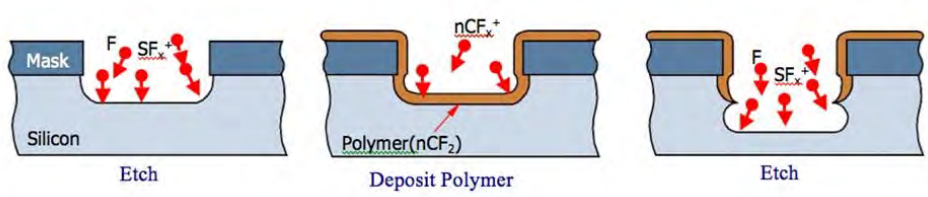

Figure 14. SEM image of a high aspect ratio MEMS structure fabricated using the Bosch DRIE process [37].

Throughout the DRIE process scalloping is created along the side walls of the cavity as shown in Figure 15. This is due to the fact that for each time the etch cycle is repeated, a new layer of unprotected sidewalls is exposed to the SF_6 plasma. Due to the methodology of the DRIE process, this scalloping is unavoidable, however the

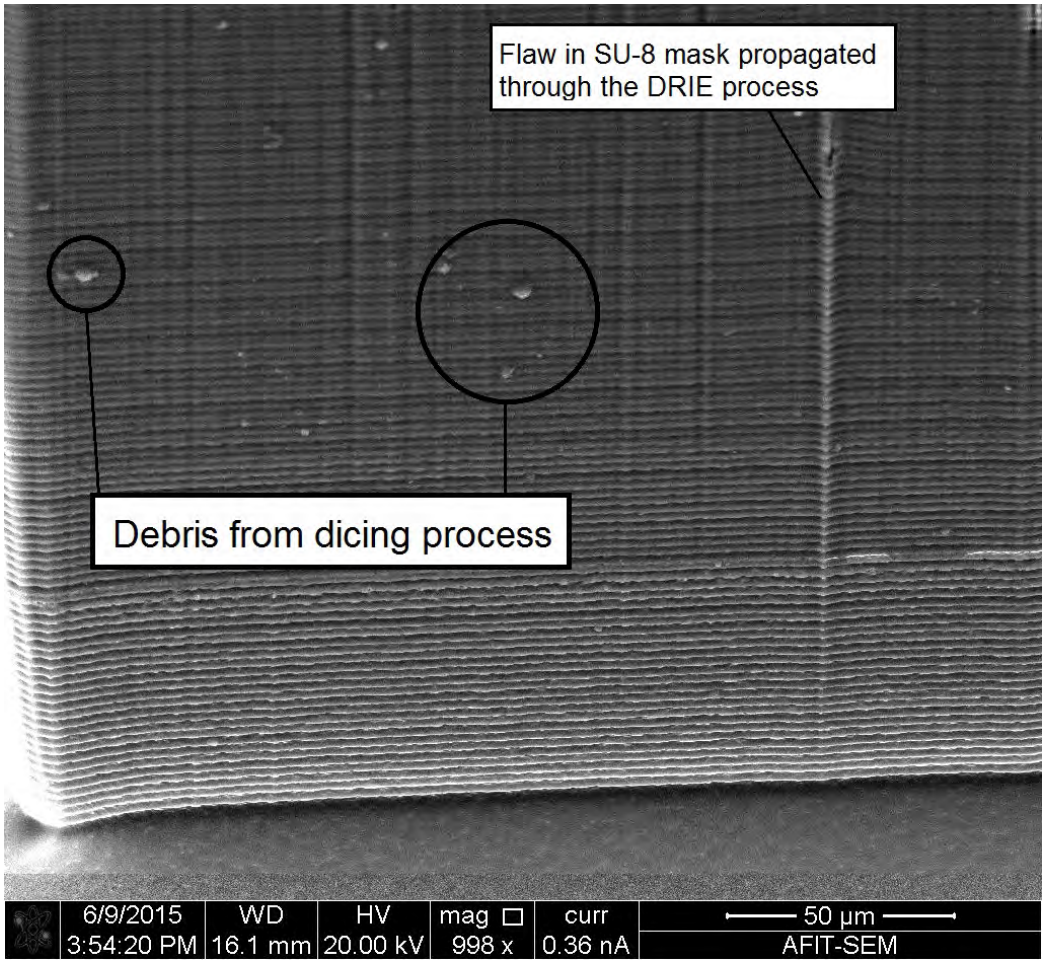

Figure 15. SEM image of scalloping on the side of a pillar fabricated using deep reactive ion etching (DRIE).

size of these scallops can be controlled by adjusting the process parameters. Scallop depth is most prominently affected by etch cycle time [38]. Shorter etch cycle times will result in smaller scalloping and smoother sidewalls at the expense of overall etch rate.

2.2 Membrane Theory

Microfabricated buckled membranes are the heart of this research effort. The goal of this section is to provide a basic understanding in the relevant theory of the mechanisms used in this effort. This will include an overview of the basics of residual stress, buckling, springs, and compliant bistable mechanisms.

2.2.1 Residual Stress.

In thin films, stress develops between layers for several reasons. The primary cause of this stress is due to a mismatch of thermal expansion coefficients and growth procedure [39]. When a thin film is deposited on a thick substrate at elevated temperature and subsequently cooled and operated at an ambient temperature, the difference between the coefficient of thermal expansion (CTE) (α) of the silicon (2.5x10^{-6}/K) and silicon dioxide (0.55x10^{-6}/K) [40, 41].

The strain in a film can be found by applying equation (1) [42],

$$\epsilon = -\Delta\alpha(T_2 - T_1) \tag{1}$$

where ϵ is the strain, $\Delta\alpha$ is the difference in thermal expansion coefficients between the two materials, and T_1 and T_2 are the deposition and cooled temperatures respectively. As the materials cool following their deposition process, they begin to contract based upon their respective thermal expansion coefficients. Because the silicon has a higher coefficient, it wants to contract more than the silicon dioxide layer. Since the two layers bonded, this results in a compressive stress being induced in the silicon dioxide layer. The silicon layer contains a minimal amount of residual stress because of its higher modulus of elasticity, crystaline structure, and greater thickness compared to

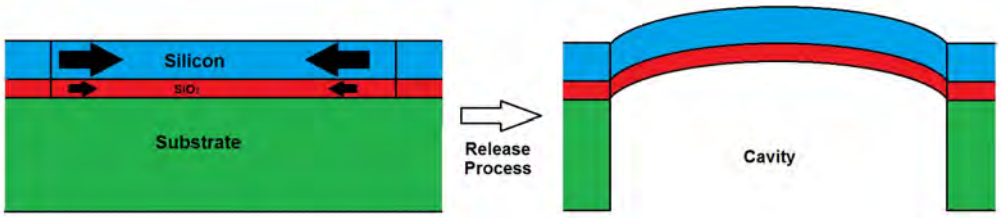

Figure 16. Illustration of stress induced the the Si/SiO_2 layers as a result of their mismatched thermal expansion coefficients, ultimately leading to buckling upon release.

the SiO_2 layer. [43, 44]. It is this compressive stress which causes the membrane to buckle out of plane as illustrated in figure 16 [45, 46].

The devices fabricated in this effort are membranes made from SOI wafers. They are fabricated by etching a cavity through the back side of a wafer usring DRIE, stopping at the buried oxide layer. This results in suspended membrane consisting of a thin layer (2μm thick) of SiO_2 underneath a 5μm or 6μm thick layer of silicon. These membranes are fixed at their boundaries and once released, buckle under residual stress, causing them to deflect either up or down to one of their two stable states.

2.2.2 Buckling.

Buckling is a failure mechanism which causes a sudden sideways failure of a structure as a result of compressive force greater than the material is capable of withstanding. With additional force the device will eventually collapse. Figure 17 illustrates a common scenario of buckling, a column under a compressive load. As the axial load on the column is increased, it reaches a critical buckling point and will bow in the direction corresponding to the lowest inertia [47].

While buckling is typically considered to be a failure mechanism for macro scale structural elements, buckled membranes are at the heart of this research. A membrane under uniform compression as shown in Figure 17 with a compressive stress greater than a critical stress will buckle out of plane without any additional load. Buckling of

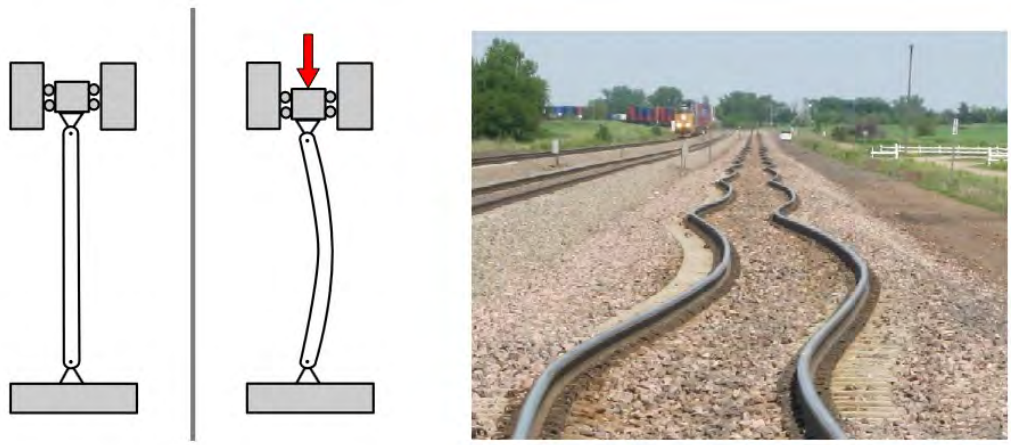

Figure 17. Left: A slender coumn under an axial compressive load will eventually buckle. Right: Buckled train rails as a result of thermal expansion of the metal causing a compressive load in the rail [48]

these membranes has been thoroughly investigated and characterized [49, 50, 51, 52]. Much of the previous research was done in an effort to determine material properties of thin films based on the deflection of the buckled membranes.

For a rectangular plate with clamped edges under pressure in two perpendicular directions, the expression for the displacement of the buckled membrane at any point (x,y) is given by equation (2).

$$w(x,y) = \frac{\delta}{4}(1 + \cos\frac{2\pi}{a}x)(1 + \cos\frac{2\pi}{b}y) \tag{2}$$

where δ is the vertical deflection at the center of the plate w(0, 0), a and b represent the length and width of the membrane [52]. The shape of the buckled membrane as described by equation (2) is illustrated in Figure 18.

Expressions for the amplitude of the deflection of the buckled plate (δ) under a uniform compressive stress (σ) in two perpendicular directions is given by equation (10) [52, 53].

$$\begin{aligned} \delta &= 0 && for:\ \sigma \leq \sigma_{cr} \\ \delta &= \pm 2.298h\sqrt{\frac{\sigma}{\sigma_{cr} - 1}} && for:\ \sigma > \sigma_{cr} \end{aligned} \tag{3}$$

where h is the thickness of the membrane and $\sigma_c r$ is the critical stress at which the membrane will begin to buckle.

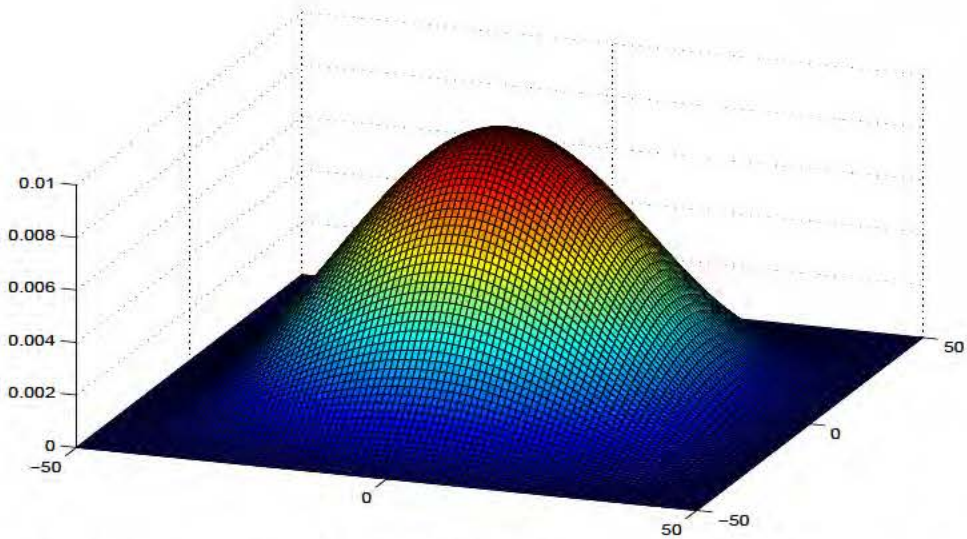

Figure 18. Matlab generation of the shape of a buckled membrane clamped on all sides under uniform compressive stress.

2.2.2.1 Volumetric Actuation.

The volume under the membrane can be determined by analyzing equation 2. Looking at a slice of the buckled membrane through the middle, illustrated by Figure 19. The height of the profile along the x-axis is given by equation 4,

$$w(x,0) = \frac{\delta}{4}(1 + \cos\frac{2\pi}{a}x) \tag{4}$$

The volume is obtained by integrating equation 4 around the z-axis as given by equation 5,

$$V = \int_0^{2\pi}\int_0^{\frac{a}{2}} xf(x)d\phi dx \tag{5}$$

where a is the length of the sides of a square membrane.

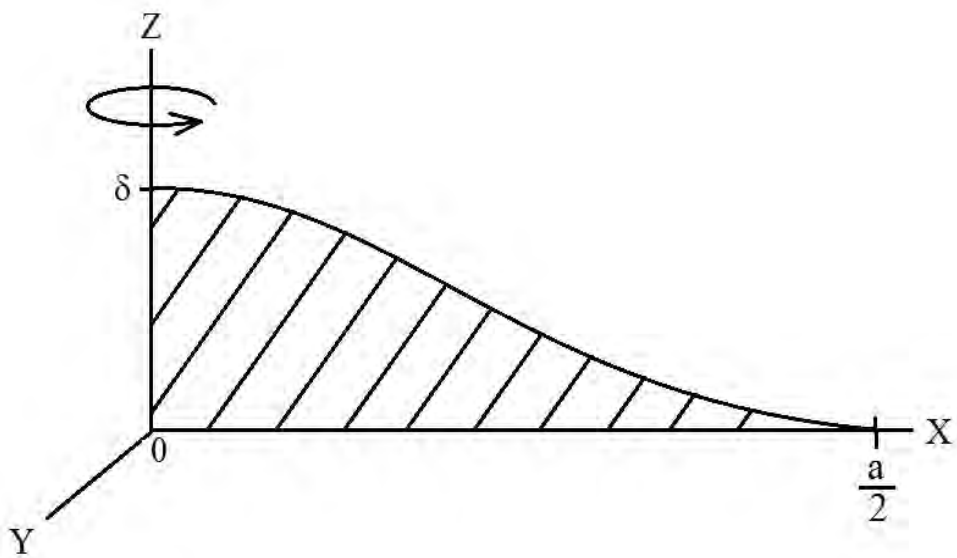

Figure 19. Membrane profile through the center of the membrane along the x-axis. The volume under the membrane can be determined by integrating this area around the z-axis.

This integration provides an equation that gives the relationship between the center deflection of the membrane, δ and its dimensions a to the volume under the membrane. This relationship is given by equation 6.

$$V = 2.34a^2\delta \tag{6}$$

The outward deflection of the membrane can be found by minimizing the strain energy of the system. From the condition for the energy to be minimum, we obtain the uniform compressive stress for first order buckling of a square membrane with clamped edges to be

$$\sigma_{cr} = 5.33\frac{\pi^2}{a^2}\frac{D}{h} \tag{7}$$

where h is the thickness of the membrane, a is the length and width of the square membrane, and D is the flexural rigidity of the plate given by equation 8-11 where E

is the Youngs modulus, and ν is Poissons ratio ([52],[53], [54]).

$$D = \frac{AC - B^2}{A} \tag{8}$$

$$A = \sum_k \frac{E_k}{1 - \nu_k^2}(z_k - z_{k-1}) \tag{9}$$

$$B = \sum_k \frac{E_k}{1 - \nu_k^2}(\frac{z_k^2 - z_{k-1}^2)}{2} \tag{10}$$

$$C = \sum_k \frac{E_k}{1 - \nu_k^2}(\frac{z_k^3 - z_{k-1}^3)}{3} \tag{11}$$

A good understanding of the behavior of these membranes can be obtained by analyzing the total internal strain energy. An expression for the total strain energy equation (12) was given by Popescu *et al.* [53]

$$U = 33\frac{Dh^2}{a^2}(\frac{\delta}{h})^4 + 100\frac{Dh^2}{a^2}(\frac{\delta}{h})^2(1 - \frac{\sigma}{\sigma_{cr}}) \tag{12}$$

Visual analysis of a plot of this equation reveals a lot of valuable insight into the behavior of these buckled membranes. Figure 20 is a plot of the total strain energy vs. deflection for three different situations. The first situation, (green,) is where the internal stress is equal to the critical stress. The second and third situations, (blue and red,) are where the internal stress is twice and three times the critical stress respectively. Looking at the line where the internal stress equals the critical stress, it can readily be seen that there is only one local minimum of the total energy which corresponds to when the deflection is equal to zero. Physically this means that the membrane is not buckled and therefore has no deflection.

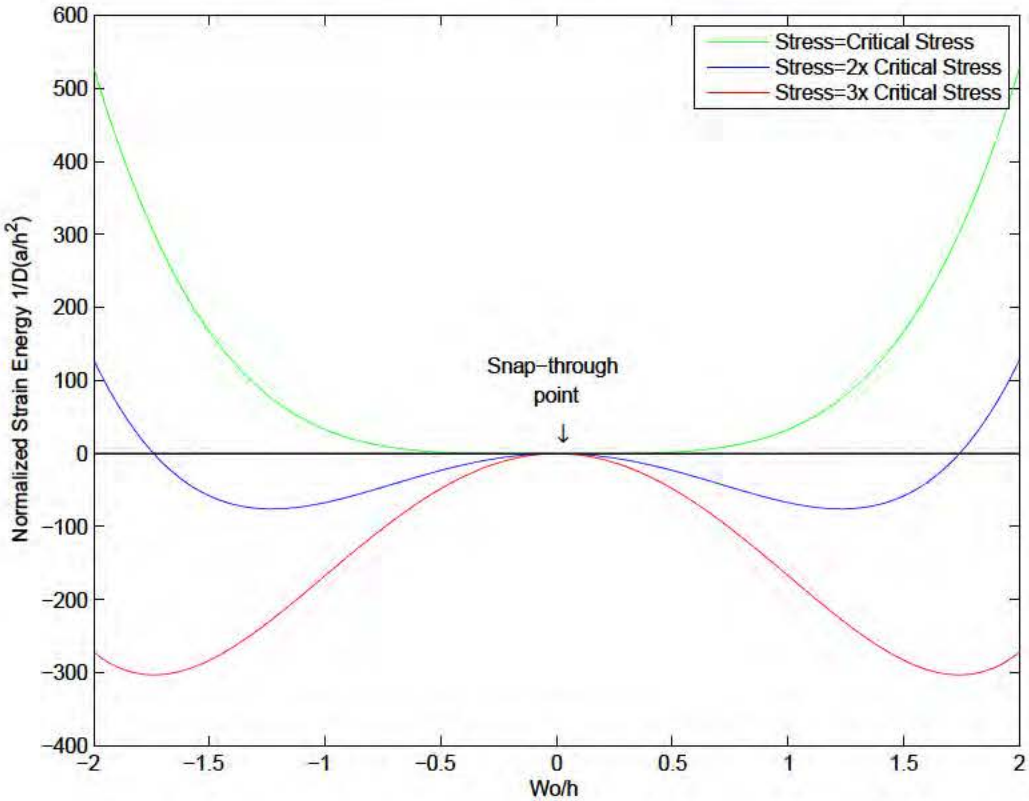

Figure 20. Plot of total internal strain energy of the membrane vs. it's deflection as given by equation 12. This plot reveals that for membranes with internal stress below it's critical stress,(green,) there is no buckling. In cases where the internal stress is greater than the critical stress, (red, blue,) the membrane will deflect out of plane and come to rest at one of its two stable positions.

The other two lines are similar in shape, but differ in magnitude. Both represent cases where the internal stress is greater than the critical stress. This reveals that there are two local minima in the total strain energy of the system, both corresponding to deflections of the membrane away from the zero point that are equal in magnitude, but opposite in direction. This is indicative of the bistability of these buckled membranes, meaning that there are two stable positions at which the membrane can rest, either deflected up or down. Note that at the point representing zero deflection, both of these curves are at a local maximum. This represents an unstable equilibrium position. The membrane will remain at this point without any external force; the slightest disturbance will cause it to move into one of its two stable equilib-

rium points. This is known as the snap-through point of the membrane. At this point the membrane is balanced in energy and wants to reach a point of lowest possible energy by deflecting either up or down. It takes very little force in either direction to cause the membrane to snap in either one of these direction and come to rest at one of its two minimum energy states. This bistability phenomenon of these membranes has been shown to be useful in many different applications.

Further analysis of this equation reveals more interesting information about the behavior of these buckled membranes. Keeping in mind that the energy is the integral of a force-displacement curve, the restoring force acting upon this membrane when it is not at one of its stable points can be found by taking the negative derivative of the energy with respect to its displacement.

$$F = -\frac{dU(x)}{dx} \tag{13}$$

Additionally, spring theory tells us that the stiffness is equal to the change in a springs force with respect to the change in its displacement as given by equation 16 [55]. By combining equation (16) and equation (13) it can be seen that the second derivative of the total internal strain energy of the buckled membrane gives an expression for its stiffness illustrated by equation (14).

$$k = -\frac{d^2U(x)}{dx^2} \tag{14}$$

A plot of the total strain energy vs. deflection, force vs. deflection, and stiffness vs. deflection is provided in Figure 21. The blue curve represents the total strain energy vs. deflection of the buckled membrane. In this case, for simplicity, just one case where the internal stress was greater than the critical stress was used. The red curve represents the force of the membrane. The three points where this curve crosses

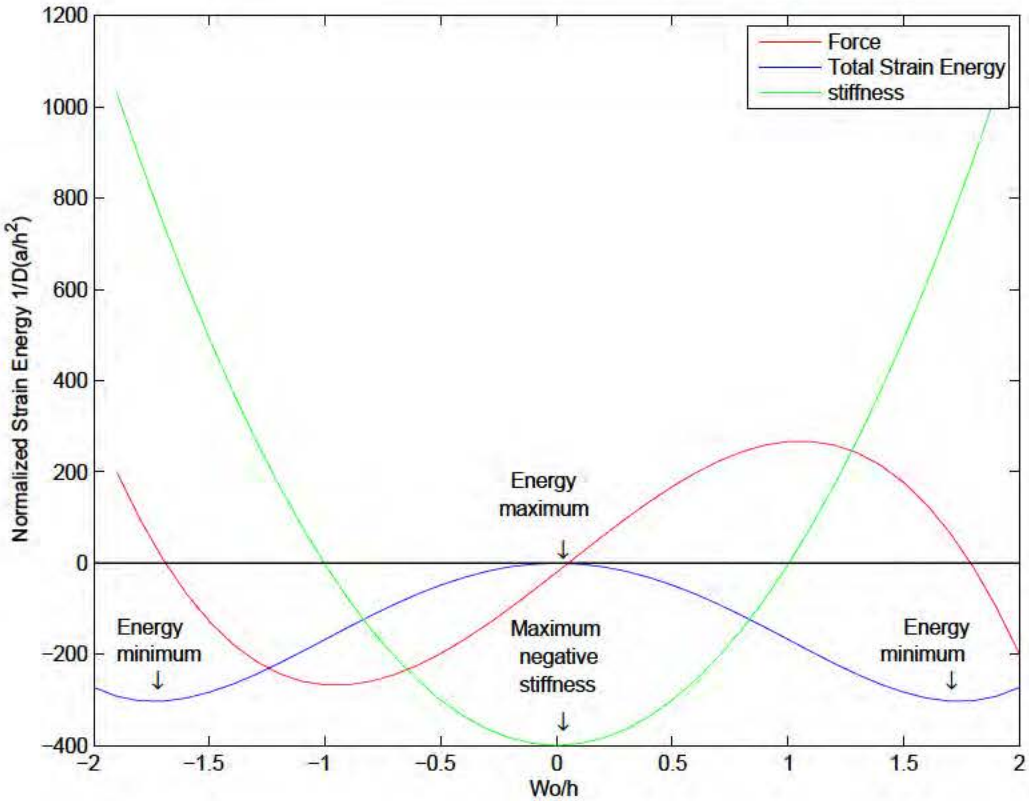

Figure 21. Plot of the internal strain energy of the membrane (blue), the restoring force acting upon the membrane (red), and the stiffness of the membrane (green) all with respect to the deflection of the membrane.

zero correspond to the local energy minima and the local maximum at the center. This is evident in test devices which remain stable when the membrane is at rest in one of those states, there is no force acting upon it. While in theory, the center represents a point of stability, in practice this would be very difficult to realize as the slightest disturbance would cause the membrane to snap through. Looking at the stiffness curve (green) it can be seen that the stiffness of the membrane has regions of positive and negative stiffness. The area of negative stiffness exists between the points where the force curve reaches its local minimum or maximum. Also noteworthy is that the negative stiffness is at its maximum right at the point where the membrane is ready to snap through to the other side. This was experimentally confirmed in [56] with the use of micro-force sensors to measure the force vs. displacement of bistable

buckled Si/SiO_2 membranes. This buckled membrane could be considered a bistable compliant mechanism.

2.2.3 Springs.

A spring is an elastic object that is used to store mechanical energy. While there may be many different types and uses of springs, they all work on the same basic principle. Most commonly, when springs are either compressed or stretched, they will display an increasing return force relating to the displacement of the spring. These springs are said to be Hookean and follow along with Hookes Law as shown by equation (15) [55],

$$F = -kx \tag{15}$$

where F is the restoring force that is exerted by the spring, k is the spring constant or stiffness of the spring, and x is the displacement of the spring. The negative sign indicates that the restoring force is exerted in the opposite direction of the displacement of the spring. In a more general sense, the stiffness is the slope of the force-displacement curve at any point. Mathematically this is represented by equation (16) [55].

$$k = \frac{dF}{dx} \tag{16}$$

Using Hookes law, the effective spring constant of a mechanical structure can be determined. For example, a simple fixed-free cantilever beam with a loading force normal to the beam as shown in Figure 22, has a moment of inertia given by equation (17) [1],

$$I = \frac{wt^3}{12} \tag{17}$$

where w is the width of the beam, t is the thickness of the beam, and l is the length of the beam.

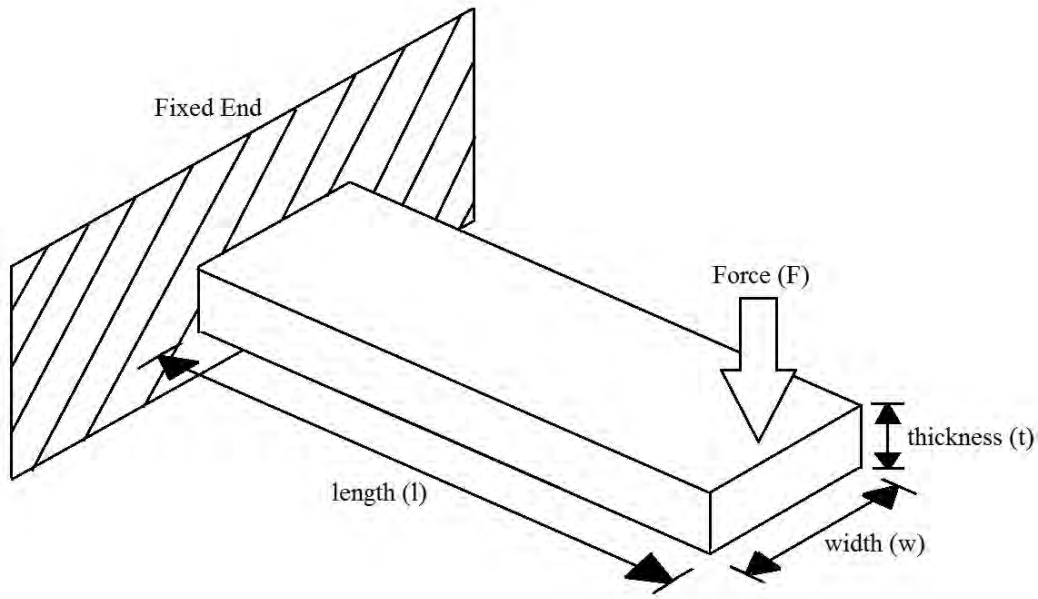

Figure 22. Fixed- free cantilever beam with loading force normal to the beam.

The displacement of the beam is given by equation (18) [2],

$$x = \frac{Fl^3}{3EI} \tag{18}$$

where x represents the displacement, F represents the applied force, E is the Youngs modulus of the material, and I is the moment of inertia, given by equation (17). Combining (17) and (18) and putting them in the form of (15), it can be shown that the stiffness (k) of a normally loaded, fixed-free cantilever beam is given as equation 19 [1].

$$k = \frac{F}{x} = \frac{Ewt^3}{4l^3} \tag{19}$$

A non-linear spring may also exhibit what is known as negative stiffness. This means that there is a reduction in the restoring force of the spring as it is displaced further. This behavior has been studied and exploited for many years. Many devices which exhibit a negative stiffness regime are pre-strained to a post-buckled state and require pre-loading [57].

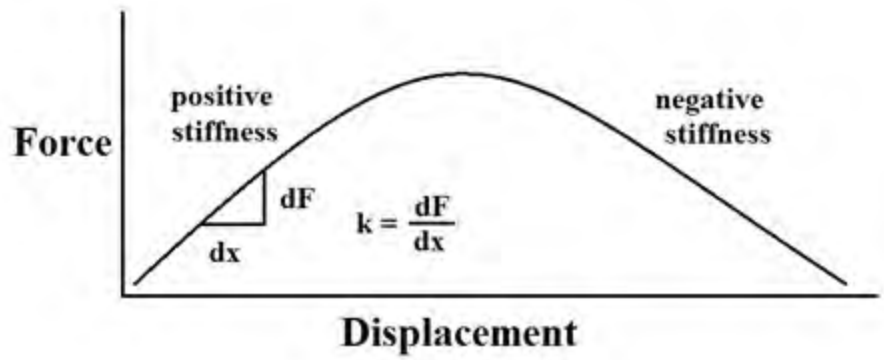

Figure 23. Force vs. Displacement for a spring demonstrating both positive and negative stiffness regimes.

One such device is the Belleville washer, or disk-spring. These devices exhibit a digressive spring force curve [58]. There are many different designs and applications of Belleville washers. One particular application is in the automotive field, in particular, high performance race cars. Based upon the configuration of the washers, by mechanically preloading them by tightening a bolt, the suspension characteristics may be finely tuned [59]. Another application of the Belleville washer is for securing high voltage electrical contacts. The Belleville washers will maintain a preload on the bolts holding the electrical contacts together. Because of this preload, the bolts will not loosen due to the thermal expansion and contraction of the bus bars under high voltage and current situations [60].

One of the main differences between the Belleville washer and the devices used in this research effort is their fabrication. The Belleville washers are fabricated to be in a post-buckled state [58]. That is to say that they are machined into their characteristic disc-cone shape, with their dimensions being specifically chosen to provide certain characteristics. The devices fabricated in this effort take advantage of residual stresses between differing materials which provide compressive stress to cause the buckling of the membranes.

2.2.4 Compliant, Bistable Mechanisms.

Micro bistable mechanisms have many possible MEMS applications including accelerometers [61], memory cells, [62], switches, [63, 64, 65, 66], relays, [67, 68, 69], and valves [70]. One of the key advantages of a compliant bistable mechanism is that no power external energy is needed in order for the mechanism to maintain its state.

A potential energy curve will only display a local minima if the mechanism has a way to store and release energy during its motion. Many devices on the macro scale simply use linear springs to store this energy. Micro-mechanisms require a form of energy storage which can be easily fabricated using standard micromachining techniques. In this case, compliant mechanisms are well suited to meet this need. The flexible segments of these compliant mechanisms store energy as they deflect [71].

There have been many designs involving the incorporation of bistable compliant mechanisms into MEMS devices. These mechanisms are analogous to how a ball behaves on a hill. Figure 24 illustrates this concept. At points A and C, the ball is at a point of its lowest energy. This is said to be stable equilibrium point, meaning that any slight deviation from this point to the left and the right, the ball will tend to fall back to this stable point. Point B represents what is known as an unstable equilibrium point. At this point, the ball is resting right on the peak since the slope of the hill at this point is flat, the ball will be at equilibrium, but will not be stable as it is at points A or C. In this case, the slightest bump in either direction will cause the ball to fall to one of the two stable equilibrium points. Since there are two stable equilibrium points, this device is said to be bistable [72].

One familiar example of a bistable mechanism is a light switch. The switch will rest in one of its two stable states and remain there indefinitely without any external input of force or energy. These two positions would be represented by points A and C in Figure 24. The switch can be placed in its other stable state only by applying

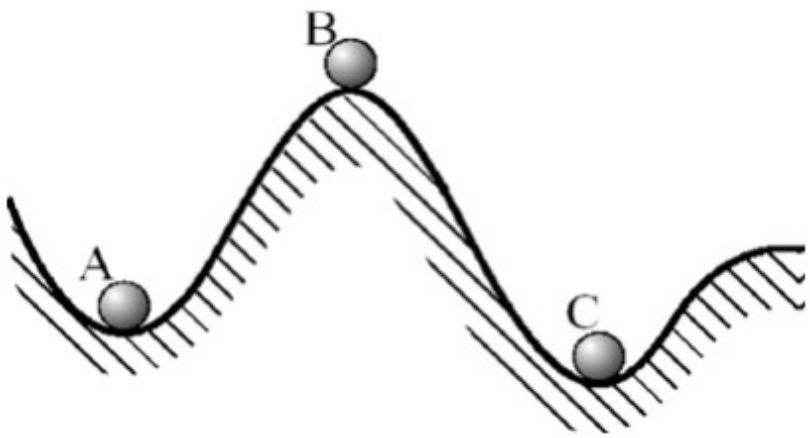

Figure 24. Analgous "ball on a hill" representation of a bistable system. Points A and C are local energy minima which are stable equilibrium positions. Point B represents a local energy maxima which is an unstable equilibrium point [72].

sufficient energy (with your finger) to overcome the internal spring mechanism of the switch and move it past its unstable equilibrium point represented by point B on Figure 24. Once the switch passes this point, it requires no additional input of energy to move the switch to its new stable equilibrium point and will remain there indefinitely without any further energy input.

Compliant mechanisms use material flexibility to transform or transmit forces, motion, or energy [73, 74]. These mechanisms inherently require the storage of non-constant strain energy. This usually results in a nonzero reaction force exerted by an actuated mechanism, even when there is no load at the output. This can be problematic in applications that require a high efficiency or high fidelity force feedback such as minimally invasive surgery. In order to mitigate this, a compliant mechanism may be statically balanced so that no effort is required in deforming the mechanism [75]. Typically this static balancing has been achieved by pre-stressing the assembly, however, this can often lead to creep and stress relaxation in the flexible members [76]. In order to obtain this static balance, a negative stiffness can be applied in order to cancel out the excess positive stiffness of the mechanism. Hoetmer *et al.* investigated the use of compressed plate springs in order to statically balance three

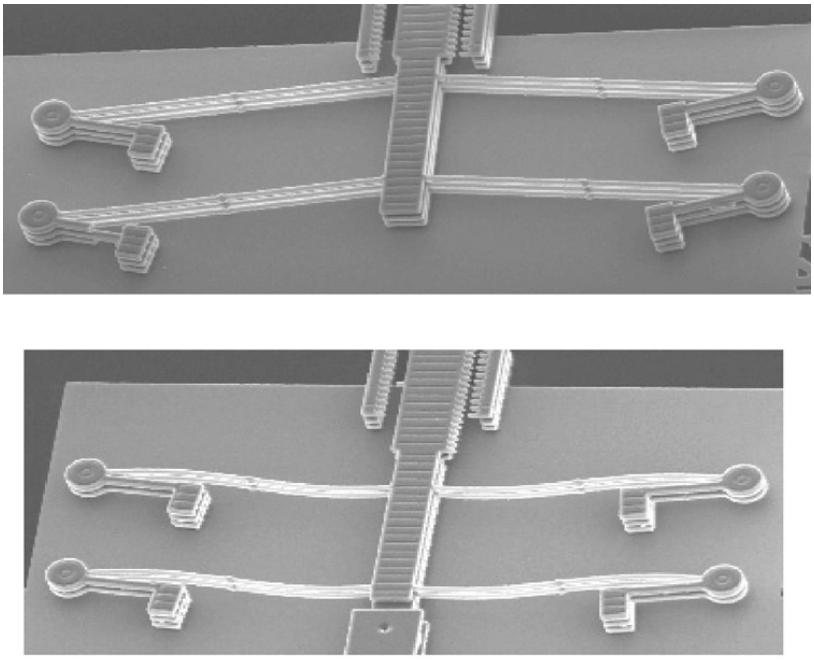

Figure 25. SEM image of a MEMS fully compliant tensural bistamble mechanism. Top: Initial fabricated position. Bottom: Second stable state [72].

different compliant mechanisms on the macro-scale. Chen *et al.* investigated the use of a constant force mechanism as well as a zero-stiffness mechanism using bistable mechanisms with negative stiffness offsets. Figure 25 shows a compliant, bistable mechanism fabricated by Wilcox *et al.* in both of its two stable positions. The force displacement curve of this device is shown in Figure 26. Note that this device has a similar force displacement curve shape to that of the buckled membranes being studied in this research. Both have regions of positive and negative stiffness as well as a "snap-through" point where the force-displacement curve crosses zero. [72]

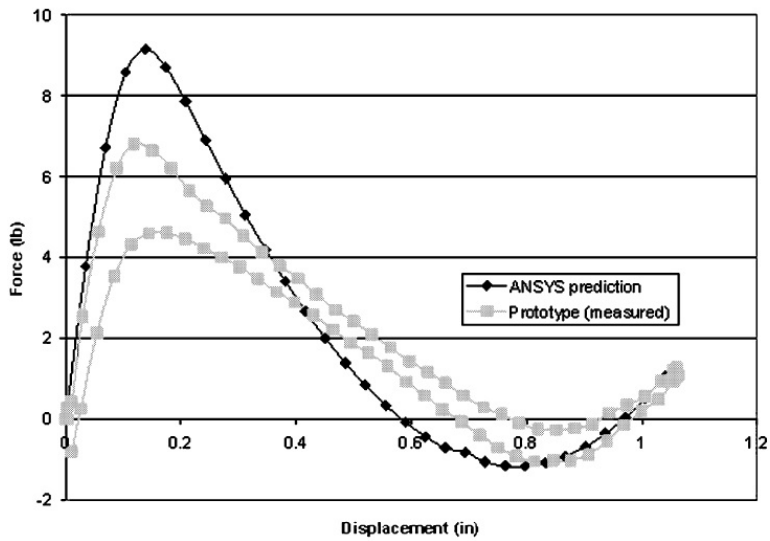

Figure 26. Predicted and measured force-displacement curve of the compliant bistable mechanism fabricated by Wilcox *et al.*. Note the similiar characteristics of this curve compared to the force displacement curve of the buckled membranes being studied in this research [72].

2.2.5 MEMS Pressure Sensors.

MEMS pressure sensors represent a mature sensor domain that is extensively utilized in electronics, environmental monitoring, medical diagnostics, automotive technology, and many other fields [77]. A typical pressure sensor consists of a silicon die with a thin membrane. Piezoresistive sensors are created by selectively doping silicon through a mask at the position of maximum stress [78, 79]. Pressure applied to the membrane causes an increase in deflection. This deflection increase causes additional strain in the areas of the piezoresistive sensors which causes a change in their resistance. These resistors are connected to a Wheatstone bridge circuit which translates the change in resistance into an electrical signal. (Figure 27 [80, 81].)

In 2013, MEMS pressure sensors surpassed accelerometers and gyroscopes as the biggest selling MEMS devices and it is predicted that the market will continue to grow (Figure 28) until at least 2017 and be worth an estimated $2.49 billion. In the automotive sector, at least 18 different applications including tire pressure, brake

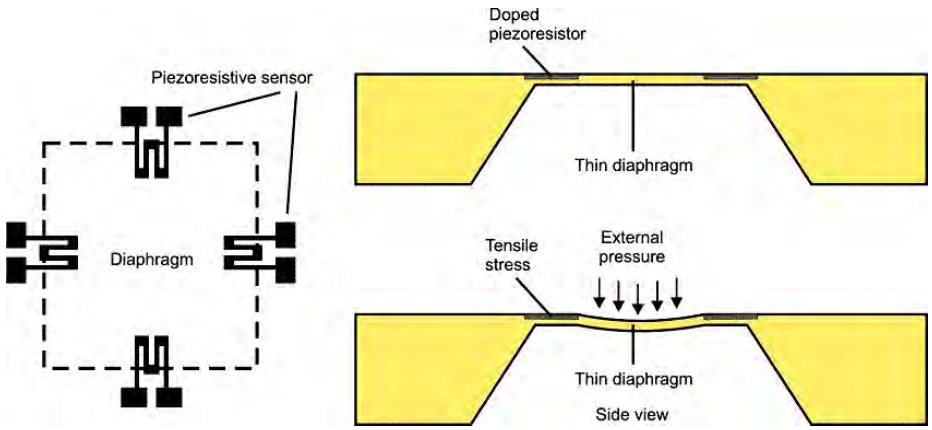

Figure 27. Diagram of a MEMS pressure sensor with piezoresistive elements located at the positions of highest stress along the edge of the membrane [82].

sensors, air bags, engine control, and exhaust gas pressure are fueling a rapid growth of MEMS pressure sensors. In 2013, the MEMS pressure sensor revenue within the automotive sector alone accounted for 75 percent of total industry revenue at $1.26 billion [83].

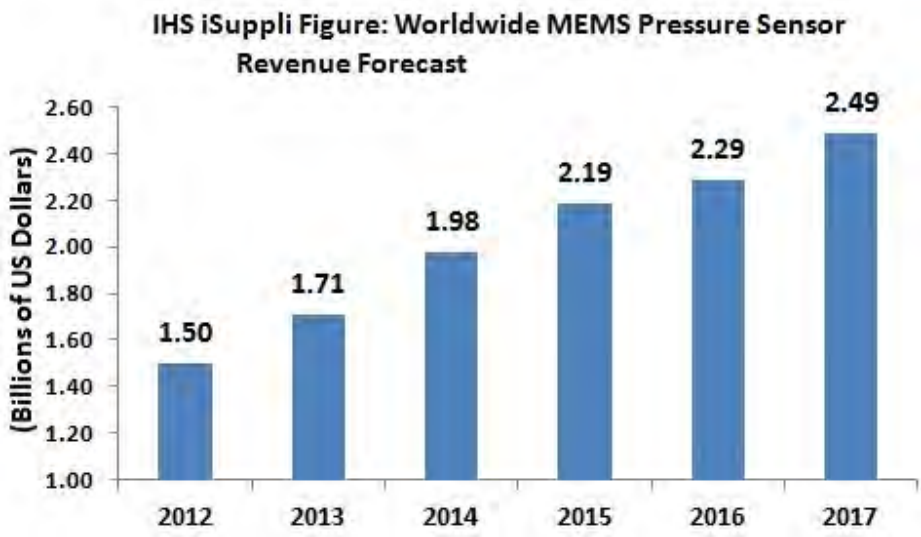

Figure 28. Revenue from the MEMS pressure sensor market from 2013 projected to 2017 [83].

2.3 Heat Transfer

Heat transfer is the flow of thermal energy due to a temperature differential across a medium. There are three primary methods of heat transfer, radiative, convection, and conduction. These three methods of heat transfer are illustrated by Figure 29.

Radiative heat transfer represents the transfer heat through electromagnetic radiation through the air or vacuum. The governing equation for the emmissive power or the rate at which energy is released per unit area E is given as:

$$E = \epsilon \sigma T_R^4 \tag{20}$$

where ϵ is the radiative emissivity of the material emitting the thermal radiation ($0 \leq \epsilon \leq 1$) [1, 84]. Some examples of radiative heat transfer would include heat from a light bulb, a fire, or the sun.

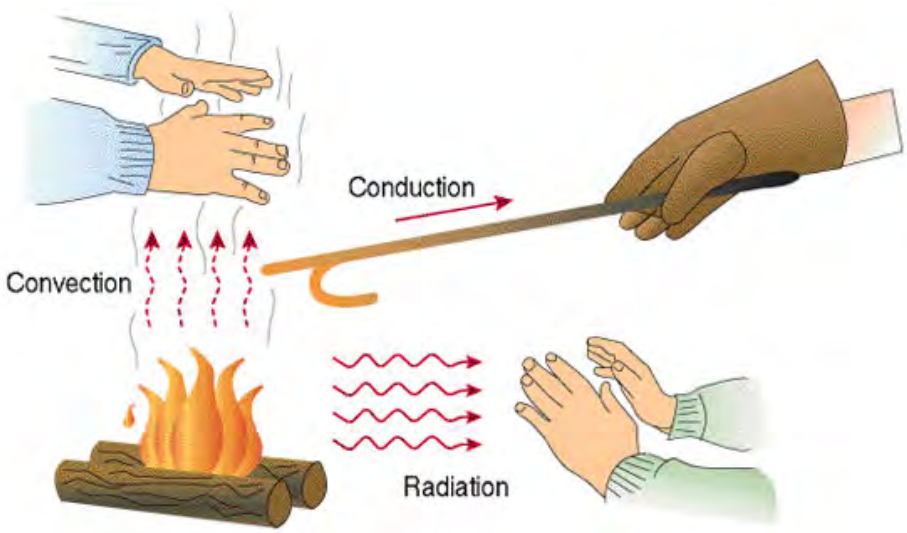

Figure 29. Illustration of the three methods of heat transfer. In this illustration, thermal energy from one source (fire) is is transferred by all three methods of heat transfer [85]

Convection involves the transfer of heat through fluid flow. A heat source can transfer its thermal energy to a surrounding fluid, such as air, which in turn may

transfer this thermal energy to another medium of a lower temperature. Examples of this include convection ovens, or a radiator in a house. The heat flux due to convection in W/m^2 is given as q_{conv}:

$$q_{conv} = h(T_s - T_\infty) \tag{21}$$

where is the convection heat flux in W/m^2, h is the convective heat transfer coefficient in W/m^{2}K, and T$_s$ and T$_\infty$ are the temperatures of the surface and fluid respectively [1, 84]

Finally, conduction is where the heat is transferred, or conducted, through a material or into another material. The heat flux due to conduction in W/m^2 is given as q_{cond}:

$$q_{cond} = -k\frac{dT}{dx} \tag{22}$$

where k is the thermal conductivity of the material, and dT/dx represents the temperature gradient across the material [1, 84]. Unlike convection, heat can be conducted within a vacuum.

To introduce additional thermal stress into the buckled membrane, it will be heated via Joule heating from a resistive heater element fabricated on top of the membrane. This heat will be conducted in to the membrane, increasing the thermal stress within it. Previous research efforts have utilized Joule heating to induce buckling in MEMS devices [86, 87] Bouwstra *et al.* utilized a resistive heater on a membrane as a sensor for detecting mass flow rates. This sensor, illustrated by Figure 30, detected a shift in the natural frequency of a thermally actuated unbuckled membrane [86]

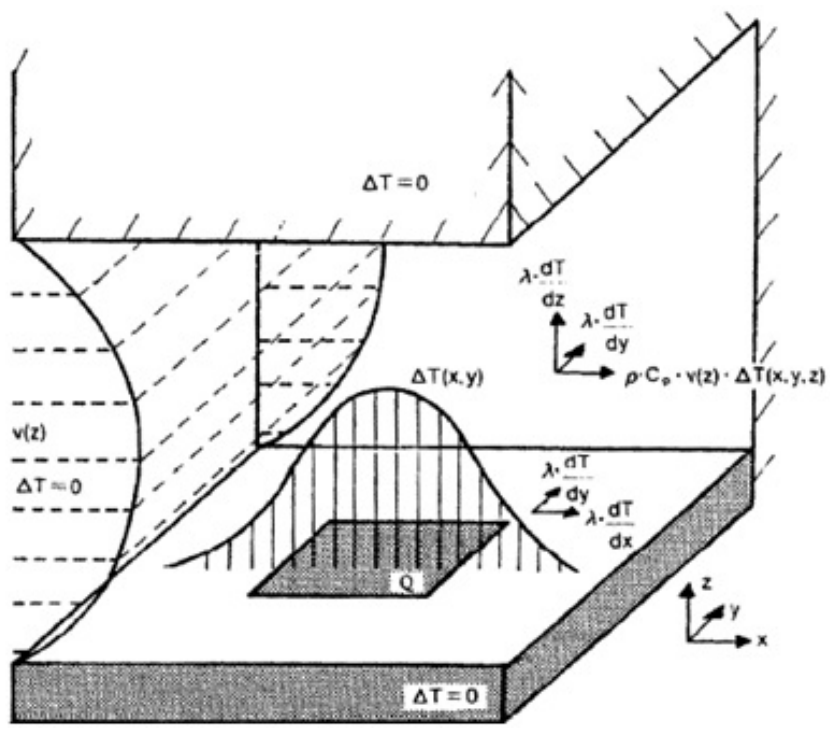

Figure 30. Model of the components of heat transfer including the two-dimensional conduction within the membrane and two dimensional conduction within the gas flow developed by Bouwstra *et al.* [86].

Bouwstra *et al.* developed a model for conductive heat transfer in a membrane with a centrally located resistor. This model is given by equation 23,

$$\Delta T_{avg} = \frac{H}{4\pi\lambda t} \tag{23}$$

where H is the heat generation per unit time, λ is the coefficient of heat conduction, and t is the thickness of the membrane. Power dissipated by the resistor is a key factor when considering the temperature across the membrane. The power dissipated by the heater is affected by the resistance of the heater given by equation 24

$$R = \rho\frac{l}{A} \tag{24}$$

where ρ is the electrical resistivity of the material, l is the length, and A is the cross sectional area of the resistor. The resistance of a meandering resistor is further influenced by increased current density around the corners of the resistor [88]. A model for the resistance of a meandering resistor is provided by equation 25,

$$R = R_s(N + (kN_{cb})) \tag{25}$$

where R is the overall resistance, R_s is the sheet resistance, N is the number of blocks in straight regions, k is the corner block correction factor, and N_cb is the number of corner blocks [89, 88]. The electrical power P dissipated by the resistive heating element is given by equation 26,

$$P = I^2R \tag{26}$$

where I is the current through the heater and R is the electrical resistance of the heater.

2.4 Previous Work and Applications

Bistable mechanisms can be applied to broader systems such as relays, valves, clips, threshold switches, and memory cells. The major advantage of these devices is that they can apply a constant force without the need for continued actuation power [90, 91]. In many of these cases, the bistable compliant mechanism has consisted of a buckled beam [71, 72, 90, 91, 92, 93, 62, 94, 95, 96, 97], while others have been based on a buckled membrane configuration [70, 98, 99].

Jin Qiu *et al.* modeled and fabricated a mechanically bistable mechanism utilizing two curved, centrally clamped parallel beams. The unique aspect of this effort is that unlike many other bistable devices, this one did not rely upon residual stress to obtain its bistability. Instead, these beams are fabricated in a curved shape. A single beam, fabricated in a bow shape, may buckle and snap through when an external force is applied to it; however it will not stay at this snapped shape when the external force is removed due to a twisting buckling mode. This essentially would make this device monostable. However, it is shown that when two curved beams are coupled together at their center, the twisting buckling modes of each beam cancel each other out, allowing the structure to behave in a bistable fashion [91, 92].

M. Taher and A. Saif developed a design for a tunable, bistable MEMS device. They used an array of electrostatic comb drive actuators to apply an axially compressive force on a long, thin beam causing it to buckle. By changing the voltage applied to the actuators, more or less compressive force is applied to the beam, which in turn has a tuning effect on the beam causing the lateral stiffness to vary [93].

Beat Hälg developed a MEMS based nonvolatile memory cell by using a bistable buckled bridge shown in Figure 31 [62]. Having two stable states makes a bistable structure ideal for digital storage applications, and being mechanical in nature makes it immune to electromagnetic fields. This, coupled with the mass of the bridge being

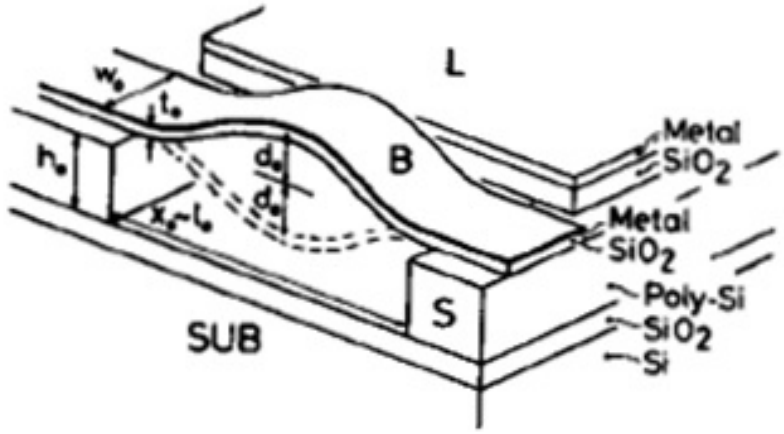

Figure 31. Nonvolatile memory cell utilizing a buckled beam. The two stable states, up or down, correspond to a digital one or zero. [62].

so small that its shock resistance is very high, makes this device absolutely nonvolatile. The bridge consists of a highly compressed film. In order to switch the bridge between its two states, electrostatic forces between the bridge and the substrate switch it into a down position and forces between the bridge and an adjacent electrode switch it into the up position. The memory state is read by measuring the capacitance of the bridge, since this will vary depending on its state, it provides a reliable, simple way to determine which of the two stable states the bridge is in.

Several other efforts have resulted in the design and fabrication of bistable, buckling beams [94, 95, 96, 97]. While these different efforts have differed in their design, fabrication method, and application, one common trait among them is that they are based on laterally actuated beams, parallel to the substrate they are fabricated upon. Qiu *et al.* [36] used the bistability of a laterally buckled beam to apply a constant force for a high current MEMS relay without the need for any external power. This beam was actuated back and forth by electrothermal actuators. Further analysis of these devices performed in [96] has shown similar findings described earlier in regards to the devices force vs. displacement curve.

Earlier research efforts have also looked into the behavior and application of bistable buckling membranes. Two major differences exist between the buckled beams previously discussed and these buckled membranes. First, and most obviously, they are membranes, meaning that they are clamped on all their sides instead of just at two points like the buckled beams. Secondly, they actuate perpendicular to the plane of the substrate. This means they are actuated vertically, rather than laterally.

Wagner *et al.* [70] investigated using two buckled Si/SiO_2 membranes to create a bistable microvalve with pneumatic coupling shown in Figure 32 These circular bistable membranes were actuated by applying a voltage differential between the membrane and a curved electrode underneath this membrane. The two membranes were sealed in with the chamber area above them pneumatically coupled. When one actuator is in the up position, the other is in the down position. By applying the voltage between the up membrane and its respective electrode, it is pulled downward. The pneumatic coupling between these two membranes causes the membrane that was in the down position to be pulled into its up stable state. This device was later implemented into a system for implantable drug delivery [98] This system used the alternating states of the bistable membranes as micro-valves that could be turned on or off depending on their rest state.

Arya *et al.* developed a thermally actuated bistable membrane [99] by applying a layer of aluminum to the silicon side of the membrane. Since the thermal expansion coefficient of Aluminum is ten times that of silicon, when heated, this aluminum layer will want to expand much more than the silicon layer it is deposited on. This will induce a compressive stress in the aluminum which counteracts the compressive stress in the oxide layer deposited on the other side of the silicon membrane. This will cause a deflection of the membrane in the direction of the aluminum, essentially, lessening

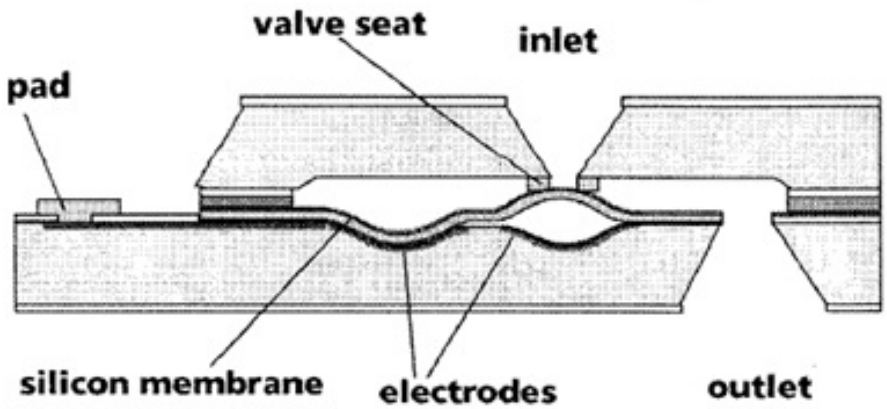

Figure 32. Pneumatically coupled microvalve created with two buckled Si/SiO_2 membranes.[62].

the initial deflection of the membrane caused by the CTE mismatch between the silicon and SiO_2 layer.

Negative stiffness elements also have a wide application in the area of vibration isolation mechanisms. Negative stiffness elements contribute to damping behavior because they tend to assist rather than resist deformation as a result of internally stored energy [100]. Minus K Technology developed a negative stiffness vibration isolation system which used the negative stiffness to effectively cancel out, or soften, the stiffness of a spring suspension. Reducing this stiffness magnifies the inherent damping of the system resulting in a compact, passive isolation system. This system was designed on the macroscale and is used to improve the isolation of air tables and other lab equipment [101]. Lee *et al.* used buckled plates to create a spring with negative stiffness to be implemented in a vehicle driver vibration isolation system [102]. Their design is applicable to a wide range of vehicle suspension applications, whether it be the vehicle suspension, seat suspension, cab mounting, or cargo container platform.

Negative stiffness can also be achieved by electrostatic means. With an increasing voltage differential, the force of electrostatic attraction between two objects increases, this force also increases as the distance between them narrows. In the case of a beam

or cantilever being actuated by electrostatic means, this electrostatic force will tend to counteract the mechanical restoring force of the beam or cantilever, effectively acting as a negative electrostatic stiffness on the member. This negative electrostatic stiffness has been implemented in the tuning of devices such as accelerometers and gyroscopes [103, 104, 105, 106]. The major drawback of this method is that the electrostatic tuning is an active method which requires the use of power.

2.5 Statistical Analysis Tools

Linear regression models are widely used in business, economics, engineering as well as the social, medical, and biological sciences. Successful applications of these models requires a sound understanding of the theory and practical problems that are encountered when employing these methods in real life. [107]. Linear regression is an approach for modeling a relationship between a dependent variable, typically denoted as Y, and a independent variable typically denoted as X.

This method will result in a linear statistical model which may be used for predicting the results of additional trials. Several software tools such as SAS (Statistical Analysis System), SPSS (Statistical Package for the Social Sciences), JMP and even Microsoft Excel are capable of generating a linear statistical model based on data provided.

However, detailed statistical analysis requires more than just the generation of a trendline. The linear regression model is based on certain assumptions about the data, that if are not correct, invalidate the generated model. Tests of these assumptions must be run in order to have any degree of confidence in the validity of the model [107]. The assumptions made are that there is a constant variance in the error of the model. Non constant error variance may indicate that may indicate additional weighting of the data towards one particular end of the range of independent variables.

[107]. Once identified, remedial measures such as a transformation of the data may be taken which will validate the assumptions made.

Once a valid model is made and all assumptions are met, inferences can be made about the data. One of the most important tests that can be run is to determine whether or not the slope of the model is non-zero. In some instances, the slope of a model may be very small, implying that there is no statistical relationship between the dependent and independent variables. The two-sided t-test can determine with a certain degree of confidence chosen by the analyst (typically 95%) whether or not that slope of the model is statistically different from zero or not. In other words for example, it can be determined with 95% confidence that there is a statistical relationship between the dependent and independent variable. This analysis also can be used to identify and remove statistical outliers which may skew the data and lead to a less accurate model.

This method of statistical analysis is a powerful and useful tool. When properly used it will result in an accurate model to use for predicting the results of future testing as well as determining whether or not statistical relationships between two variables exist or not. Higher complexity models can also be generated to examine the effects of multiple independent variables on one dependent variable.

2.6 Summary

This chapter presented the necessary concepts relating to the devices presented in this research. A discussion on the basic fabrication methods of MEMS devices was provided. Both of the main methods discussed, surface and bulk micromachining, are integral to the fabrication of the membranes used in this effort as well as photolithography and deep reactive ion etching. Secondly, a discussion on the important theoretical concepts that dictate how these membranes behave was presented to in-

clude why they buckle, and how they behave once they are in a buckled state. Finally, an overview of some different applications of similar designs have been implemented in previous research was provided.

The following chapter will describe the methodology of this research. This will include a description of the fabrication steps of the membranes and heaters, as well as bonding and integrating these membranes into larger devices. Descriptions of the test equipment is provided as well as a discussion on the simulation of the membranes.

III. Methodology

The previous chapter outlined the basic theory behind the behavior of the buckled membranes studied in this research. This chapter will discuss the methodology of the research performed for this effort. First, details on the fabrication of the membrane and the electrothermal heaters are provided. Next, details are provided on the steps to bond additional devices. Details of finite element method modeling of the membranes are provided next. Finally, a description of the test equipment and setup used for the measurement and analysis of these devices is provided.

3.1 Membrane Fabrication

The buckled membrane structures are fabricated on a silicon-on-insulator (SOI) wafer. The wafers consist of a 500μm thick Si handle with a 2μm thick buried oxide layer of SiO_2 grown on top of the handle layer. A 5μm thick device layer of Si is bonded on top of the buried oxide layer. The membranes are released by way of a backside etch through the entire depth of the handle wafer, stopping at the buried SiO_2.

The SOI wafers were first diced into 1 inch by 1 inch square samples for easier processing. Prior to the dicing, a protective layer of S1818 photoresist was applied to the wafer. This layer serves to protect the wafer from any debris resulting from the dicing process. After dicing, the samples were cleaned with a 30 second acetone rinse, 30 second methanol rinse, and a 30 second deionized water (DIW) rinse and dried with pressurized nitrogen.

Following the step, the samples were submerged in a buffered oxide etch buffered oxide etch (BOE) for 1 minute to remove any native oxide and maximize SU-8 adhesion to the sample. The samples were then rinsed in DIW for 30 seconds and

dried with pressured N_2. Finally, the samples were placed on a hotplate at 110°C to evaporate any remaining moisture and then allowed to cool.

After the samples had cooled, a layer of SU-8 was spin coated at 3000 RPM for 30 seconds on the handle side of the sample to obtain a 25μm thick coating of SU-8. Following the sping coating, the sample was soft baked on a 65°C hotplate for 2 minutes then placed on a 95°C hotplate for 5 minute. The samples were then allowed to cool before they were exposed.

The samples were aligned using the Karl Suss MJB-3 mask aligner and exposed. The UV power of this tool is set to 11mW/cm^2. The exposure time was set to 15 seconds to provide an exposure energy of 165mJ/cm^2 as prescribed by the SU-8 data sheet [7]. Following the exposure, the samples were placed on a 65°C hotplate for 1 minutes then placed on a 95°C hotplate for 5 minute for the post exposure bake (PEB). The samples were then developed for 1 minute using Microchems SU-8 developer and then rinsed in DIW. The development opens up the windows in the SU-8 mask layer that will allow the cavity in the handle to be etched with DRIE.

The samples were etched using the University of Michigan's STS Pegasus DRIE. Because this tool can only accept 4 inch diameter wafers, the 1 inch by 1 inch samples had to be mounted to a 4 inch carrier wafer. Santovac pump oil is used as an adhesive between the carrier wafer and the sample. The santovac is used because it provides good thermal conduction between the carrier wafer and the sample. Also, because it is designed for use in high vacuum systems, it will not produce any byproducts while in the DRIE process chamber [108].

The etch rate of the STS pegasus 4 has been characterized at 15μm/minute for features larger than 100μm so an etch time of 34 minutes was chosen to etch completely through the 500μm thick handle. After the etch was complete the samples

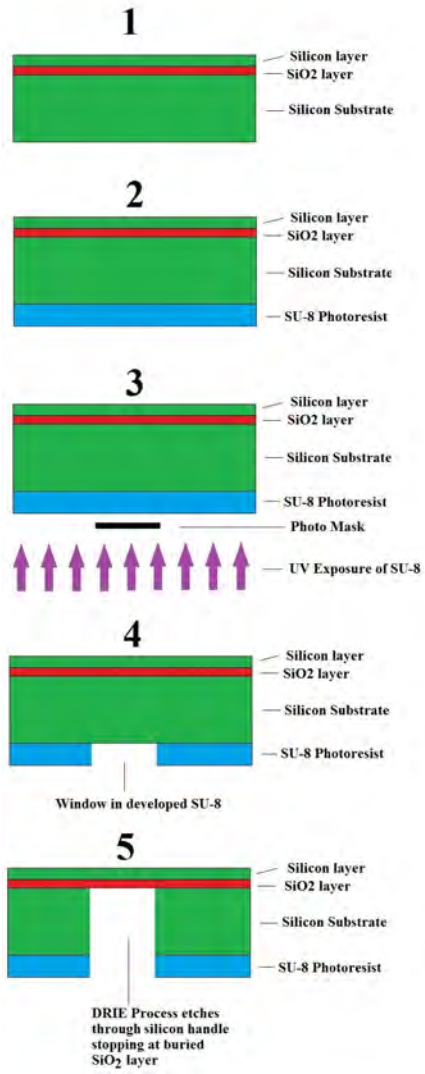

Figure 33. Illustration showing the fabrication process for the buckled membrane.

were removed from the carrier wafer by soaking them in acetone for a 24 hour period to dissolve the santovac.

3.2 Heater Fabrication

The membrane is heated by a meandering resistive heating element fabricated directly on top of the membrane. As current flows through this heater it experiences Joule heating and heat is transferred by conduction to the membrane, thereby

increasing the thermal strain which causes an increase in deflection. The resistive heating element shown in Figure 34 consists of a 3000$\AA$ layer of gold on top of a 500$\AA$ layer of titanium which serves as an adhesion layer. This was pattered using the liftoff method.

The sample is first cleaned with a 30 second acetone rinse, a 30 second methanol rinse, and a 30 second DI water rinse and dried with pressurized N_2. A layer of S1818 photoresist was spin coated on to the device layer side of the sample and spun for 30 seconds at 4000 RPM resulting in a 1.8μm thick coating of photoresist. This was then baked at 110°C hotplate for 75 seconds and then allowed to cool.

The photoresist is then exposed to UV light using the MJB-3 mask aligner for 7 seconds to provide an exposure dose of 77mJ/cm^2. Following the exposure, the photoresist was developed in a developer solution of 5:1 DI water to 351 developer for 30 seconds. Following the development, the sample was rinsed in DI water for 30 seconds and dried with pressurized N_2.

With the heater now patterned in the photoresist, the samples were placed in the Torr International electron beam evaporation tool. This tool uses a focused beam of electrons to evaporate metals which then deposit on the samples. The first layer deposited was a 500$\AA$ layer of titanium to serve as an adhesion layer between the silicon and the 3000$\AA$ gold layer which was subsequently deposited.

After the the metal deposition, unwanted metal was removed by a liftoff process. The samples were placed in a container of acetone which was then placed into an ultrasonic bath. This acetone dissolved the remaining photoresist which removed the metal deposited on top of it, leaving only the resistive heater on the sample.

Two different heater designs were used. The tunable pressure sensor uses a single heater which covers the the entire area of the membrane (Figure 34 left.) The multidirectional thermal actuator requires four smaller heaters which each cover a single

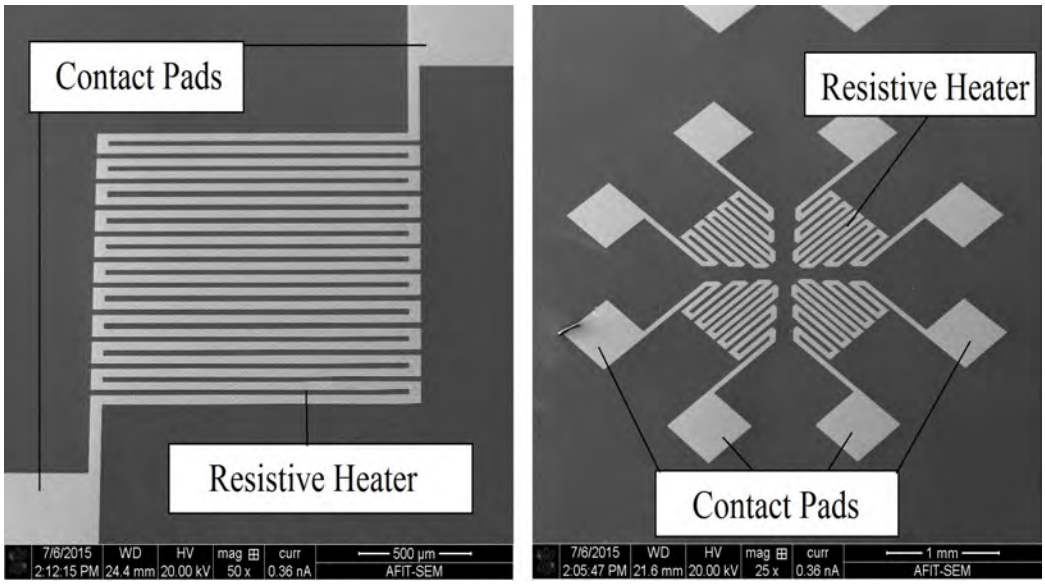

Figure 34. Scanning electron microscope images of the two heater designs used. The single heater design (left) is used for the tunable pressure sensor design and the multiple heater design (right) is used for the multi-directional electrothermal actuator.

quadrant of the membrane in order to provide localized heating of the membrane (Figure 34 right.)

3.3 Bonding and Integration

In order for the buckled membranes to be integrated into larger, more complex systems a method of bonding them to other devices is needed. Two methods of bonding were investigated. The first attempt at bonding a structure to the membrane involved the use of SU-8 photresist as an adhesion material.

In this study, SU-8 bake times and temperatures were kept constant throughout fabrication while UV energy exposure was varied. Once the test structures were fabricated and flip-bonded together, the SU-8 bonded structures were then systematically tested under tensile loads to determine the separation force needed to break the SU-8 bonds. The resulting data was analyzed and the statistical significance of the UV exposure parameter was examined.

3.3.1 Test Structure Fabrication.

Fabrication of the SU-8 test structures followed the prescribed process flow given by Microchem in their SU-8 (2000) processing guidelines shown in Figure 35. All of the processing took place in a class 1000 cleanroom with the temperature and humidity maintained at 68°C and 35%, respectively. During the substrate pretreat processing step, organic contaminants were removed from three inch, n-type (100) silicon (Si) wafers with acetone, methanol, and DIW sprays for 30 seconds each followed by a clean, dry N_2 spray. The wafers were then dipped in a 7:1 buffered oxide etch (BOE) for 1 minute to remove the native oxide layer and maximize SU-8 adhesion to the Si wafer. This ensured that SU-8 adhesion to the silicon wafer was greater than the bond strength between the SU-8 test structures and isolated the bond strength of interest in this research. The wafers were then rinsed with DIW for 30 seconds, dried with N_2, and then heated on a hotplate for 2 minutes at 110C to evaporate off any

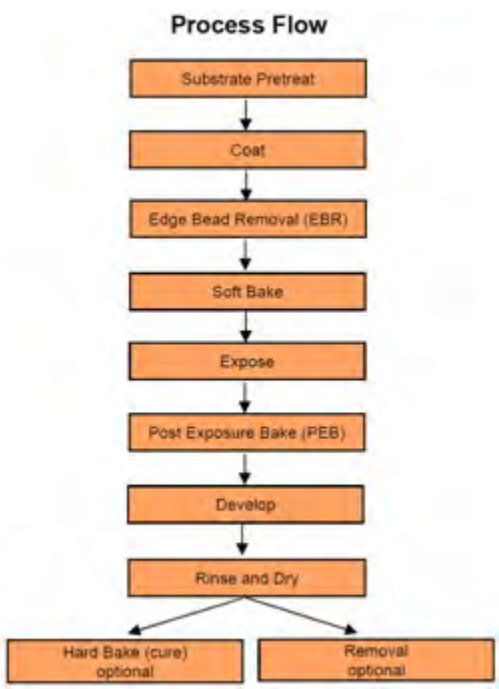

Figure 35. Process Flow for SU-8 fabrication as outlined by Microchem SU-8 datasheet.[7]

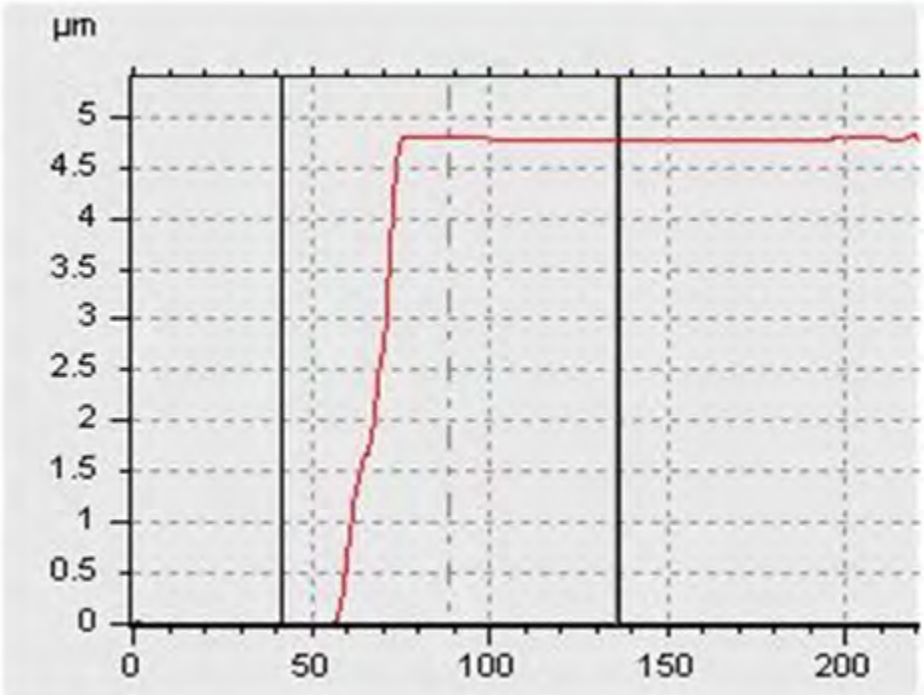

Figure 36. A representative step height measurement, using a KLA Tencor Alpha IQ Step profilometer, of an SU-8 test ring with a step height of 4.7μm.

remaining moisture. After cooling for approximately 15 minutes, the wafers were then spin-coated with SU-8 at 500 rpm for 5 seconds and then 3000 rpm for 30 seconds resulting in a uniform layer of SU-8 approximately 5μm thick (as shown in Figure 36). Immediately after spin-coating, the wafers were soft baked for 2 minutes at 95C.

Following soft bake, the wafers were exposed using a Karl Suss MJB3 mask aligner with the UV power set to 11mW/cm^2. Exposure times were varied from 5 seconds to 15 seconds resulting in total UV energy doses ranging from 55mJ/cm^2 to 165mJ/cm^2 to provide different degrees of cross-linking in the SU-8. Based on the 5μm thickness of the SU-8 bond structures, exposure energy of 93.5mJ/cm^2 was the manufacturer recommended energy dose according to the SU-8 application guide [1]. This dose was taken to be 100% level and all other doses were determined from this baseline value, resulting in exposure doses ranging from 58% to 176% of the recommended energy

dose. The bonded test structures, shown in Figure 37, were square rings 200μm wide and 2mm in length, with a total bondable area of 1.44mm^2.

Immediately after UV exposure, the wafers were transferred to a hotplate for the Microchem recommended PEB of 95°C for 5 minutes. The samples were then developed for 1 minute using Microchems SU-8 developer and then rinsed in DIW and isopropyl alcohol (IPA) for 30 seconds and 10 seconds, respectively. Next, the test structures were dried thoroughly using clean, dry compressed N_2 gas. The wafers were then diced into squares approximately 6.35mm inch by 6.35mm with each sample containing one complete bond pad. Following dicing, the samples were again rinsed with IPA and dried with N_2 to remove debris from the dicing process.

3.3.2 Flip Bonding and Test Structure.

Next, the samples were bonded together using a Semiconductor Equipment Corporation, Eagle 860 flip-chip bonder. The bonding process for all of the samples was kept constant to ensure that UV exposure was the only variable in the fabrication

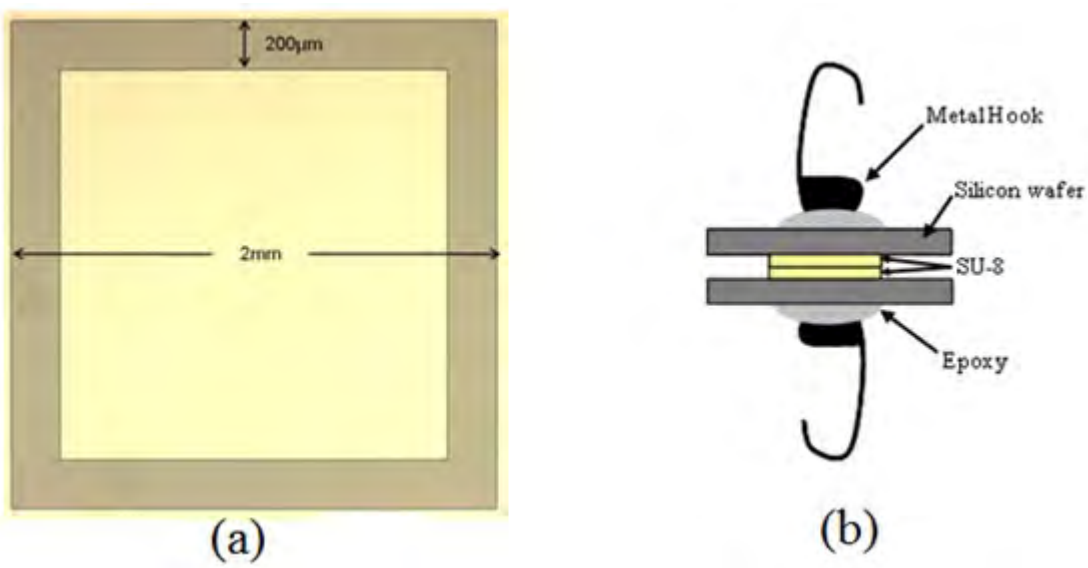

Figure 37. (a)Optical image of fabricated bond pad consisting of a square ring measuring 2mm by 2mm with a width of 200μm. (b) Cross-sectional diagram of the fully assembled structure ready for tensile load testing.

process. The pre-programmed bonding sequence had both the tip and stage temperature set at 125°C. During the bonding sequence, they were both rapidly heated to 150°C while a load of 1-kg was applied for 10 seconds. With flip-bond pressure removed, the stage was rapidly cooled back to 125°C with flowing N_2. This controlled timing minimized any residual temperature effects and inadvertent SU-8 cross-linking to ensure the only variable in the experiment was the level of cross-linking due to the varying UV exposure.

After the SU-8 square rings were flip-chip bonded together, small metal hooks were fixed to outside Si surfaces, as shown in 37, using a two-part epoxy. The hooks were dipped in the epoxy and then placed in the center of the bonded samples, taking care to align the hooks directly over each other (also shown in Figure 37). This ensured that the tensile load forces, applied during the separation test sequence, were normal to the bonded structures and that shear loads were minimized. The material used to make the metal hooks was extremely rigid and chosen to minimize flex or stiffness variations during tensile load testing resulting in highly consistent force measurements.

3.3.3 Seperation Force Testing.

A Microforce Testing System (MTS) Tytron 250, shown in Figure 38, was used to apply the tensile loads and pull the bonded SU-8 test samples apart. The MTS Tytron 250 system was configured to perform automated load testing ranging from 0.001N to 44.5N while recording necessary data. The test samples were mounted horizontally in the MTS unit between two clamps using a one inch loop of ultra low stretch braided line to minimize the effects of stiffness variations during testing. The sequence for mounting a sample in the system follows: 1) the right, movable clamp was commanded to the home position, 2) braided line loops were then placed onto

the sample hooks, and 3) the right, movable clamp was positioned, away from home, so that the sample sagged slightly with no measurable axial force. With the force test ready to begin; the software was configured to pull at a constant rate (1mm/minute) with the force and clamp displacement being measured every 9.77ms. Figure 39 shows an example of a test run where an applied tensile load of approximately 1.13 N was required to separate the test sample and break the SU-8 bonds.

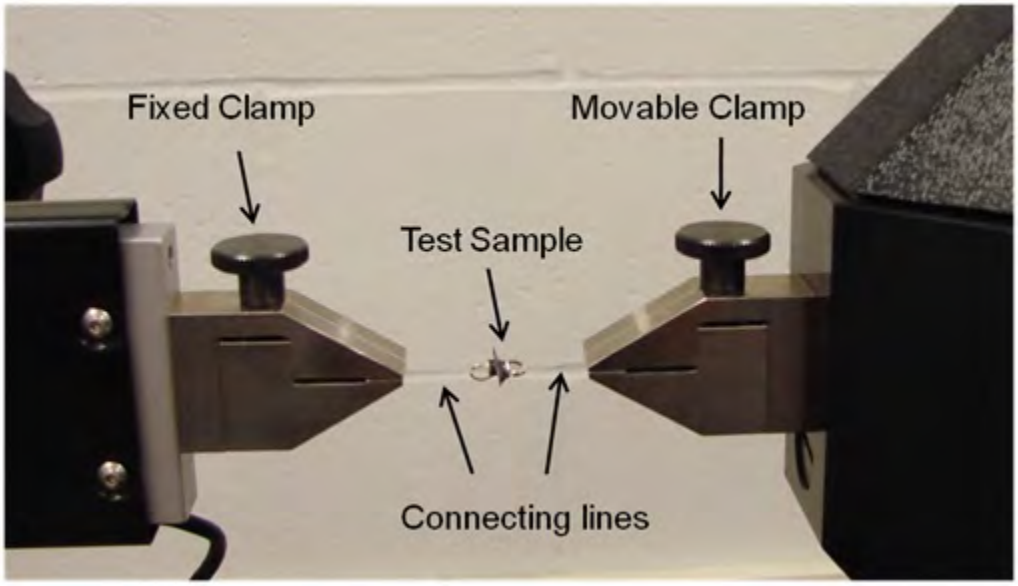

Figure 38. Fully assembled mechanism for testing the seperation force of the bonded sample.

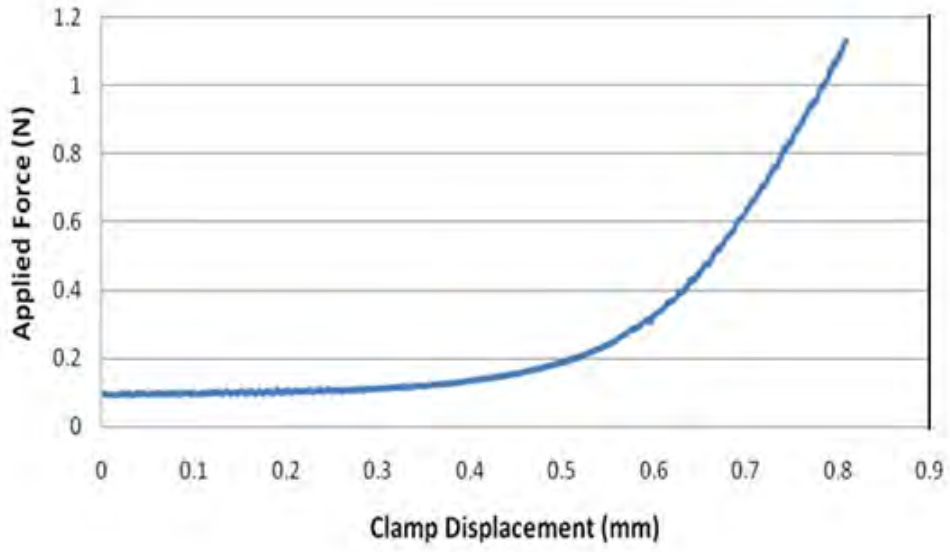

Figure 39. Graph of the applied force versus clamp displacement showing an SU-8 bonded structure that separated with approximately 1.13N of applied force.

A second method for bonding with SU-8 was attempted in which the flip-chip bonding took place prior to the DRIE process to eliminate the possibility of destroying the membrane with the large bonding forces required to bond SU-8. In order to perform the DRIE on the back side of the SOI sample, the bonded device was placed into a cavity that was DRIE etched into a 1" x 1" sample of silicon. This cavity provides the necessary heat transfer between the DRIE platen and the sample in order to keep etch rates constant and protect the bonded sample from the DRIE process.

During the processing, the sample became unseated from the spacer as a result of the pressure difference between processing chamber and the cavity. As a result, the samples were destroyed during the processing.

3.3.4 Epoxy Bonding.

Because of the fragile nature of the membranes, an additional method to bond structures was devised that requires no applied pressure for bonding and therefore

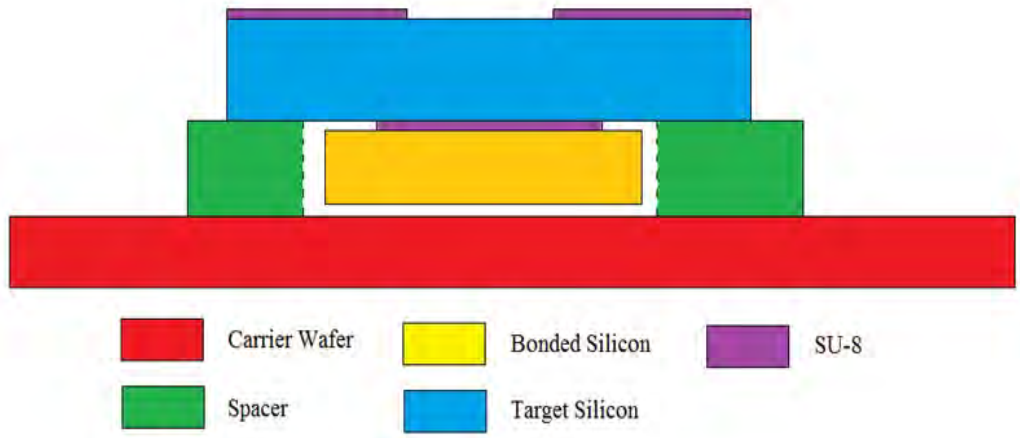

Figure 40. Cross sectional diagram of assembly used for DRIE processing after bonding.

minimizes the risk of damaging or destroying the membrane. This method uses Dymax EMAX 403, optically clear structural adhesive to adhere the devices to the membrane. This epoxy is designed for rapid bonding of glass and metals. It contains no reactive solvents and cures upon exposure to ultraviolet light. The structure to be bonded to the membrane shown in Figure 42 was fabricated using a DRIE process in order to create 300μm x 300μm pillars that were 200μm tall. Once this etching was complete, the samples were diced into 1mm x 1mm squares.

First, the epoxy is applied with a pneumatically activated syringe to the center of the membrane as shown in Figure 41. Prior to the application of the epoxy, the membrane is set in its buckled down position for two reasons. First, this will ensure that the epoxy will not flow away from the center of the membrane since it is already at its lowest point. Second, being in the buckled down state guarantees that the membrane will not snap through once the sample is brought into contact with it. If this were to happen, the tool may feel the response force, and disengage before the sample has been properly seated in the center of the membrane.

After application of the epoxy on to the membrane, it is placed on a Fine Tech Femto Flip-Chip bonder. Once the pillar is aligned with the epoxy dot on the mem-

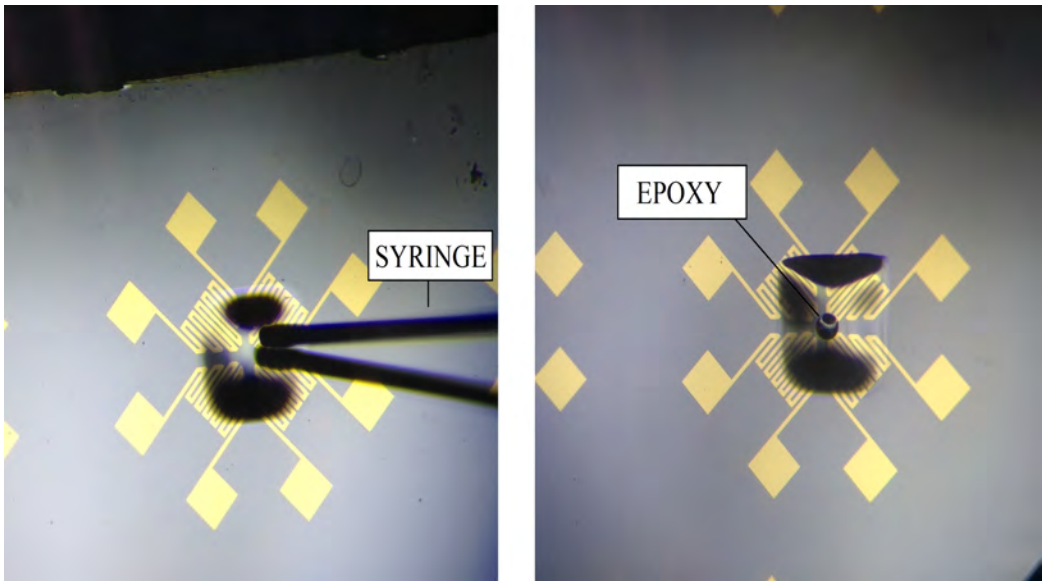

Figure 41. Optical microscope image of the application of epoxy to the membrane. The epoxy is applied by using a pneumatically driven syringe (left) leaving a controlled amount of epoxy in the center of the membrane (right)

brane, the sample is slowly brought down to the membrane and released while exerting a minimum amount of pressure on the membrane. Once released, the epoxy is cured with UV light and the process is complete. Once the epoxy has been cured, the membrane can then be placed in its buckled up position for testing and analysis.

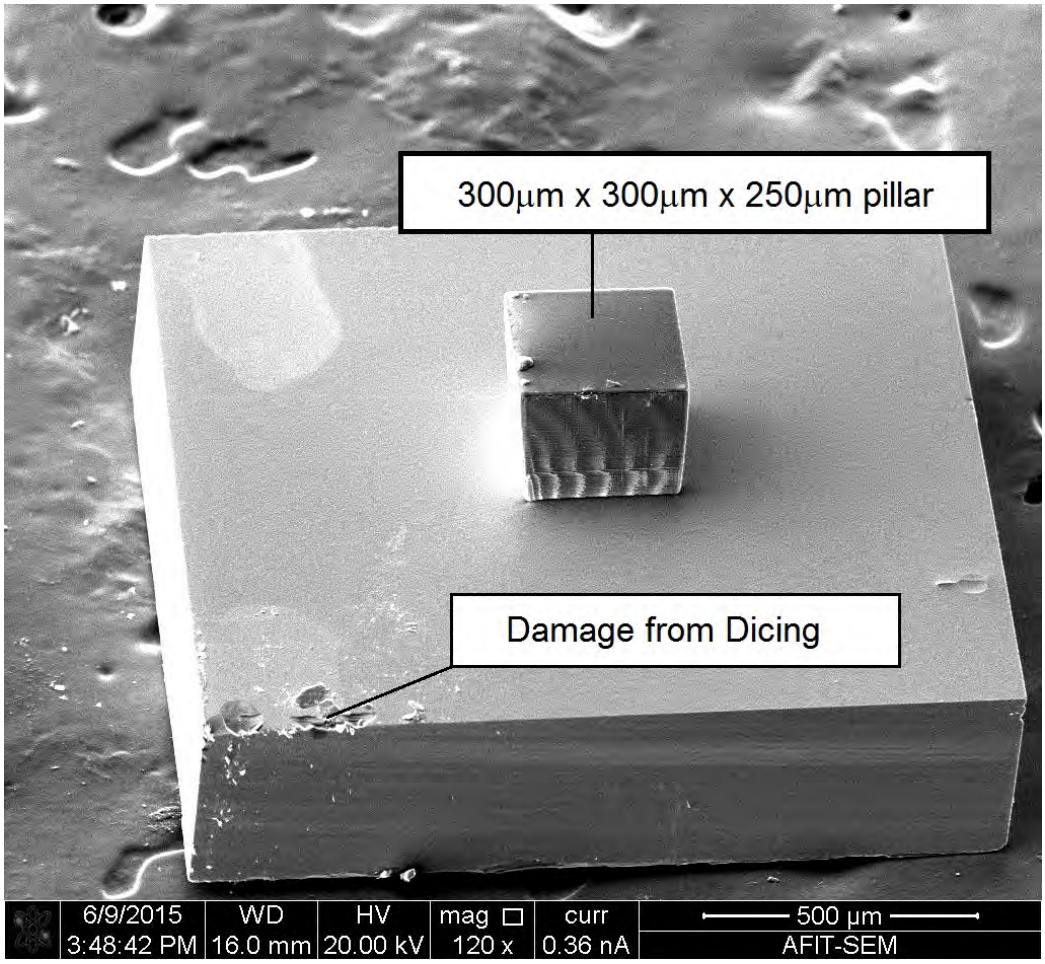

Figure 42. SEM image of the the samples fabricated for epoxy bonding to the buckled membrane. The 300μm x 300μm x 200μm pillars are centered on a 1mm x 1mm square silicon.

3.4 Membrane Testing Equipment

A white light optical interferometer by Zygo New View 7300 was used to measure membrane deflection once it was released into its post-buckled state. This tool reflects light from the surface of the sample in order to quantify step heights, surface roughness, and other topographical features. Three dimensional models of the surface features are generated by the tools software which allow the measurements to be made as shown in Figure 43.

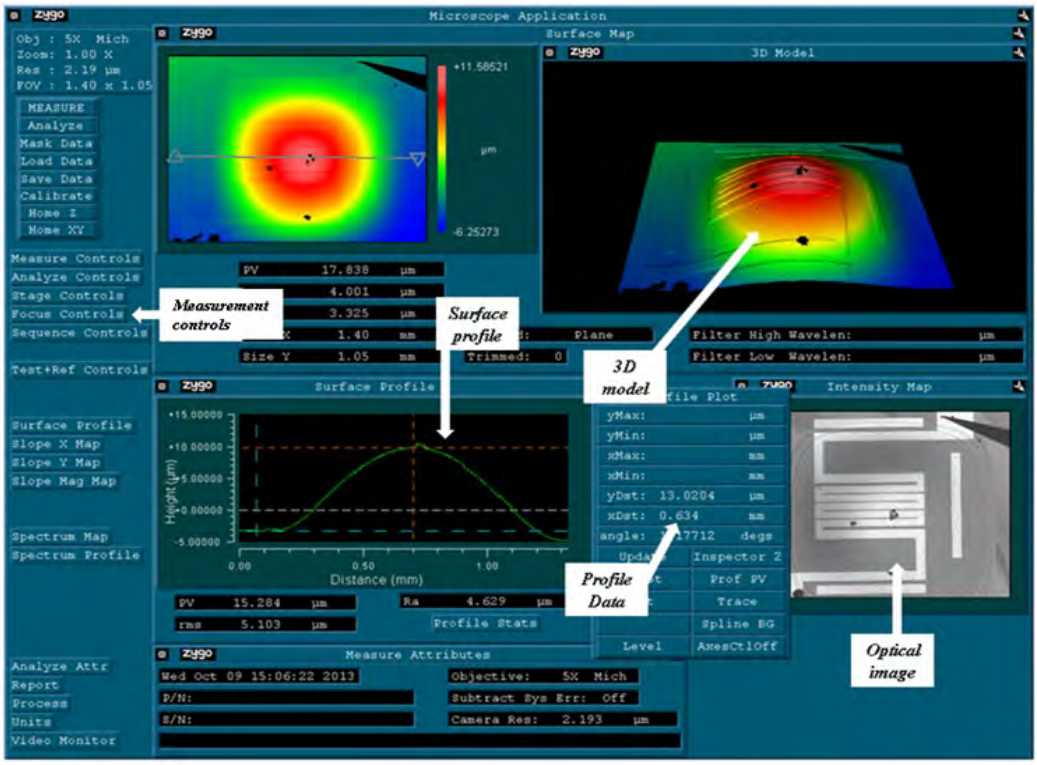

Figure 43. Zygo interface screen showing the measurement controls, surface profile, 3D model, profile data, and optical image.

To test these tunable pressure sensors on the Zygo, a specialized platform was fabricated shown in Figure 44. This platform is a solid square slab of aluminum with a 2mm hole drilled in the center of the horizontal surface. A second hole is drilled in to the side of the platform which intersects the hole from the horizontal surface. A threaded adapter which accepts a 1/4 inch pressurized N_2 line is threaded into the the second hole. This set up directs the pressurized N_2 to the back of the pressure sensor.

On the horizontal surface of the platform are two nylon clamps that are held in place by screws. These clamps keep the pressure sensor from drifting around due to the pressure on their under side as well as ensure a tight fit between the pressure sensor cavity and the 2mm hole. An adjustable pressure regulator between the N_2 source and the platform is used to control the pressure applied to the tunable pressure

sensor. The complete setup of the test station, shown in Figure 45 makes it possible to measure the deflection of the tunable pressure sensor while adjusting both the temperature of the resistive heater and the applied pressure simultaneously.

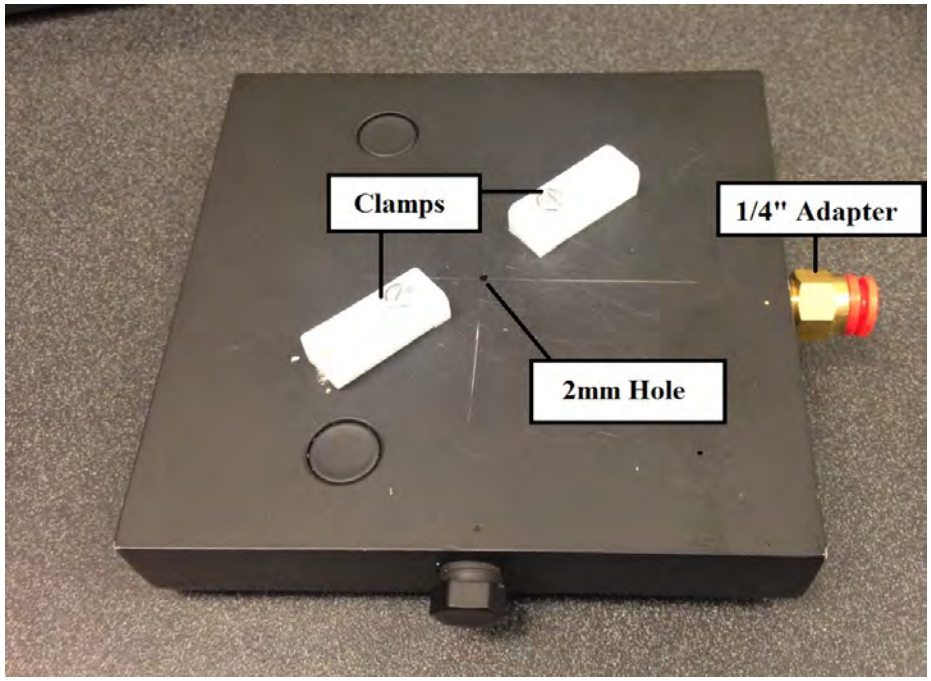

Figure 44. Platform for holding samples in place while applying pressurized N_2 to the back of the pressure sensor during deflection measurement with the Zygo.

After sample is aligned properly over the 2mm hole and securly clamped down the tunable pressure sensor is positioned under the lens of the Zygo so that the membrane and contacts are visible. Once in position, voltage probe tips are put into contact with the contact pads. These probe tips are connected to an adjustable DC power supply. Proper contact is verified by setting the DC power supply output to one volt. The probe tips are adjusted until a non-zero current is read on the power supply display. This current flow signals that the probe tips are properly positioned on the contact pads. With the tunable pressure sensor securely in place under the Zygo lens and the voltage probe tips in contact with the contact pads of the electrothermal heater, deflection measurements of the pressure sensor can now be made for each combination of applied pressure and temperature on the tunable pressure sensor.

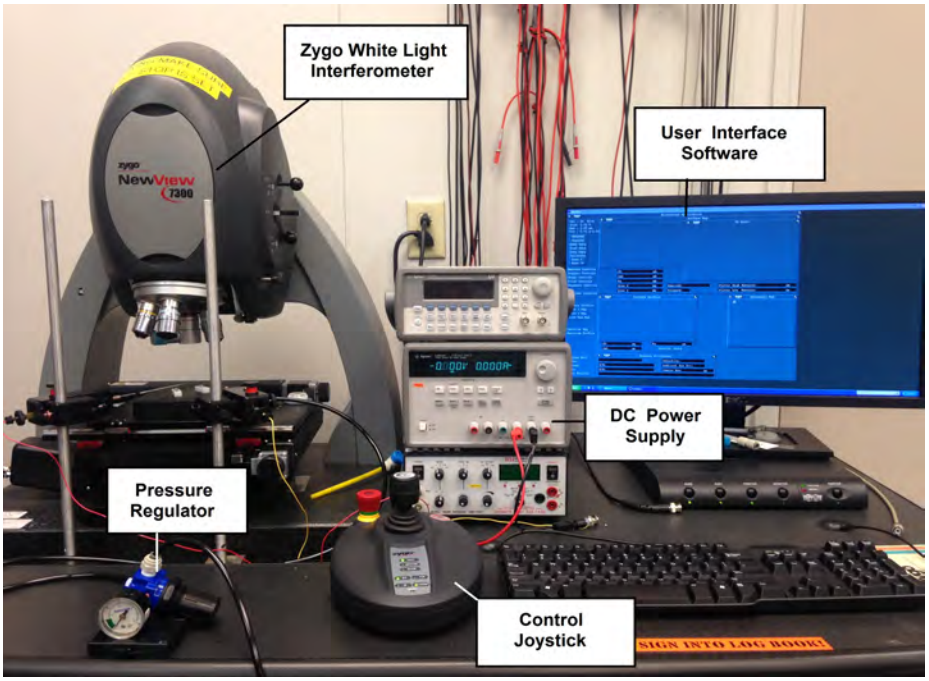

Figure 45. Testing bench with the Zygo white light interferometer, dc power supply, and pressure regulator.

3.5 Finite Element Modeling of Buckled Membrane

Finite element method (FEM) partitions a structure into simply shaped portions called finite elements. It then generates an approximate solution for the variable of interest within each element, then combines the approximate solutions [109].

FEM is similar in concept to the Reimann sums method for integration. This method divides the area under a curve into several rectangular sections. The area of each of the individual "finite elements" is calculated, and the sum total of all the areas represents the area under the curve [110]. The accuracy of the approximations for both the Reimann sum method and FEM are both a function of the size of the individual elements in relation to the overall device size and shape.

Finite element modeling of these buckled membranes was performed using CoventorWare™. This software suite allows the user to create a model of the device to be tested including material properties. After the creation of the solid model, the user chooses the

size and style of the finite elements, known as a mesh. After generating the mesh the user can select from a comprehensive suite of solvers such as mechanical, electrical, thermal, etc. Finally, after the calculation is complete, the user is presented with a 3D rendering of the device which can display the desired behavior of the device [111].

The models consisted of two stacked square plates of the same area and different thicknesses to correspond to the thickness of the SiO_2 layer and the Si layer. To simulate the compressive stress induced in the SiO_2 layer, a stress of -240 MPa was selected in the material properties of the oxide.

3.5.1 Mesh Convergence.

Recall that like the Reimann sum method for finding the area under a curve, the accuracy of FEM analysis is dependent upon the size and shape of the mesh elements used. If the dimensions are too large, the result will be inaccurate results. Conversely, if the elements are too small, then computation time will be unnecessarily long. A mesh convergence study was performed in order to determine the best mesh size which provides accurate results, while minimizing computing time. This study uses the harmonic analysis feature of CoventorWare^{TM} to calculate the modal frequency of the membrane. The natural log of the modal frequencies were plotted with respect to the inverse number of elements (Figure 46).

The results of this method, known as the Richardson extrapolation method, were curve fit, and the y-intercept was taken as the location of infinite mesh refinement. This value was interpreted to be the actual modal freqency of 80500.76 Hz [111, 112]. The results of the study and their corresponding error are summarized in table 1. A mesh size of 1μm by 1μm by 1μm was found to have less than 0.1% error with a run time of of 9 minuts, 58 seconds.

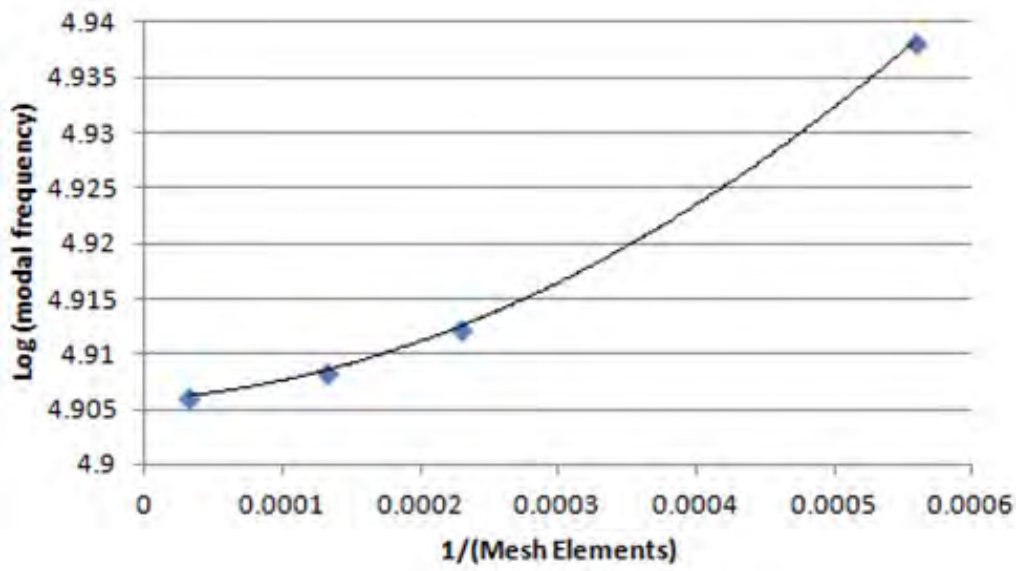

Figure 46. Plot of four models of different mesh size and their respective modal frequency. As the mesh size decreases, the modal frequency begins to converge on the point of infinite mesh [112].

Table 1. Mesh element size with corresponding modal frequency and error measurement.

Mesh Element Size	1st Modal Frequency (Hz)	Corresponding Error (%)
Infinite	80500.76	0
100μm	113502	40.995
60μm	86738.38	7.749
40μm	81743.05	1.543
30μm	81011.84	0.634
15μm	80572.59	0.089

3.5.2 Buckling Simulation.

Simulating the steady state buckling of the membrane is a two part process. Since CoventorWare^{TM} simulates the membrane as completely defect free, if left undisturbed, the membrane will remain in the unstable equilibrium point, illustrated by point B in Figure 24. The results of this are shown in Figure 47.

To remedy this, an initial simulation must be performed with an external load applied to the bottom of the membrane in order to give it the "nudge" it needs to snap into its stable equilibrium point. Once the simulation is complete, it can be

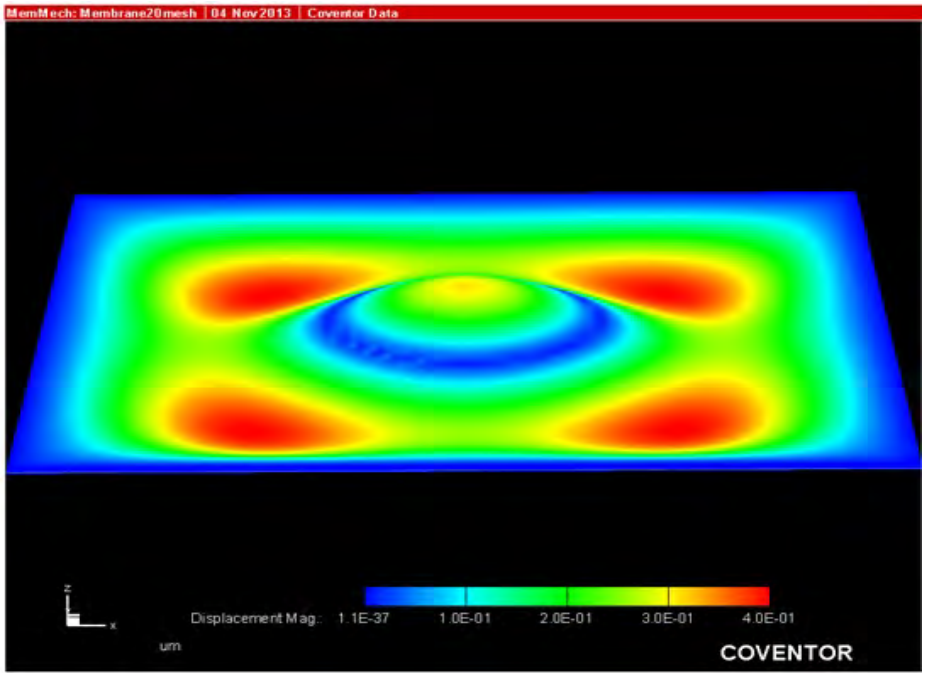

Figure 47. Example of a simulated undisturbed membrane under compressive stress resting in its unstable equilibrium point.

re-ran using the previous results. However, this time the external load is removed which causes the membrane to settle at its stable equilibrium point. With the membrane now in it's stable equilibrium state shown in Figure 48, further analysis can be performed.

3.6 Summary

This chapter provided the details of how the devices used in this research were fabricated. Detailed descriptions of how MEMS fabrication techniques were used to create the buckled membranes and the electrothermal heaters. Following this, the method for bonding and integration was detailed including a description of a study on the application of SU-8 photoresist as a bonding material. A description of the testing equipment used to measure the membrane deflection of the membranes as a function of applied pressure and temperature was provided. Finally, a description

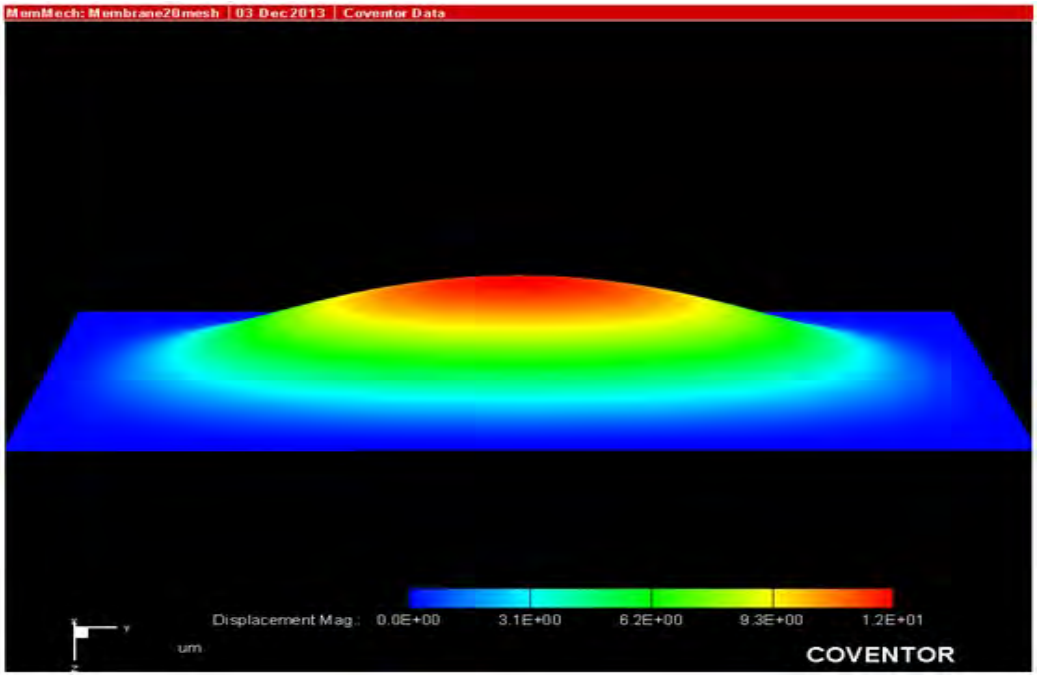

Figure 48. Example of a simulated post-buckled membrane in its stable equilibrium position.

of finite element method techniques that were used to model the behavior of the membranes was provided. The next chapter will present the results of the testing performed on these devices.

IV. Results

This chapter provides the results of testing the buckled membrane devices. The primary measurement of these devices was the deflection as it related to increasing temperature and pressure applied to the back of the membrane. The main interest is to understand how the sensitivity of these membranes changes as thermal stress is increased. Additionally, test results of the multidirectional thermal actuator are presented illustrating it's range of motion in its four different axes. Chapter V will include a detailed analysis of the results presented here.

4.1 Analytic Results

A brief discussion on membrane theory and buckling was provided in Chapter II. From this theory and the equations provided, we can obtain an estimation of the membranes behavior when buckled. Figure 49 shows the strain energy curve for a 1.5mm x 1.5mm membrane with a 5μm thick silicon mechanical layer and a 2μm thick buried oxide layer. Again, the two local energy minima positions correspond to the two stable equilibrium points representing the buckled up, or buckled down position. The x-axis of this plot represents the deflection of the membrane as a ratio of the total thickness of the membrane, 7μm. Each stable equilibrium point in this curve corresponds to a deflection of approximately 18μm.

Recall from Figure 20 that increasing the stress in the membrane, in this case by introducing additional thermal stress, increases it's deflection. By combining the equation for the thermal stress and the equation for the total internal strain energy, the total deflection of the membrane as temperature increases can be analytically determined. This is plotted in Figure 50 for increasing 100K temperature increments from room temperature to 1000K.

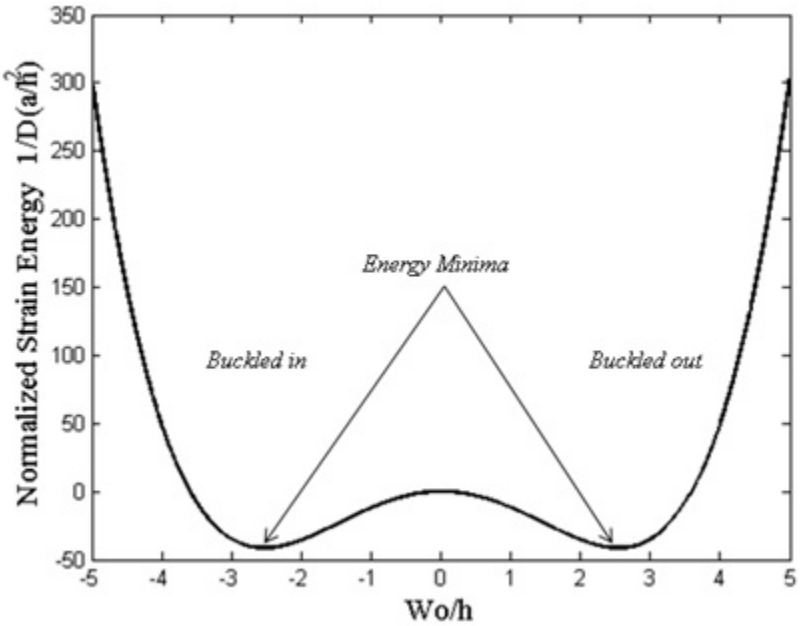

Figure 49. Plot of the internal strain energy of a 1.5mm by 1.5mm membrane. The two local energy minimas shown represent a total buckled deflection of approximately 18μm.

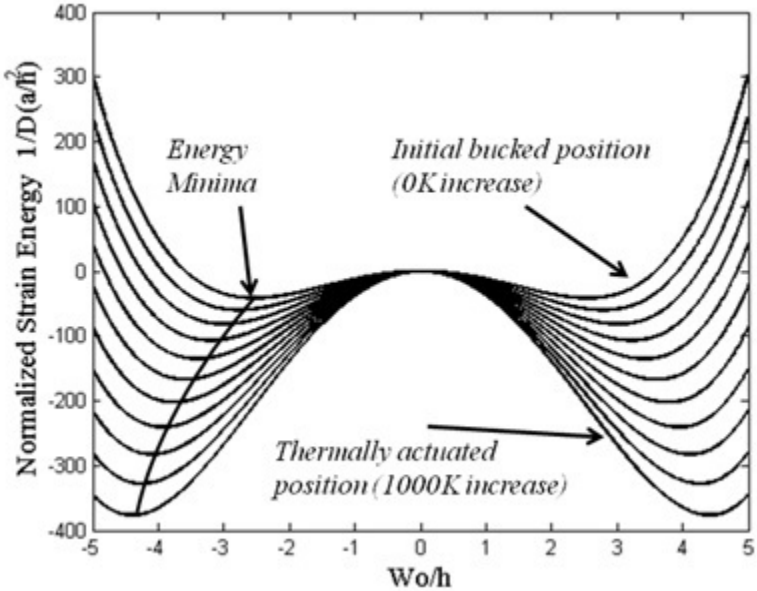

Figure 50. Plot of total internal strain energy of a 1.5mm x 1.5mm membrane for increasing temperature from 300K to 1000K.

Taking the energy minimums of this plot for each temperature, we can determine the total membrane deflection versus the applied temperature. This data, illustrated

by Figure 51, shows that a 1.5mm x 1.5mm membrane will have an initial deflection of approximately 18μm at room temperature and deflect to approximately 31μm at 1000 K.

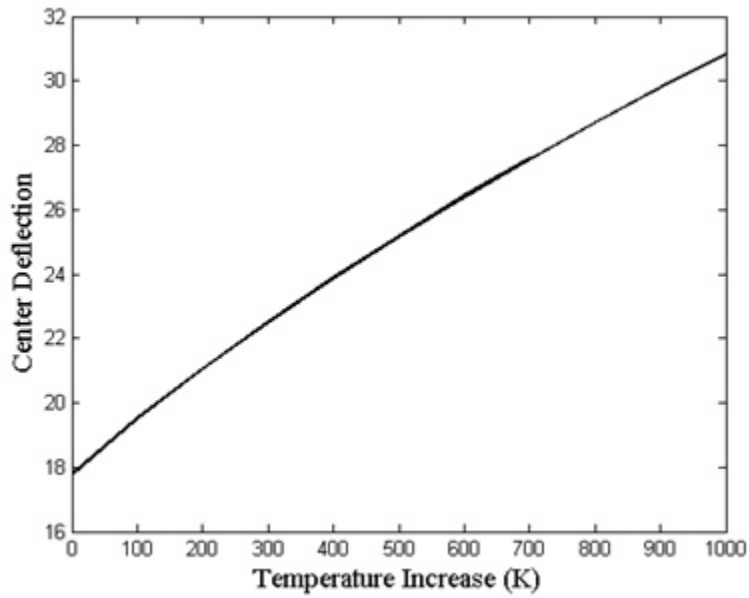

Figure 51. Plot showing the membrane deflection vs. applied temperature. A 1.5mm x 1.5mm membrane will have an initial deflection of approximately 18/mum at room temperature and increase to approximately 31μm at 1000 K.

Further analysis was performed to model the deflection of the membrane versus its size. Three different square membranes were analyzed, 1.0mm by 1.0mm, 1.5mm by 1.5mm, and 2.0mm by 2.0mm. Furthermore, two different thicknesses of the silicon mechanical layer were used to analyze how the thickness affects the rigidity of the membrane. The results illustrated in Figure 52 below indicate that the deflection increases as its size increases. Additionally, the thicker mechanical layer has the effect of increasing the flexural rigidity of the membrane causing a smaller deflection than the same size membrane with a thinner mechanical layer.

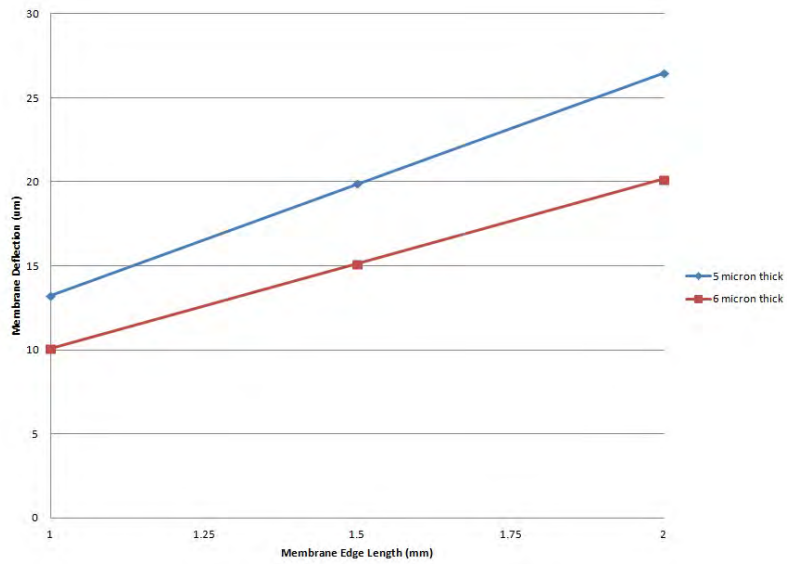

Figure 52. Plot showing the relation between membrane edge length and deflection for 1.0mm, 1.5mm, and 2.0mm membranes. A thinner, 5μm thick membrane will deflect more than a thicker 6μm thick membrane of the same size due to the thicker membranes increased flexural rigidity.

4.2 FEA Results

Finite element method analysis was performed to simulate the behavior of the buckled membranes. With appropriate mesh size determined earlier, the membrane models were built in the software model editor. Membranes with a 5μm thick Si layer on top of a 2μm thick SiO_2 layer were created of varying sizes. The appropriate material properties were verified in the software's material property database. Simulations were preformed to analyze the membranes initial deflection with respect to its dimensions and to see how an increasing temperature effects the membrane deflection.

4.2.1 Membrane Edge Length vs. Deflection.

Six different models were created for FEM modeling to simulate the behavior of a 1.0mm, 1.5mm, and 2.0mm square membrane each with device layer thicknesses of 5μm and 6μm. An appropriate mesh size was chosen based on the mesh analy-

sis performed earlier and simulations were run to measure the determine the initial deflection of the membrane at room temperature with no external force or pressure applied. The results are summarized below in table 2 and plotted in Figure 53.

Table 2. FEM Simulation results of initial membrane deflection

Device Layer Thickness	Membrane edge length	Deflection
5μm	1.0mm	10.46μm
	1.5mm	19.60μm
	2.0mm	27.78μm
6μm	1.0mm	8.24μm
	1.5mm	17.03μm
	2.0mm	26.29μm

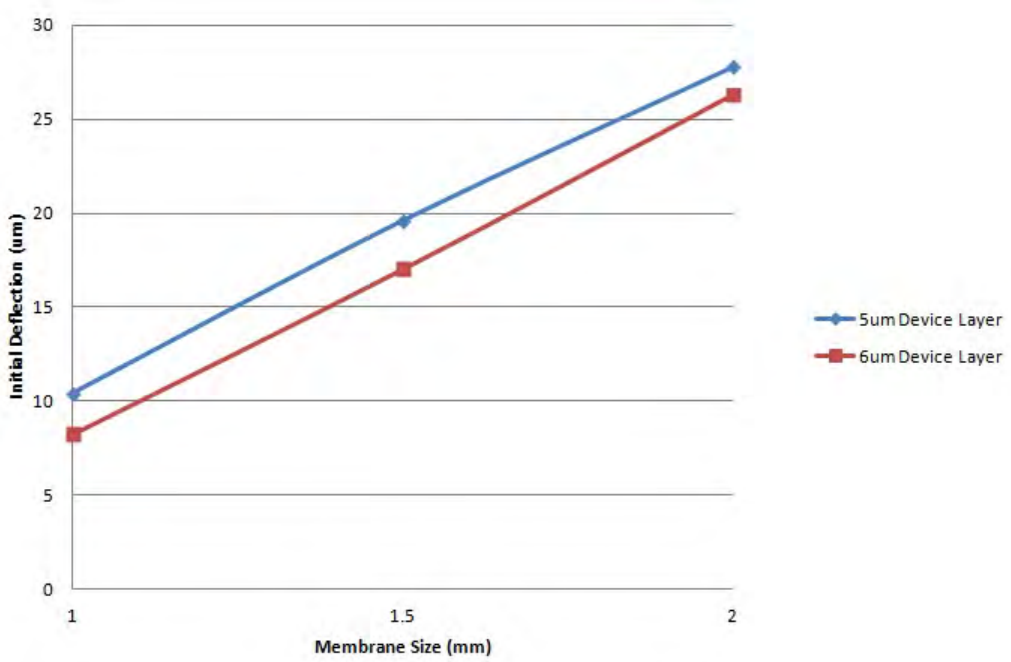

Figure 53. Plot of the FEM simulation initial membrane deflection with respect to membrane size and mechanical layer thickness.

4.2.2 Heater Temperature.

In order to tune the stiffness of the membranes, heat is applied to them by applying a voltage to a meandering resistor located on top of the membrane. As current flows through the resistor, its temperature increases due to Joule heating. The temperature of the membranes was measured under different applied voltages. Because of their different dimensions, the meandering resistors have different resistances. Because if this, one voltage level applied to the resistor of the 1.0mm membrane will have a different temperature profile than that of the same voltage applied to the 1.5mm or 2.0mm membranes. The temperatures of each different heater were measured with the infrared camera over a range of voltages. It was found that the smaller 1.0mm heater required less voltage to reach the same temperatures as the larger 1.5mm and 2.0mm membranes. This is due to the lower length of the resistor allows a higher current to flow for the same applied voltage. This higher current results in a higher power dissipation in the heater leading to higher temperatures for the same applie voltage. This is similarly the case looking at the 1.5mm compared to the 2.0mm heaters. The results are summarized in figure 54.

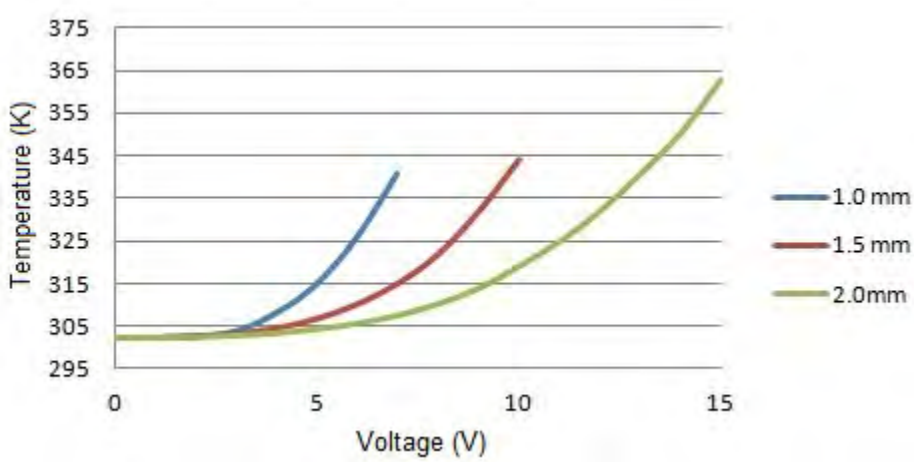

Figure 54. Plot of the measured membrane temperature vs. the applied voltage to the heater.

4.2.3 Temperature vs. Deflection.

With the buckled membrane in a stable state, additional simulations can be run analyze the membranes response to an increasing temperature. Beginning at 300K, the temperature of the membrane was increased by 100 K for each subsequent run. Analysis showed that the membrane increased in deflection from an initial 12μm at 300 K to approximately 32μm at 1200K. The cross-sectional profile of the membrane as it is deflected by temperature is shown in Figure 55.

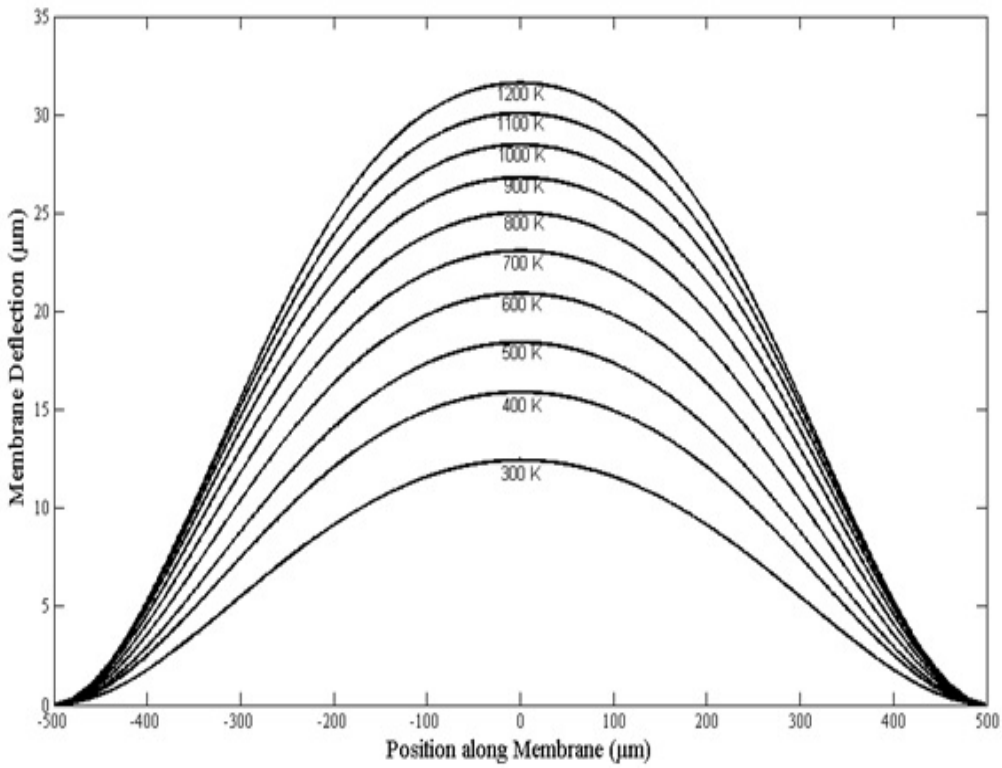

Figure 55. Cross-sectional profile of buckled membrane at different temperature applications ranging from 300K to 1200K.

4.3 Measured Results

All of the measurements done to analyze the behavior of the tunable pressure sensors was done on the Zygo white light interferometer. Deflection was measured under increasing temperature and applied pressures. Six different membrane configurations were measured and analyzed. The edge length of these square membranes varied from 1.0mm, 1.5mm, and 2.0mm each with a silicon mechanical layer thickness of 5μm or 6μm For each data point, an average of four different membranes is used.

4.3.1 Membrane Deflection vs Membrane Edge Length Measurement.

Measuring the membrane deflection vs. its edge length for both 5μm and 6μm thick mechanical layers with no applied temperature or pressure was the first test. Results showed that the 1.0mm, 5μm thick membrane has an initial deflection of 8.7μm and increases to 24.8μm when it's size is increased to 2.0mm. Likewise, results showed that the 1.0mm, 6μm thick membrane has an initial deflection of 7.36μm and increases to 23.48μm when it's size is increased to 2.0mm. The results of these measurements are summarized in table 3 and illustrated by Figure 56.

Table 3. Measured values of initial membrane deflection with at room temperature with no external force applied.

Device Layer Thickness	Membrane Edge Length	Deflection
5μm	1.0mm	9.3μm
	1.5mm	17.5μm
	2.0mm	24.8μm
6μm	1.0mm	7.36μm
	1.5mm	15.2μm
	2.0mm	26.29μm

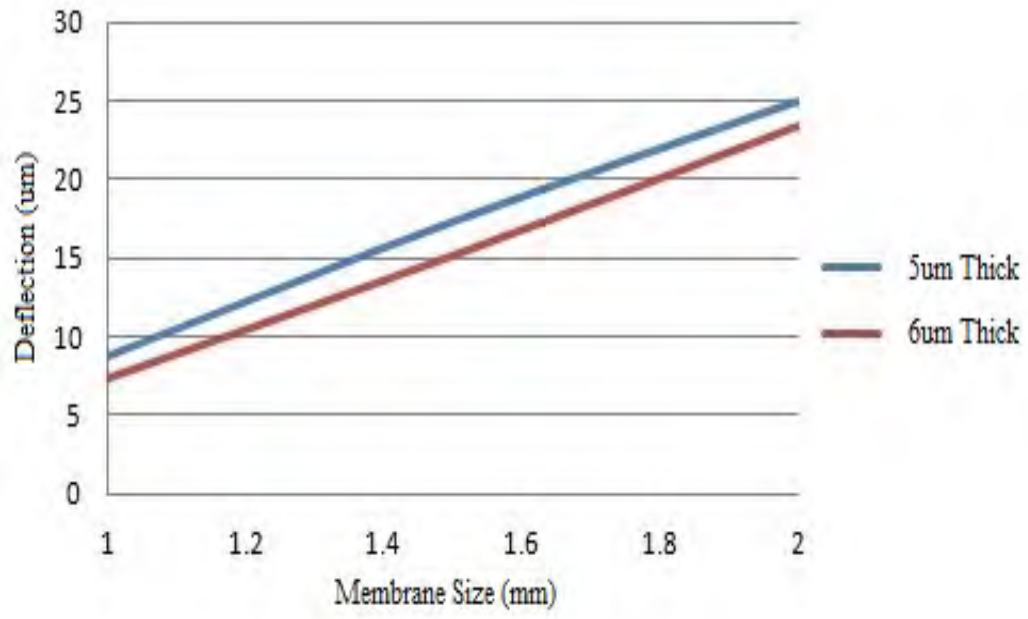

Figure 56. Plot of the initial membrane deflection vs. its size for 1.0mm, 1.5mm, and 2.0mm square membrane with 5μm (blue) and 6μm (red) thick silicon mechanical layers.

4.4 Buckled Membrane Stiffness Measurement

The stiffness of the buckled membrane was measured using a Femto Tools FT-WFSO2-CT probe station. This tool uses a piezoelectrically actuated force sensor to slowly push on the center of the membrane and measure the response force of the membrane. Recall that the stiffness is the change in force with respect to the change in deflection. This means that the slope of the response curve indicates the stiffness of the membrane. The results, illustrated in Figure 57, are consistent with what analytic analysis predicts.

As the force sensor initially begins pressing on the membrane, the response force increases demonstrating a region of positive stiffness. At a certain point (2) the response force begins to decrease as the force sensor continues to push further against the membrane indicating a region of negative stiffness. Eventually, the membrane is pushed past its snap-through point (3) and transitions to a buckled down position,

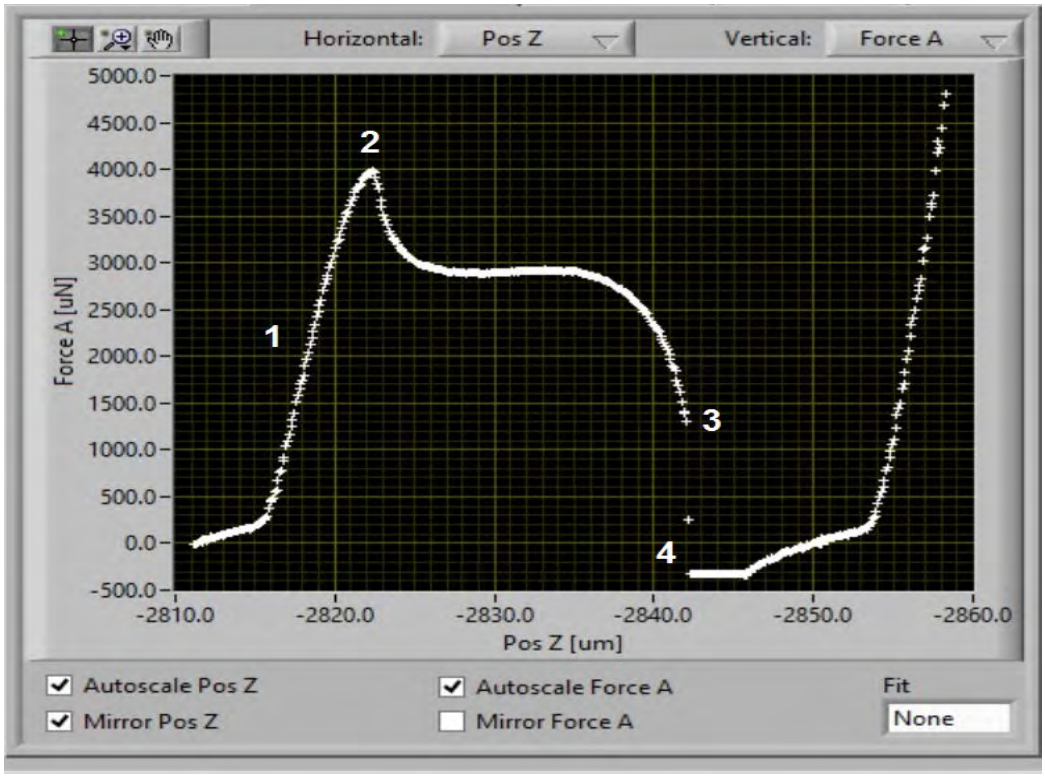

Figure 57. Plot of the force vs. displacement curve of a 1.5mm membrane showing regions of positive (1) and negative stiffness (2) as well as the snap through point (3).

leaving the force sensor out of contact with the membrane until it eventually reaches it again and continues to push the now inverted membrane outward (4).

4.5 Tunable Pressure Sensor Measurements

4.5.1 Deflection vs. Pressure.

Measuring the the deflection of the membrane with respect to applied pressure revealed is important to understanding the overall stiffness of the membrane. By applying pressure to membranes of different size and thickness, and measuring their deflection with the Zygo white light interferometer, it was shown that the smaller the membrane, the smaller its change in deflection was. For the 1.0mm, 5μm thick membrane it's deflection increased 6.57μm from 8.7μm at 0 psi applied up to 15.27μm at 10 psi applied. Likewise, the 1.5mm, 5μm thick membrane increased in deflection

from 17.5μm to 28.23μm, an increase of 10.73μm. The 2.0mm 5μm thick membrane deflection increased 14.33μm from 24.8μm to 39.13μm. These results are illustrated in Figure 58.

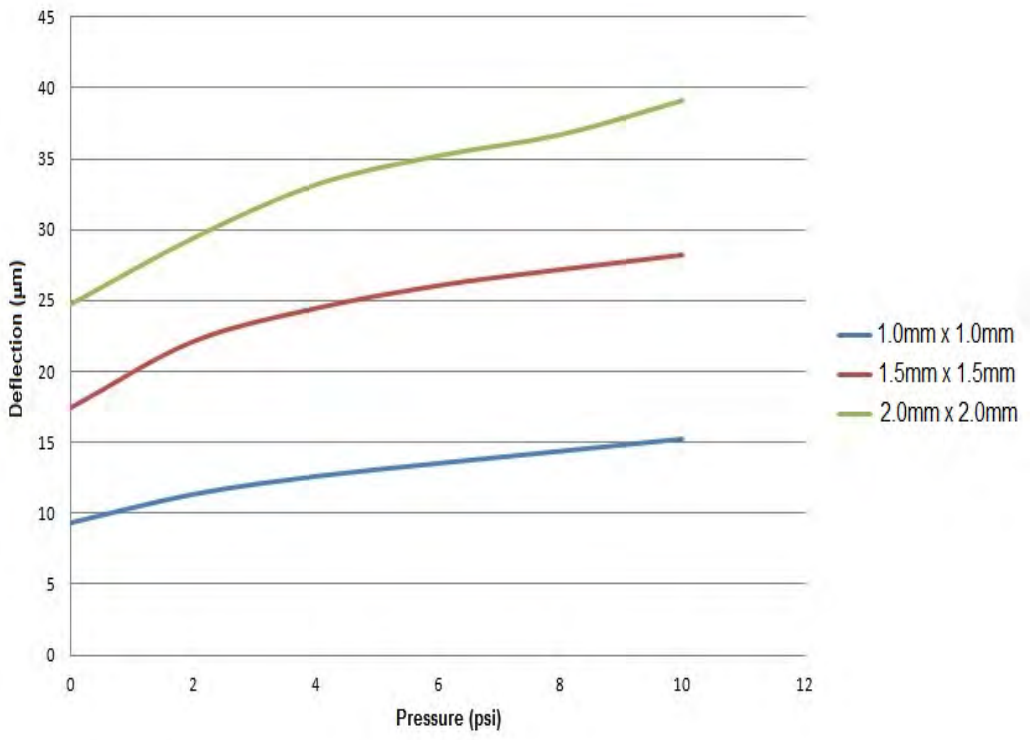

Figure 58. Plot of the deflection vs. applied pressure 5μm thick, 1.0mm, 1.5mm, and 2.0mm membranes. The 2.0mm membrane exhibits the largest range of deflection across the same applied pressures, demonstrating its lower overall stiffness

The corresponding 6μm thick membranes behave in the same fashion as their 5μm thick counterparts. For the 1.0mm, 5μm thick membrane it's deflection increased 5.66μm from 7.36μm at 0 psi applied up to 13.02μm at 10 psi applied. Likewise, the 1.5mm, 5μm thick membrane increased in deflection from 15.2μm to 22.98μm, an increase of 7.78μm. The 2.0mm 5μm thick membrane deflection increased 13.56μm from 23.48μm to 37.04μm. These results are illustrated in Figure 59. The measured results of all the membranes are summarized in table 4.

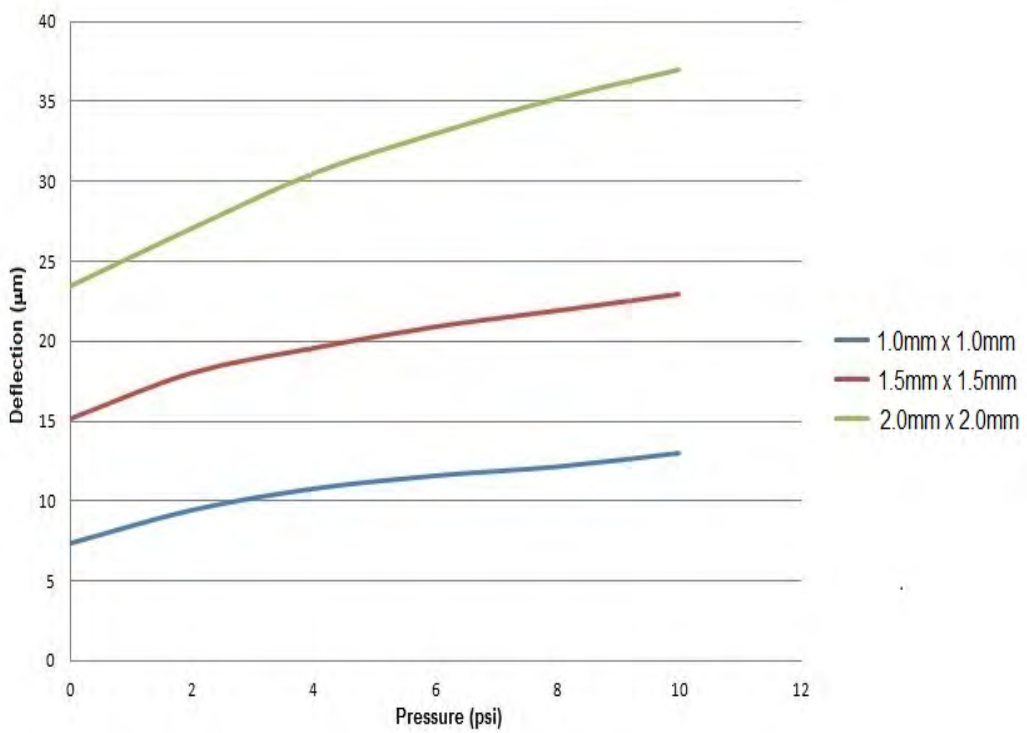

Figure 59. Plot of the deflection vs. applied pressure 6μm thick, 1.0mm, 1.5mm, and 2.0mm membranes. The 2.0mm membrane exhibits the largest range of deflection across the same applied pressures, demonstrating its lower overall stiffness

Table 4. Measured deflections for 1.0mm, 1.5mm, and 2.0mm membranes with 5μm and 6μm thicknesses

Thickness	Membrane Size	0psi	2psi	4psi	6psi	8psi	10psi
5μm	1.0mm	9.30μm	11.33μm	12.61μm	13.53μm	14.40μm	15.27μm
	1.5mm	17.50μm	22.15μm	24.48μm	26.08μm	27.20μm	28.23μm
	2.0mm	24.80μm	29.45μm	33.20μm	35.23μm	36.72μm	39.13μm
6μm	1.0mm	7.36μm	9.45μm	10.79μm	11.60μm	12.17μm	13.02μm
	1.5mm	15.20μm	18.07μm	19.62μm	20.95μm	21.95μm	22.98μm
	2.0mm	23.48μm	27.11μm	30.55μm	33.05μm	35.24μm	37.04μm

4.5.2 Deflection vs. Temperature.

The deflection of the membrane was measured with respect to the temperature applied via the resistive heater. Four different membranes of each size and thickness combination were measured as the temperature was increased and the results were averaged to obtain the deflection vs. temperature data.

Table 5 shows the results of the deflection vs. applied temperature for the 5μm and 6μm thick 1.0mm x 1.0mm membranes. These results are plotted in Figure 60. The 5μm thick membrane has an initial deflection of 7.905μm at 299.44K and a maximum deflection of 16.473μm at 315.88K. The 6μm thick membrane has an initial deflection of 6.256μm at 299.44K and a maximum deflection of 11.152μm at 315.88K.

Table 5. Deflection vs. Applied Temperature for 1.0mm x 1.0mm membranes.

Temperature (K)	Deflection (μm)	
	5μm	6μm
299.44	7.905	6.256
299.51	8.330	6.409
299.73	8.883	6.970
300.43	9.749	7.437
302.52	11.025	8.066
305.49	12.555	8.899
310.01	14.425	9.971
315.88	16.473	11.152

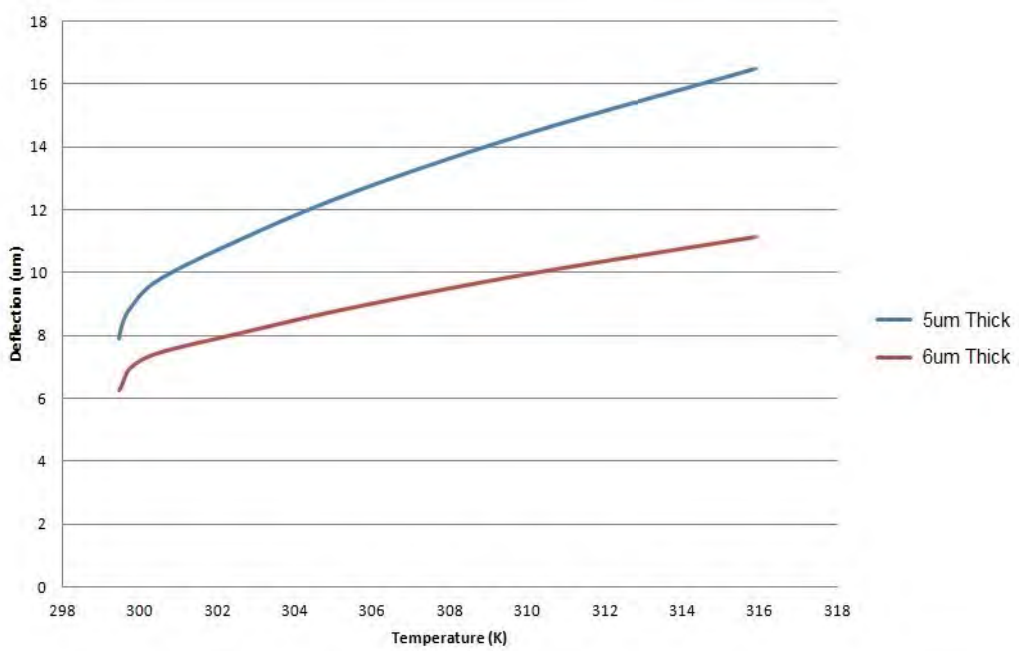

Figure 60. Deflection data for 1.0mm x 1.0mm membrane with 5μm and 6μm thick device layer.

Table 6 shows the results of the deflection vs. applied temperature for the 5μm and 6μm thick 1.5mm x 1.5mm membranes. These results are plotted in Figure 61.

Table 6. Deflection vs. Applied Temperature for 1.50mm x 1.50mm membranes.

Temperature (K)	Deflection (μm)	
	5μm	6μm
299.44	14.525	12.616
299.49	15.355	12.889
299.69	16.351	13.073
300.08	17.596	13.371
300.79	18.351	13.977
301.89	19.713	14.458
303.44	21.148	14.923
305.54	22.584	15.612
308.39	24.253	16.583
312.39	25.68	17.380
317.12	27.382	18.351

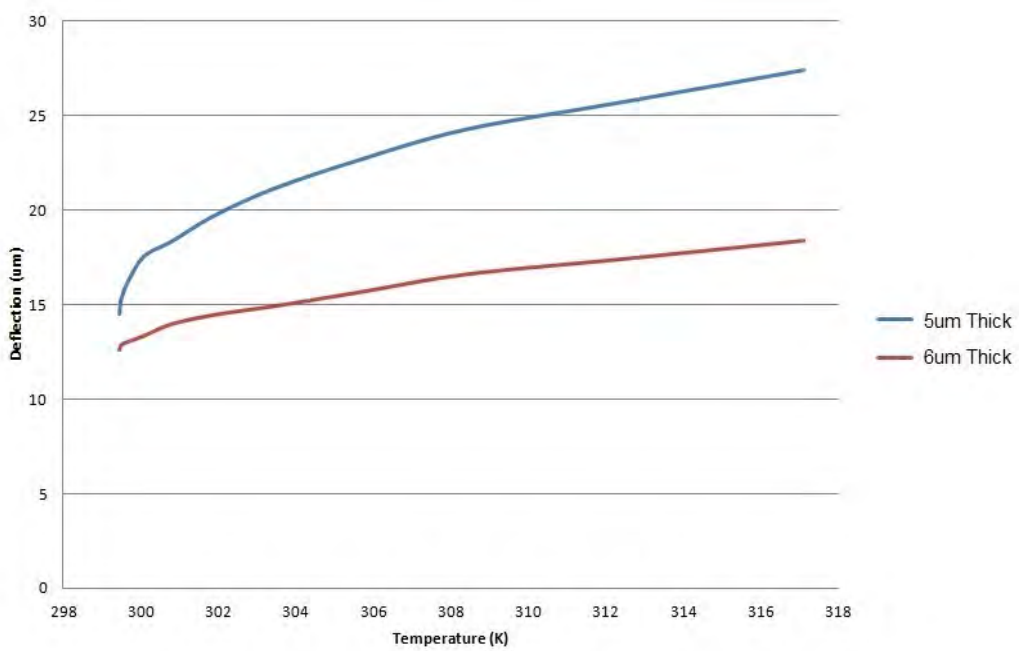

Figure 61. Deflection data for 1.5mm x 1.5mm membrane with 5μm and 6μm thick device layer.

The 5μm thick membrane has an initial deflection of 14.525μm at 299.44K and a maximum deflection of 27.382μm at 317.12K. The 6μm thick membrane has an

initial deflection of 12.616μm at 299.44K and a maximum deflection of 18.351μm at 317.12K.

Table 7 shows the results of the deflection vs. applied temperature for the 5μm and 6μm thick 2.0mm x 2.0mm membranes. These results are plotted in Figure 62. The 5μm thick membrane has an initial deflection of 19.840μm at 299.44K and a maximum deflection of 35.608μm at 324.11K. The 6μm thick membrane has an initial deflection of 18.784μm at 299.44K and a maximum deflection of 27.824μm at 324.11K.

Table 7. Deflection vs. Applied Temperature for 2.00mm x 2.00mm membranes.

Temperature (K)	Deflection (μm)	
	5μm	6μm
299.44	19.840	18.784
299.45	20.080	18.848
299.57	20.328	19.000
299.80	20.688	19.208
300.13	21.232	19.456
300.65	21.928	19.84
301.33	22.768	20.408
302.24	23.832	20.816
303.44	24.992	21.424
305.00	26.176	21.968
307.18	27.44	22.872
309.50	28.928	23.744
312.32	30.352	24.616
315.72	32.080	25.600
319.37	33.752	26.680
324.11	35.608	27.824

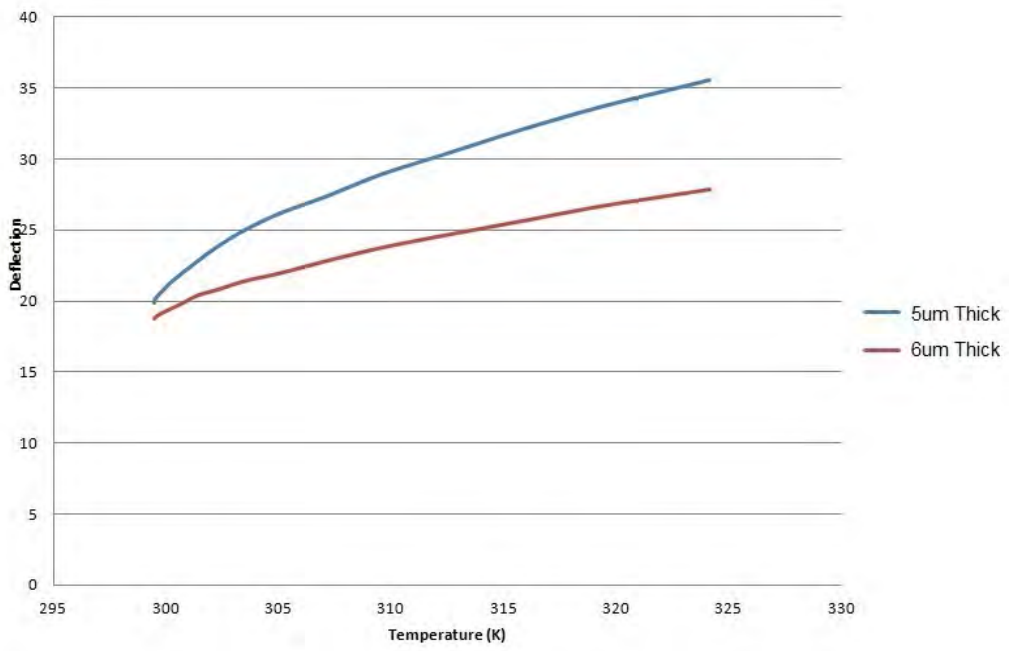

Figure 62. Deflection data for 2.0mm x 2.0mm membrane with 5μm and 6μm thick device layer.

4.5.3 Deflection vs. Pressure and Temperature.

In order to quantify the effects of thermal stiffness tuning on the sensitivity of the pressure sensor, the membrane deflection was measured with respect to varying pressure and temperature. The measurements were repeated on four different membranes and averaged for each.

Table 8 shows the results of the deflection measurements over an applied pressure range from zero to ten psi and a range of applied temperature from 299.44K to 315.88K for a 5μm thick, 1.0mm x 1.0mm membranes. These results are plotted in Figure 63.

Table 8. Table of measured deflections for a 5μm thick, 1.0mm x 1.0mm membrane.

Temperature (K)	Pressure (psi)					
	0	2	4	6	8	10
299.44	9.30	11.33	12.61	13.53	14.40	15.27
299.51	9.80	11.72	12.75	13.61	14.66	15.36
299.73	10.45	12.22	13.12	13.95	14.92	15.62
300.43	11.47	12.93	13.88	14.47	15.54	16.04
302.52	12.97	14.19	14.92	15.54	16.39	16.98
305.49	14.77	15.85	16.22	16.82	17.70	18.19
310.01	16.97	17.61	17.89	18.30	19.20	19.35
315.88	19.38	19.76	20.14	20.44	20.92	21.18

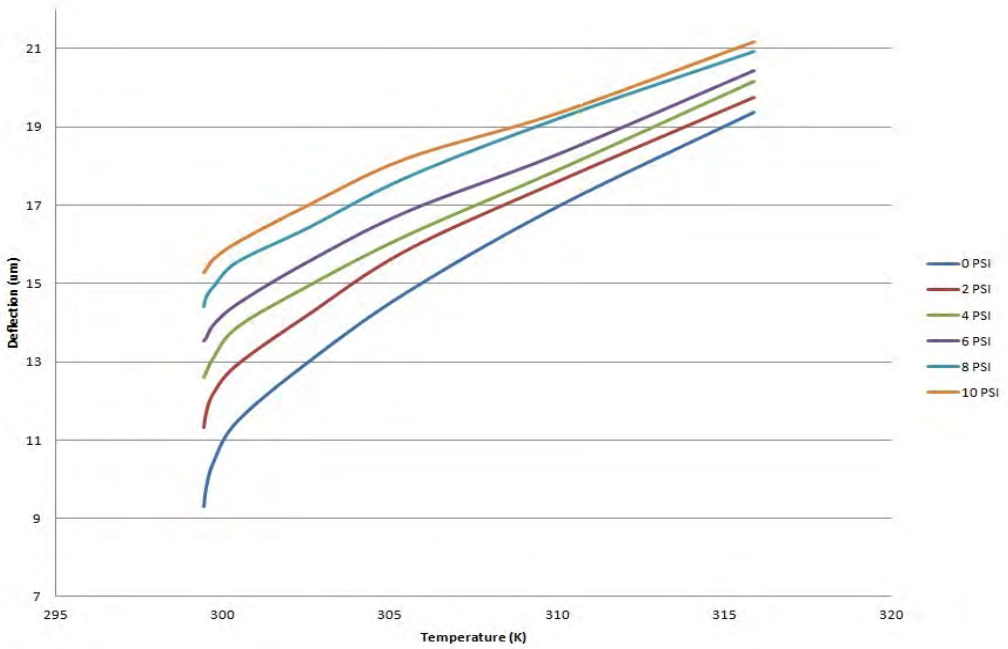

Figure 63. Deflection data for a 5μm thick, 1.0mm x 1.0mm membrane.

Table 9 shows the results of the deflection measurements over an applied pressure range from zero to ten psi and a range of applied temperature from 299.44K to 315.88K for a 6μm thick, 1.0mm x 1.0mm membranes. These results are plotted in Figure 64.

Table 9. Table of measured deflections for a 6μm thick, 1.0mm x 1.0mm membrane.

Temperature (K)	Pressure (psi)					
	0	2	4	6	8	10
299.44	7.36	9.44	10.79	11.60	12.17	13.02
299.51	7.54	9.50	10.89	11.64	12.22	13.05
299.73	8.19	9.74	11.03	11.89	12.65	13.23
300.43	8.75	10.17	11.47	12.17	12.87	13.54
302.52	9.49	10.82	12.00	12.55	13.47	13.93
305.49	10.47	11.67	12.56	13.32	14.08	14.47
310.01	11.73	12.77	13.36	14.13	14.77	15.30
315.88	13.12	13.82	14.74	15.13	15.55	16.27

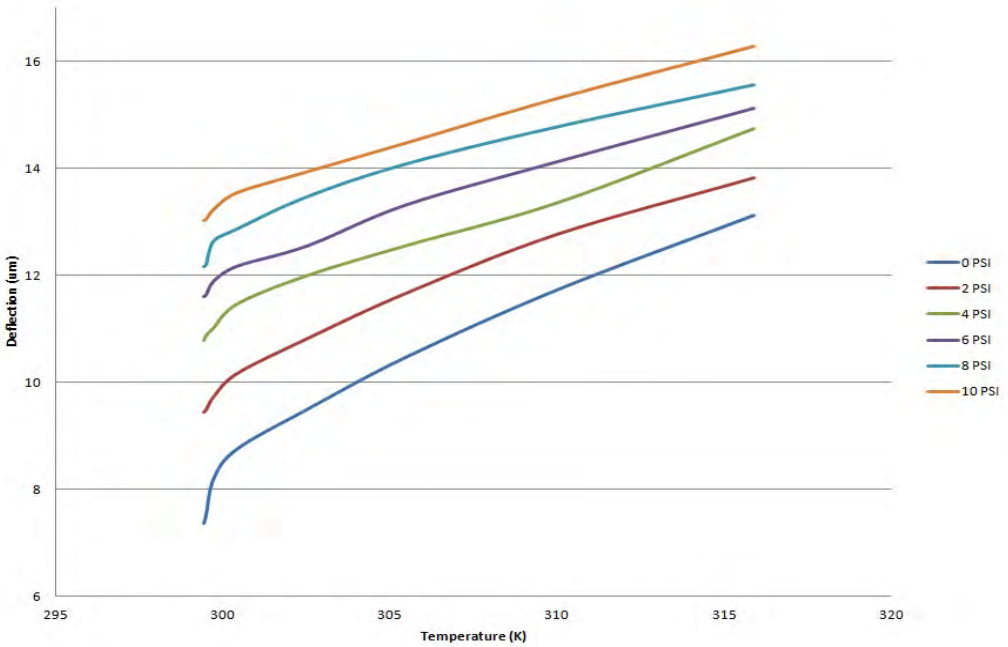

Figure 64. Deflection data for a 6μm thick, 1.0mm x 1.0mm membrane.

Table 10 shows the results of the deflection measurements over an applied pressure range from zero to ten psi and a range of applied temperature from 299.44K to 317.12K for a 5μm thick, 1.5mm x 1.5mm membranes. These results are plotted in Figure 65.

Table 10. Table of measured deflections for a 5μm thick, 1.5mm x 1.5mm membrane.

Temperature (K)	Pressure (psi)					
	0	2	4	6	8	10
299.44	17.50	22.15	24.48	26.08	27.20	28.23
299.49	18.50	22.85	24.55	26.13	27.22	28.66
299.69	19.70	23.45	24.83	26.20	27.25	28.91
300.08	21.20	24.25	25.36	26.64	27.51	29.33
300.79	22.11	24.98	26.49	27.73	28.20	29.47
301.89	23.75	25.94	27.43	28.60	29.22	30.15
303.44	25.48	27.25	28.61	29.63	29.97	31.08
305.54	27.21	28.54	30.02	30.60	31.14	32.11
308.39	29.22	30.34	31.65	31.95	33.03	33.61
312.39	30.94	32.10	33.36	33.65	34.65	34.89
317.12	32.99	34.45	35.38	35.75	35.97	36.47

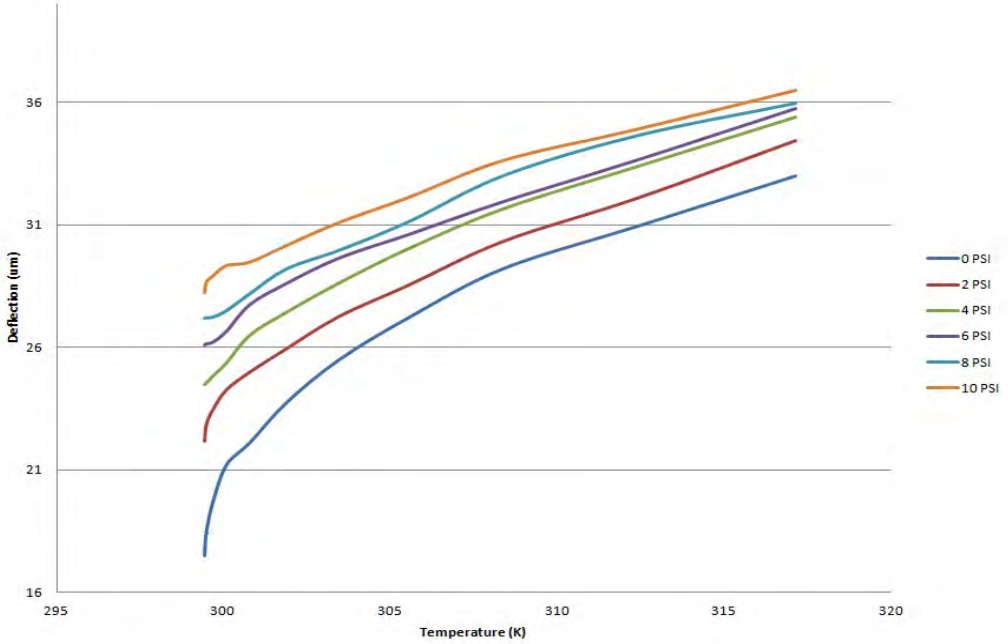

Figure 65. Deflection data for 5μm thick, 1.5mm x 1.5mm membrane.

Table 11 shows the results of the deflection measurements over an applied pressure range from zero to ten psi and a range of applied temperature from 299.44K to 317.12K for a 6μm thick, 1.5mm x 1.5mm membranes. These results are plotted in Figure 66.

Table 11. Table of measured deflections for a 6μm thick, 1.5mm x 1.5mm membrane.

Temperature (K)	Pressure (psi)					
	0	2	4	6	8	10
299.44	15.20	18.07	19.62	20.95	21.95	22.98
299.49	15.53	18.13	19.67	21.10	22.09	23.04
299.69	15.75	18.29	19.80	21.23	22.20	23.16
300.08	16.11	18.53	19.98	21.29	22.31	23.33
300.79	16.84	18.88	20.25	21.60	22.56	23.64
301.89	17.42	19.45	20.69	22.00	23.08	23.99
303.44	17.98	20.05	21.47	22.39	23.42	24.37
305.54	18.80	20.77	21.95	23.11	24.06	24.90
308.39	19.98	21.47	22.73	23.67	24.61	25.54
312.39	20.94	22.63	23.43	24.51	25.61	26.26
317.12	22.11	23.64	24.42	25.44	26.08	27.05

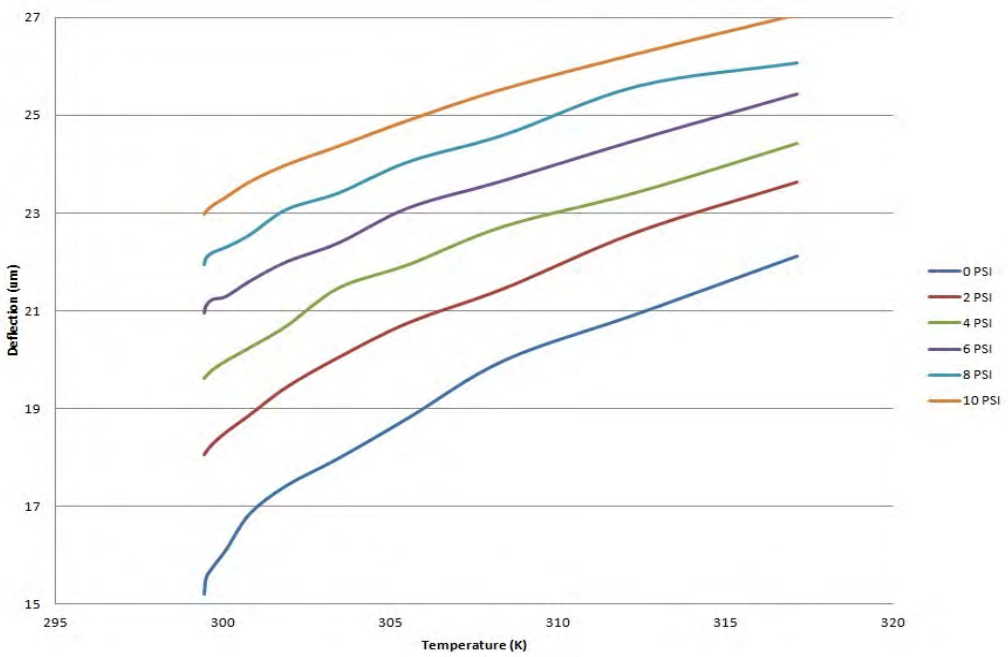

Figure 66. Deflection data for a 6μm thick, 1.5mm x 1.5mm membrane.

Table 12 shows the results of the deflection measurements over an applied pressure range from zero to ten psi and a range of applied temperature from 299.44K to 324.11K for a 5μm thick, 2.0mm x 2.0mm membranes. These results are plotted in Figure 67.

Table 12. Table of measured deflections for a 5μm thick, 2.0mm x 2.0mm membrane.

Temperature (K)	Pressure (psi)					
	0	2	4	6	8	10
299.44	24.80	29.45	33.20	35.22	36.72	39.13
299.45	25.10	29.49	33.78	35.25	36.89	39.29
299.57	25.41	29.67	33.92	35.36	37.17	39.35
299.80	25.86	29.98	34.11	35.59	37.57	39.40
300.13	26.54	30.45	34.59	35.94	37.82	39.70
300.65	27.41	31.06	34.94	36.42	38.22	40.07
301.33	28.46	31.85	35.60	37.01	38.71	40.51
302.24	29.79	32.72	36.32	37.68	39.42	41.14
303.44	31.24	33.83	37.22	38.53	40.15	41.85
305.00	32.72	35.15	38.29	39.42	41.01	42.56
307.18	34.29	36.56	39.45	40.54	42.11	43.62
309.50	36.15	38.18	40.82	41.77	43.21	44.57
312.32	37.94	40.04	42.38	43.44	44.61	45.86
315.72	40.10	41.86	44.14	44.92	45.99	47.22
319.37	42.19	43.55	45.88	46.59	47.46	48.69
324.11	44.51	46.11	47.78	48.20	49.21	50.01

Table 13 shows the results of the deflection measurements over an applied pressure range from zero to ten psi and a range of applied temperature from 299.44K to 324.11K for a 6μm thick, 2.0mm x 2.0mm membranes. These results are plotted in Figure 68.

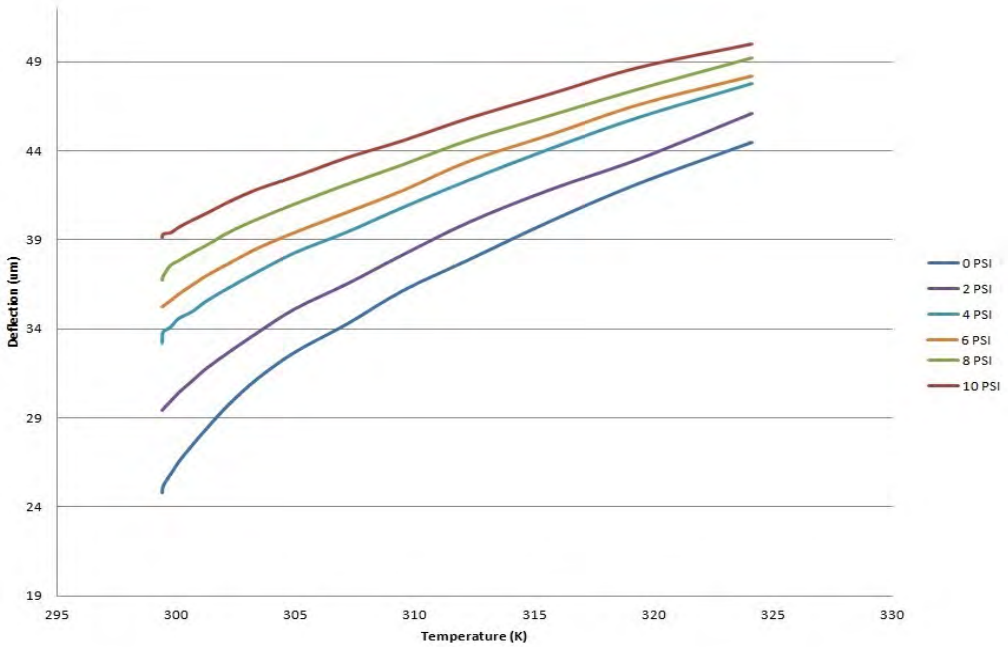

Figure 67. Deflection data for 2mm x 2mm membrane with 5μm thick device layer.

Table 13. Table of measured deflection of 6μm thick, 2.0mm x 2.0mm membrane.

Temperature (K)	Pressure (psi)					
	0	2	4	6	8	10
299.44	23.48	27.11	30.55	33.04	35.24	37.04
299.45	23.56	27.16	30.61	33.08	35.28	37.06
299.57	23.75	27.23	30.69	33.14	35.36	37.10
299.80	24.01	27.32	30.80	33.18	35.45	37.20
300.13	24.32	27.56	30.94	33.40	35.61	37.40
300.65	24.80	27.98	31.33	33.94	35.69	37.61
301.33	25.51	28.68	31.51	34.18	36.10	37.83
302.24	26.02	29.19	31.94	34.53	36.20	38.18
303.44	26.78	29.84	32.61	34.99	36.93	38.56
305.00	27.46	30.43	33.29	35.50	37.40	39.02
307.18	28.59	31.33	33.99	36.13	37.65	39.47
309.50	29.68	32.15	34.65	36.78	38.53	40.04
312.32	30.77	33.13	35.50	37.47	39.22	40.60
315.72	32.00	34.20	36.45	38.32	39.90	41.41
319.37	33.35	35.29	37.47	39.20	40.79	42.17
324.11	34.78	36.40	38.44	40.21	41.77	43.01

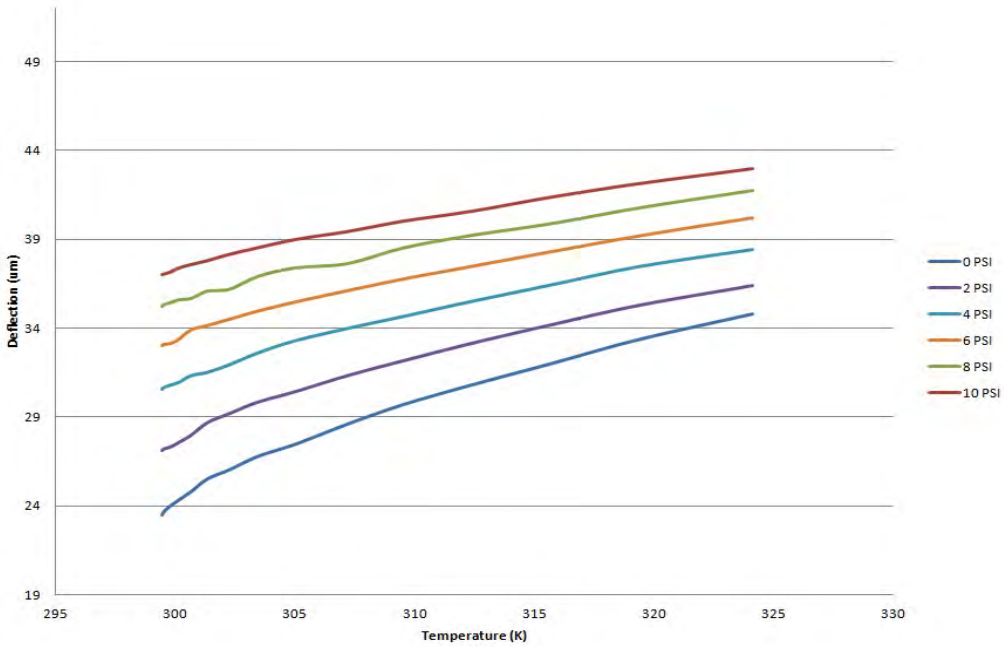

Figure 68. Deflection data for a 6μm thick, 2.0mm x 2.0mm membrane.

4.5.4 Pressure Sensitivity.

The sensitivity of the pressure sensor is the ratio of its deflection to the pressure applied. A pressure sensor that is more sensitive will deflect further than a less sensitive pressure sensor will for the same applied pressure. By thermally tuning the stiffness of the buckled membrane, the sensitivity is also tuned.

The sensitivity was quantified by taking the overall range of the membrane deflection from 0 psi to 10 psi with no heat. It can be seen here that while each configuration of pressure sensor has a unique curve, all of them are found to have a decreasing sensitivity over their range of applied temperatures.

Table 14 shows the pressure sensitivity of both a 5μm and 6μm thick, 1.0mm by 1.0mm pressure sensor over a range of temperatures from 299.44K to 315.88K. The 5μm thick pressure sensor shows a 69.8 percent decrease in sensitivty over this range of temperature while the 6μm thick pressure sensor shows a 44.3 percent decrease in sensitivity over the same temperature range. These results are plotted in Figure 69.

Table 14. Sensitivity vs. Applied Temperature for both 5μm and 6μm thick, 1.0mm x 1.0mm membranes.

Temperature (K)	Sensitivity (μm/psi)	
	5μm	6μm
299.44	0.597	0.566
299.51	0.556	0.551
299.73	0.517	0.503
300.43	0.457	0.479
302.52	0.401	0.444
305.49	0.342	0.400
310.01	0.238	0.357
315.88	0.180	0.315

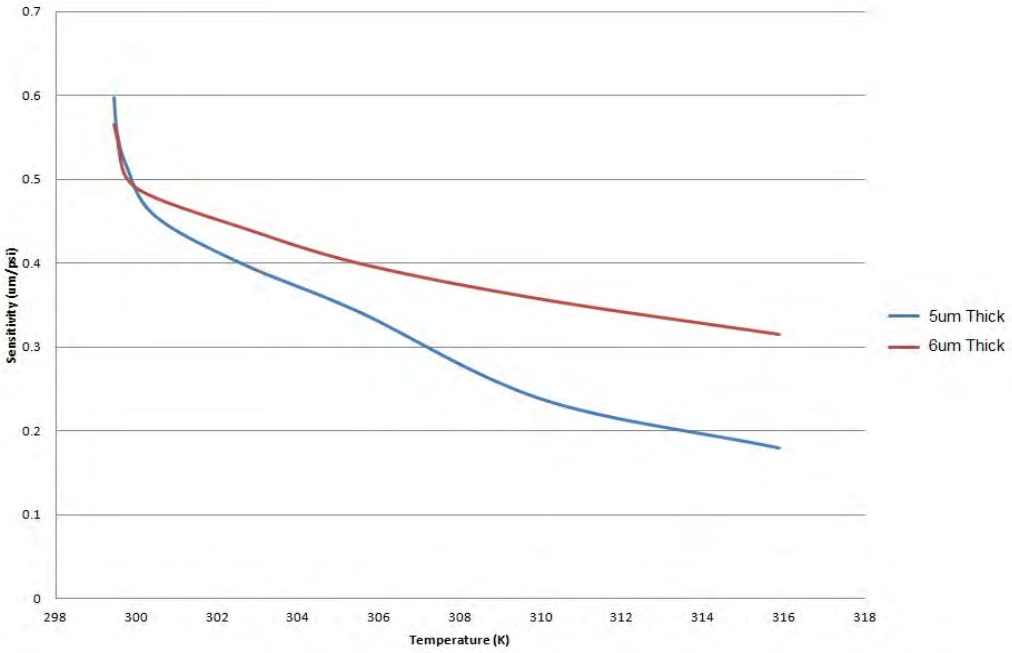

Figure 69. Plot of the sensitivity of a 1.0mm x 1.0mm membrane with a 5.0μm and 6.0μm thick device layer.

Table 15 shows the pressure sensitivity of both a 5μm and 6μm thick, 1.5mm by 1.5mm pressure sensor over a range of temperatures from 299.44K to 317.12K. The 5μm thick pressure sensor shows a 67.6 percent decrease in sensitivty over this range of temperature while the 6μm thick pressure sensor shows a 36.5 percent decrease in sensitivity over the same temperature range. These results are plotted in Figure 70.

Table 15. Sensitivity vs. Applied Temperature for both 5μm and 6μm thick, 1.5mm x 1.5mm membranes.

Temperature (K)	Sensitivity (μm/psi	
	5μm	6μm
299.44	1.073	0.778
299.49	1.016	0.751
299.69	0.921	0.741
300.08	0.813	0.722
300.79	0.736	0.680
301.89	0.640	0.657
303.44	0.560	0.639
305.54	0.490	0.609
308.39	0.440	0.556
312.39	0.395	0.532
317.12	0.348	0.494

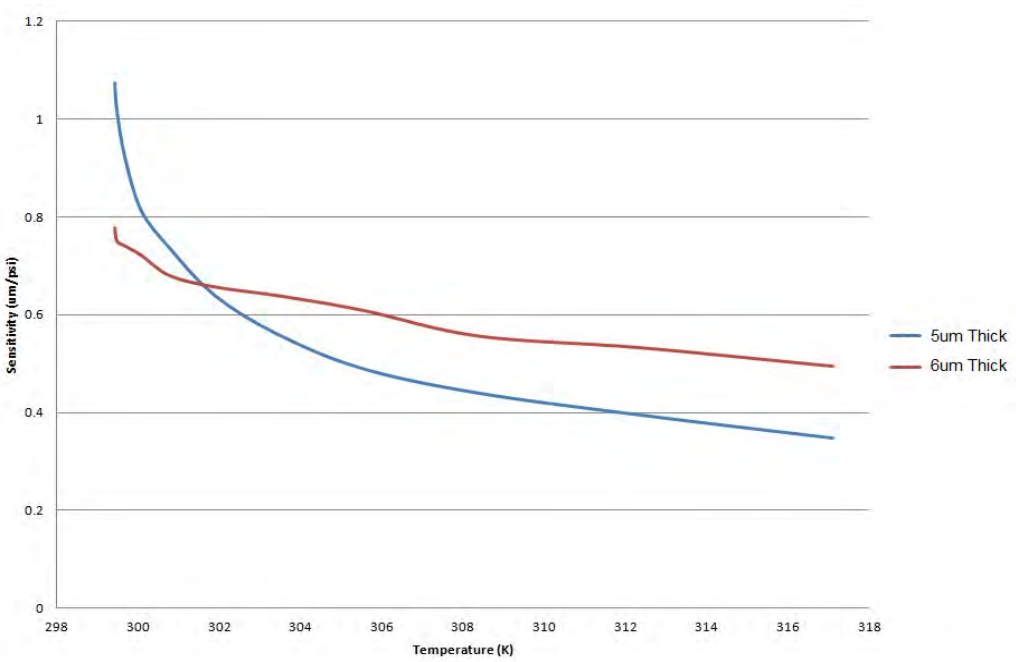

Figure 70. Plot of the sensitivity of a 1.5mm x 1.5mm membrane with a 5.0μm and 6.0μm thick device layer.

Table 16 shows the pressure sensitivity of both a 5μm and 6μm thick, 1.5mm by 1.5mm pressure sensor over a range of temperatures from 299.44K to 324.11K. The 5μm thick pressure sensor shows a 61.6 percent decrease in sensitivty over this range of temperature while the 6μm thick pressure sensor shows a 39.3 percent decrease in sensitivity over the same temperature range. These results are plotted in Figure 71.

Table 16. Sensitivity vs. Applied Temperature for both 5μm and 6μm thick, 2.00mm x 2.00mm membranes.

Temperature (K)	Sensitivity (μm/psi	
	5μm	6μm
299.44	1.433	1.356
299.45	1.419	1.350
299.57	1.394	1.335
299.80	1.354	1.319
300.13	1.316	1.309
300.65	1.266	1.281
301.33	1.205	1.232
302.24	1.135	1.216
303.44	1.061	1.178
305.00	0.984	1.156
307.18	0.932	1.088
309.50	0.841	1.037
312.32	0.792	0.983
315.72	0.712	0.941
319.37	0.650	0.882
324.11	0.550	0.823

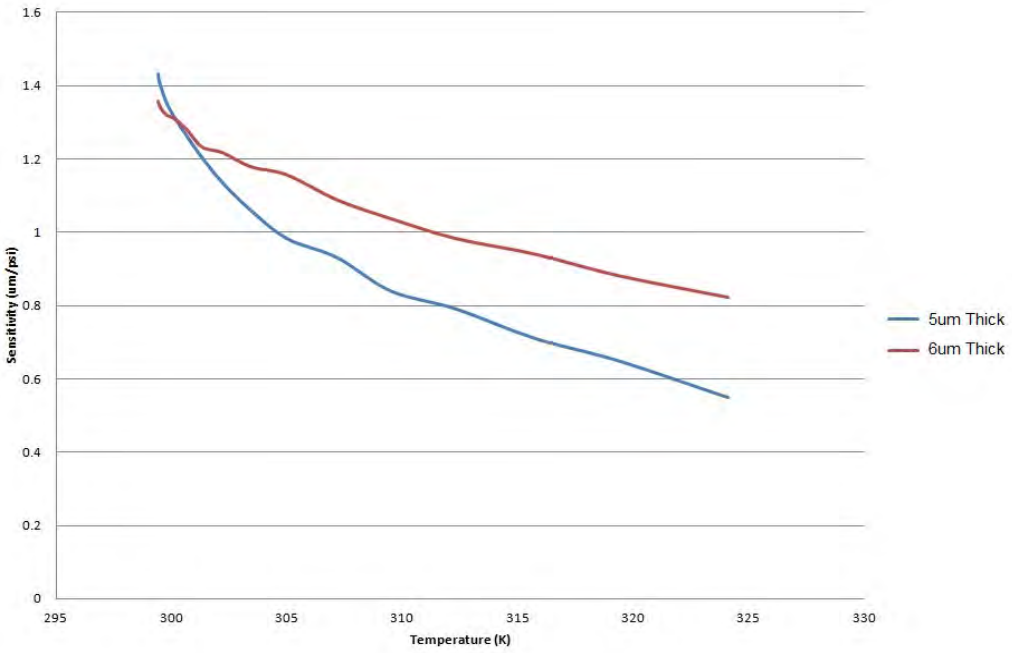

Figure 71. Plot of the sensitivity of a 2.0mm x 2.0mm membrane with a 5.0μm and 6.0μm thick device layer.

4.5.5 Volume Actuation.

The volume under the membrane as a function is determined by applying a measured membrane deflection to equation 6. Table 17 shows the volume results for both the 5μm and 6μm thick 1.0mm membrane as it is actuated over a range of temperatures from 299.44K to 315.88K. The 5μm thick membrane has an initial volume of 2.170x10$^7\mu$m^3 and a maximum volume of 4.525x10$^7\mu$m^3. The 6μm thick has an initial volume of 1.719x10$^7\mu$m^3 and a maximum volume of 3.064x10$^7\mu$m^3. These results are plotted in Figure 72.

Table 17. Volume vs. Temperature of a 5μm and 6μm thick, 1.0mm x 1.0mm membrane.

Temperature (K)	Volume (μm^3)	
	5μm	6μm
299.44	2.172e7	1.719e7
299.51	2.288e7	1.761e7
299.73	2.441e7	1.915e7
300.43	2.678e7	2.044e7
302.52	3.029e7	2.216e7
305.49	3.449e7	2.445e7
310.01	3.963e7	2.739e7
315.88	4.526e7	3.064e7

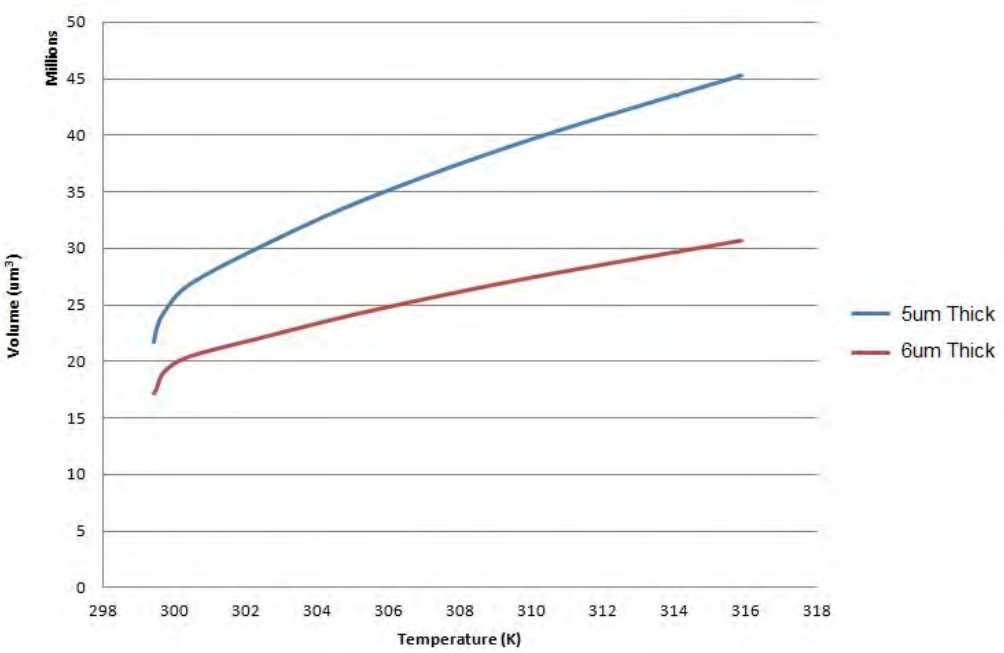

Figure 72. Plot of the membrane volume vs. temperature for a 1.0mm x 1.0mm membrane.

Table 18 shows the volume results for both the 5μm and 6μm thick 1.5mm membrane as it is actuated over a range of temperatures from 299.44K to 317.11K. The 5μm thick membrane has an initial volume of 9.196x10$^7\mu$m^3 and a maximum volume of 1.733x10$^8\mu$m^3. The 6μm thick has an initial volume of 7.987x10$^7\mu$m^3 and a maximum volume of 1.162x10$^8\mu$m^3. These results are plotted in Figure 73.

Table 18. Volume vs. Temperature of a 5μm and 6μm thick, 1.5mm x 1.5mm membrane.

Temperature (K)	Volume (μm^3)	
	5μm	6μm
299.44	9.196e7	7.987e7
299.49	9.721e7	8.161e7
299.68	1.035e8	8.276e7
300.08	1.114e8	8.465e7
300.79	1.116e8	8.849e7
301.88	1.248e8	9.154e7
303.44	1.339e8	9.448e7
305.54	1.429e8	9.884e7
308.39	1.535e8	1.049e8
312.39	1.625e8	1.100e8
317.11	1.733e8	1.162e8

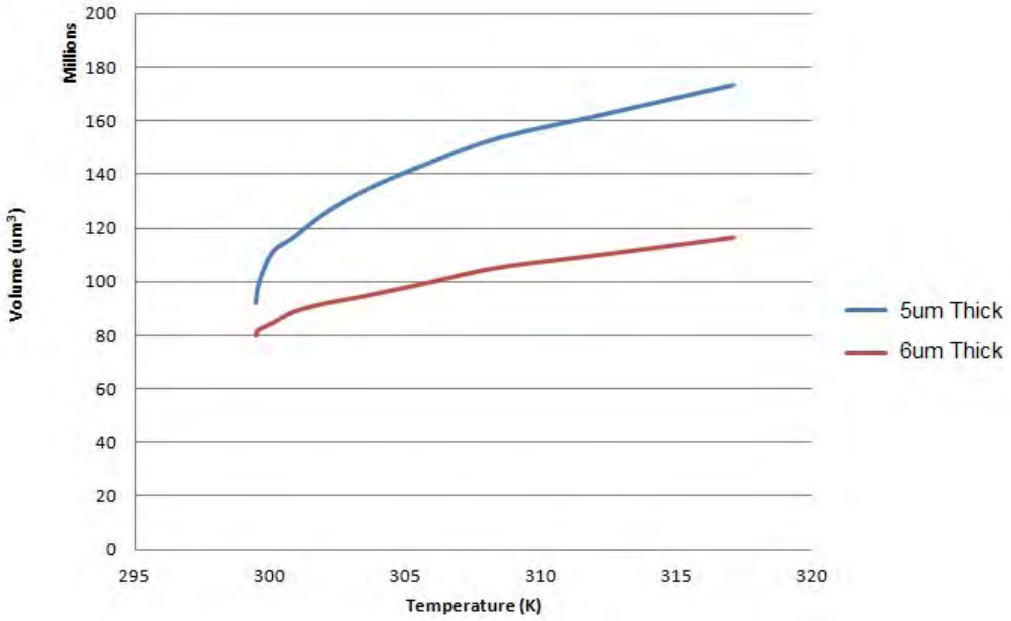

Figure 73. Plot of the membrane volume vs. temperature for a 1.5mm x 1.5mm membrane.

Table 19 shows the volume results for both the 5μm and 6μm thick 1.5mm membrane as it is actuated over a range of temperatures from 299.44K to 324.11K. The 5μm thick membrane has an initial volume of 2.317x10$^8\mu$m^3 and a maximum volume of 4.158x10$^8\mu$m^3. The 6μm thick has an initial volume of 2.193x10$^8\mu$m^3 and a maximum volume of 3.249x10$^8\mu$m^3. These results are plotted in Figure 74.

Table 19. Volume vs. Temperature of a 5μm and 6μm thick, 2.0mm x 2.0mm membrane.

Temperature (K)	Volume (μm^3)	
	5μm	6μm
299.44	2.317e8	2.193e8
299.45	2.344e8	2.201e8
299.57	2.373e8	2.219e8
299.79	2.416e8	2.243e8
300.12	2.479e8	2.272e8
300.65	2.651e8	2.317e8
301.33	2.659e8	2.383e8
302.24	2.783e8	2.431e8
303.44	2.918e8	2.502e8
305.00	3.057e8	2.565e8
307.18	3.204e8	2.671e8
309.49	3.378e8	2.773e8
312.32	3.544e8	2.874e8
315.72	3.746e8	2.989e8
319.37	3.941e8	3.115e8
324.11	4.158e8	3.249e8

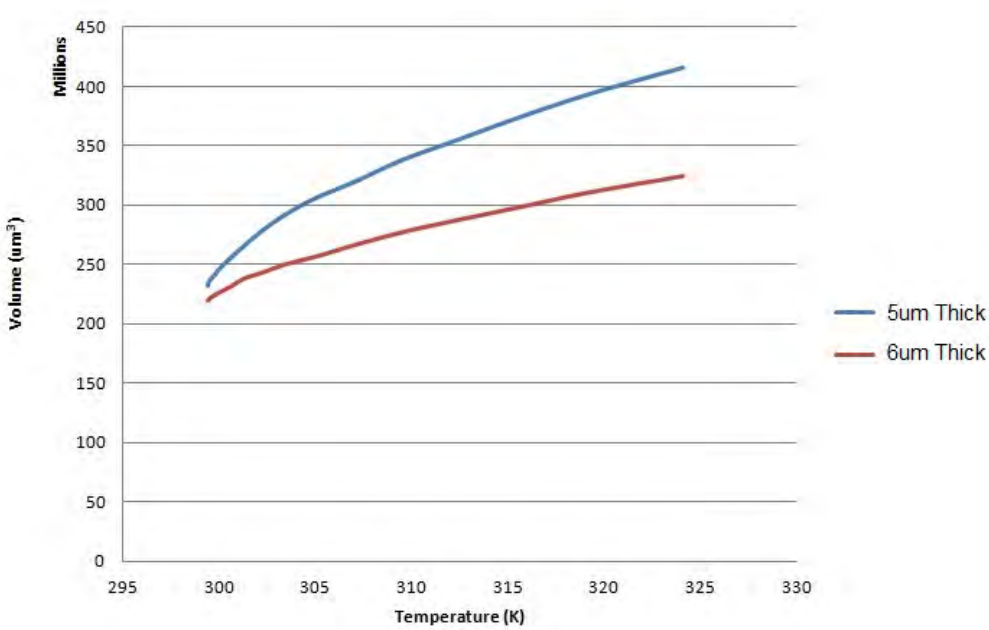

Figure 74. Plot of the membrane volume vs. temperature for a 2.0mm x 2.0mm membrane.

4.6 Bonding and Integration Results

4.6.1 SU-8 Bonding Results.

The samples were all tested to the point at which the bond of the SU-8 pads failed, and the tensile force at this point was recorded. Statistical analysis of this raw data indicated that there was a direct correlation between UV exposure dose and separation force. A trend-line was fitted to this raw data (Figure 75) and a two-sided t-test determined with 90% confidence that the slope of this line was non-zero. Equation 27 models the trend-line, determined through regression analysis,

$$Y = 0.0367 + 0.0779X, \tag{27}$$

where Y is the separation force in Newtons and X is the UV exposure time in seconds. This model was found to have a coefficient of correlation (R^2) of 0.31, meaning that 31% of the variability of the separation force is can be attributed to the UV exposure dosage.

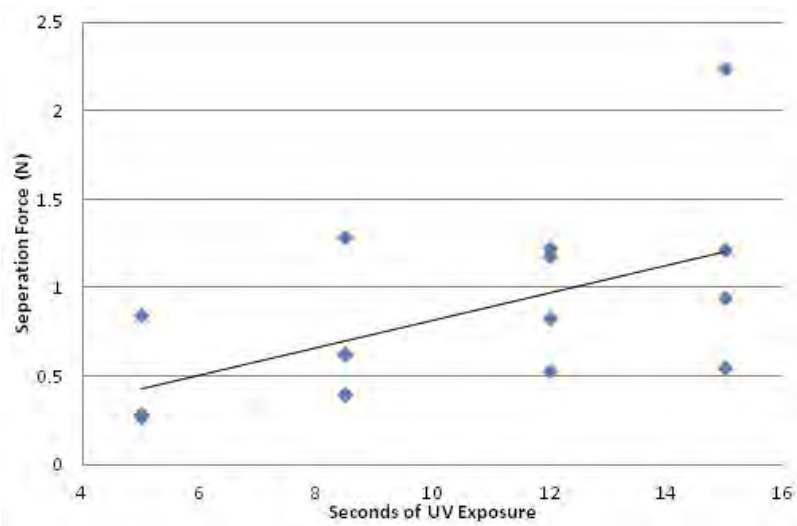

Figure 75. A predictor trend-line fitted to raw data from the separation testing was found to be non-zero with 90% confidence.

4.6.2 Etch Resiliency of Cross-linked SU-8.

The cross-linked SU-8 materials, processed during this study, were further investigated to assess their resiliency to plasma etching. The thicknesses of un-bonded, cross-linked SU-8 structures were initially measured using a KLA Tencor Alpha IQ Step surface profilometer. The samples were etched in an O_2 plasma asher for 5 minutes at 100 watts with film thickness being recorded after etching. The samples were then placed back in the plasma asher for 15 minutes at 100 watts with the subsequent thicknesses of the SU-8 structures being recorded. Five structures were measured for each UV dosage with the average thicknesses per dosage plotted in Figure 76.

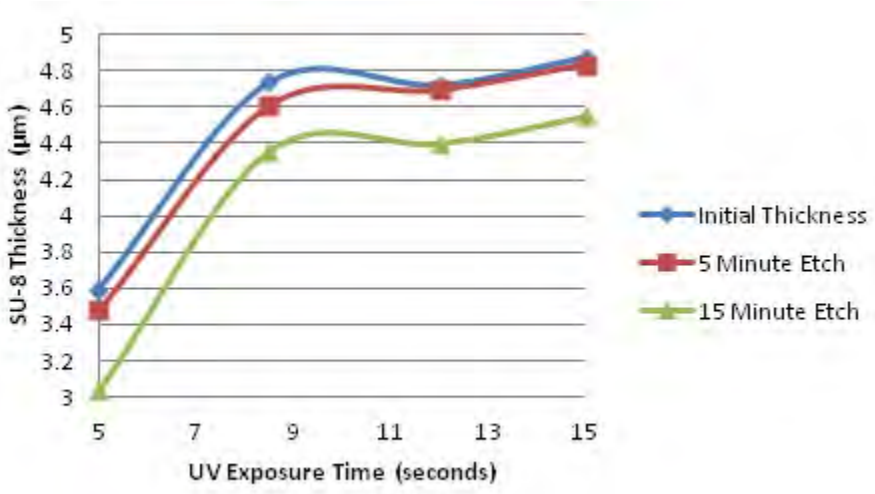

Figure 76. Plot of the average SU-8 thicknesses with respect to UV exposure time for the initial thickness, following a 5 minute plasma etch, and following a 15 minute plasma etch.

4.7 Multidirectional actuator

4.7.1 Thermal Results.

The localized heating of individual quadrants of the membrane was investigated using a thermal camera. The results show that the membrane undergoes localized

heating under the heater as expected and that the remaining three quadrants exhibit rise in temperature that is 88% less than the temperature rise of the hot quadrant. The heat is restricted to this region because the substrate surrounding the membrane on two sides of the heated quadrant acts as a heat sink, and draws the heat away from the rest of the membrane. This can be seen as the light blue region surrounding the membrane.

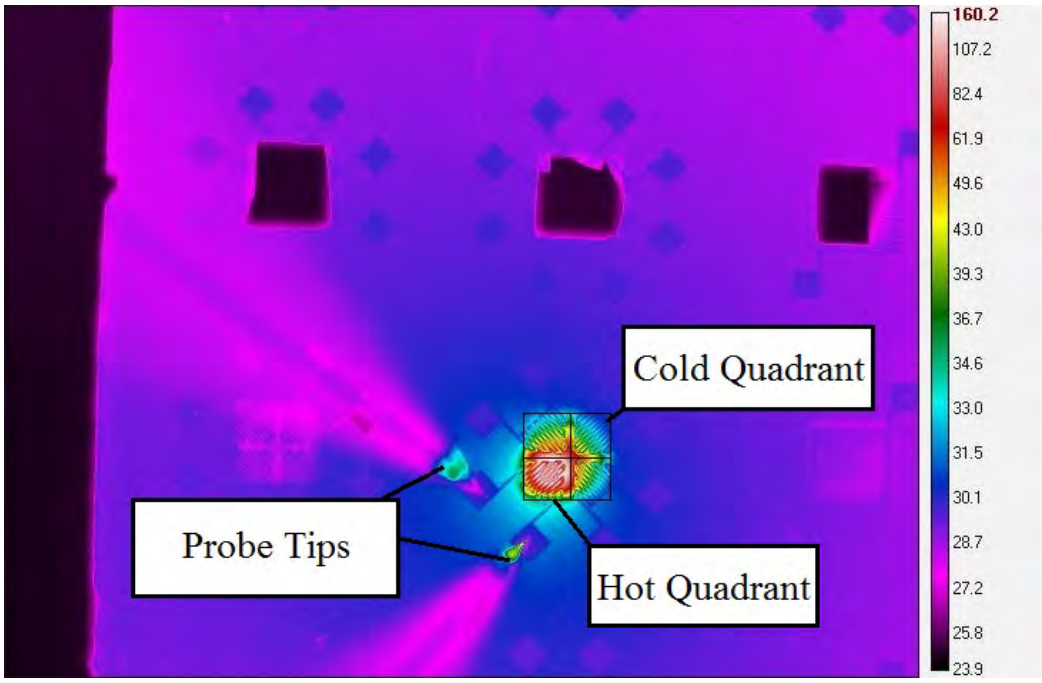

Figure 77. Thermal camera imaging of the multidirectional heater with 7 volts applied to the lower left heater.

The temperature was measured by taking an average of points within each quadrant. The average temperature in the "hot" quadrant ranged from 301.8K at zero volts applied to 434.2K at seven volts applied. The average temperature of the "cold" quadrant ranged from 301.8K at zero volts applied to 317K at seven volts applied. These temperatures are summarized in the table 20 and illustrated in Figure 78.

Table 20. Summary of applied voltage, current, power, and temperature for the hot and cold quadrants of the multidirectional actuator.

Voltage (V)	Current (mA)	Power (mW)	Hot Temp (K)	Colt Temp (K)
0	0	0	301.8	301.8
1	44	11	303.1	301.2
2	85	21	305.4	301.7
3	123	42	313.6	302.8
4	154	79	330.5	304.5
5	180	103	358.1	307.2
6	198	125	390.4	311.3
7	210	142	434.2	317.0

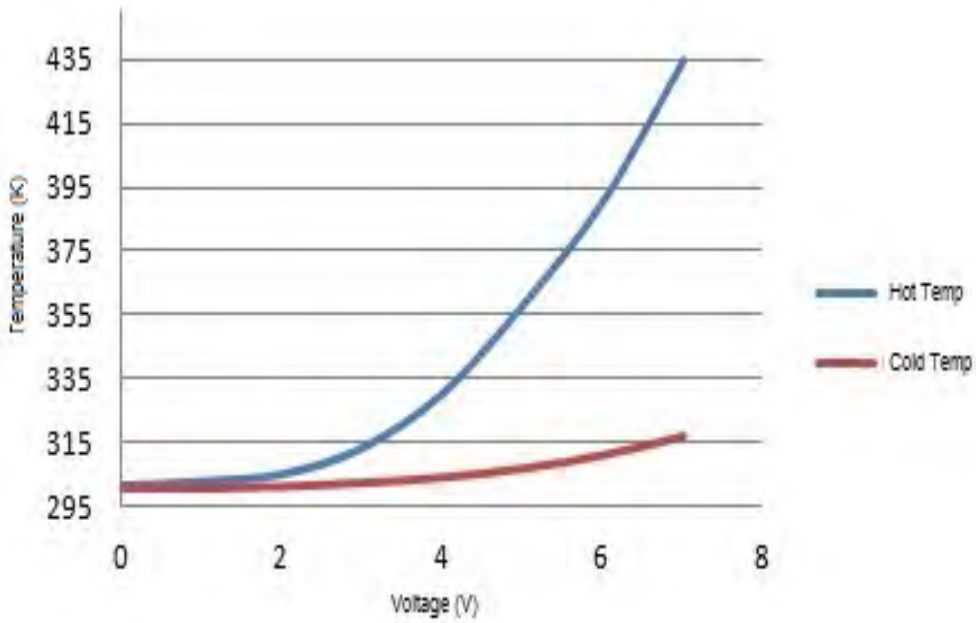

Figure 78. Plot of the average temperatures in each quadrant of the multidirectional membrane. The "hot" quadrant (blue) increases from 301K to 434K. The "cold" quadrant increases from 301K to 317K.

4.7.2 Actuation Results.

The localized deflection of the membrane quadrants was measured using the Zygo white light interferometer before the mirror assembly was bonded to it. The results, illustrated in Figures 79 and 80, show that a localized deflection occurs within the quadrant that is being heated. With seven volts applied, which corresponds to 434K,

peak deflection of approximately 13μm occurs 300μm from the center of the membrane.

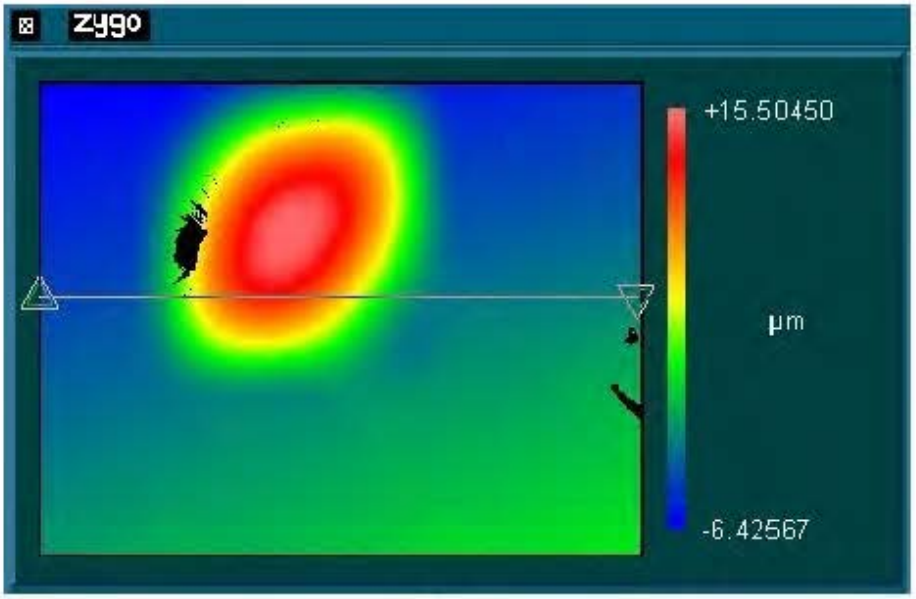

a

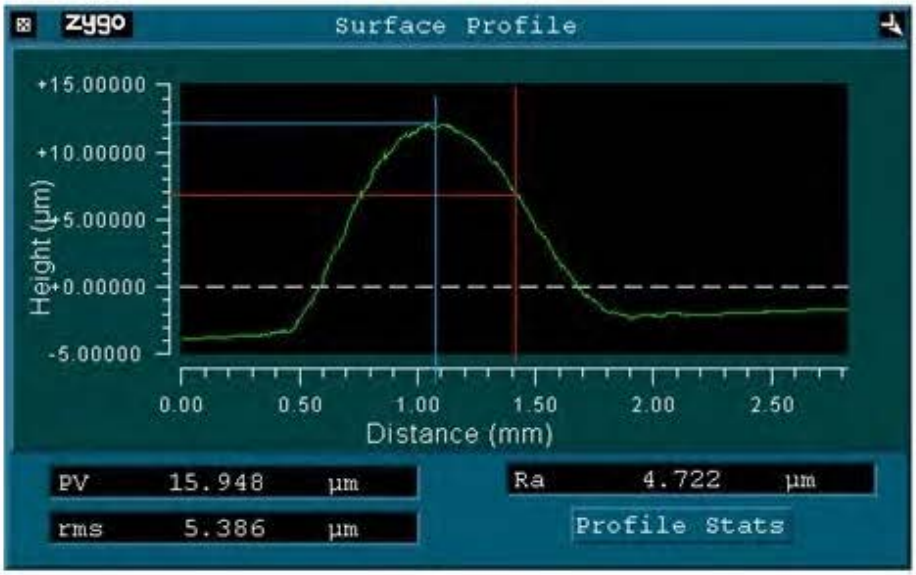

b

Figure 79. Screenshot of Zygo software measuring the deflection of the multidirectional thermal actuator with no voltage applied. A top view image of the membrane is shown in (a) while a plot of the surface profile of the membrane is shown in (b).

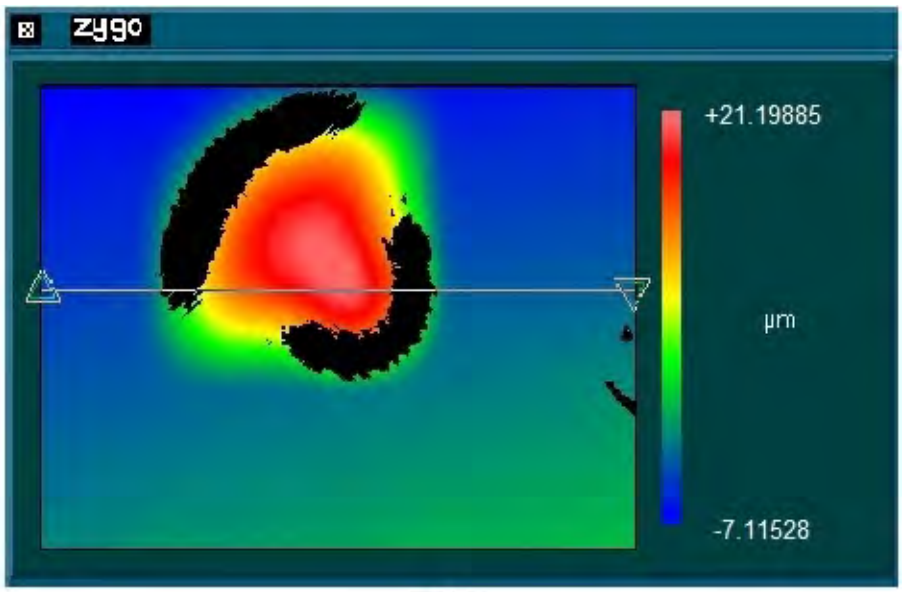

a

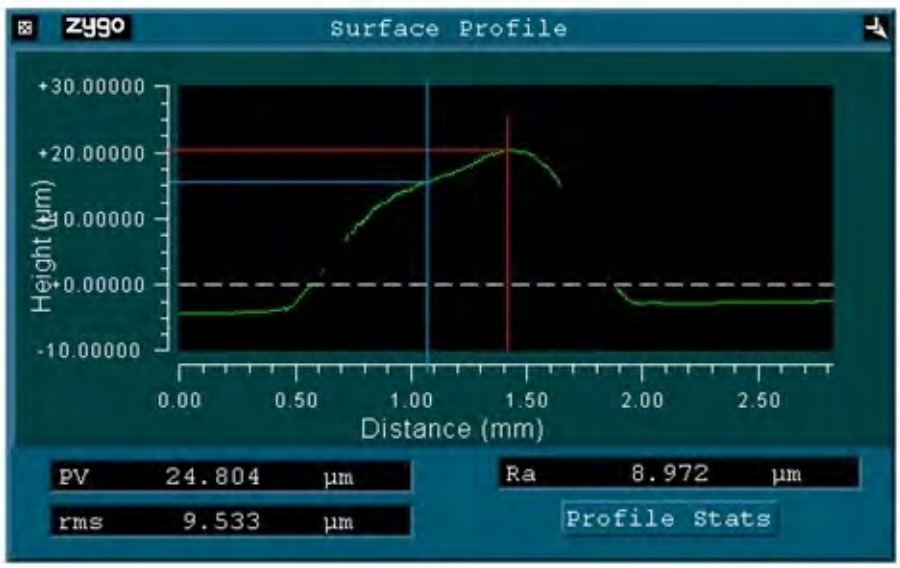

b

Figure 80. Screenshot of Zygo software measuring the deflection of the multidirectional thermal actuator with seven volts applied. A top view image of the membrane is shown in (a) while a plot of the surface profile of the membrane is shown in (b).

The actuation of the fully assembled mirror assembly was then measured using the Zygo. The four quadrants were arbitrarily named north, south, east, and west with respect to each other. Each quadrant was actuated from zero to six volts and

the tilt angle of the surface of the mirror was measured. The results are summarized in table 21.

Note that the mirror always tilts more to the north quadrant than to the south as well as more to the east quadrant than the west. Visual inspection of the assembly revealed that the mirror is slightly off centered to the north-east of the very center of the membrane. This can be explained because the single pillar that supports the mirror is off center, and skewed to one direction where the maximum deflection of the membrane occurs. When those quadrants are actuated, that side of the mirror experiences a higher deflection than it would in the opposite direction.

Table 21. Tilt angle vs. applied voltage

Voltage	North	South	East	West
0	0	0	0	0
1	0.06	0.03	0.03	0.02
2	0.14	0.1	0.09	0.05
3	0.24	0.19	0.19	0.14
4	0.37	0.34	0.33	0.26
5	0.57	0.51	0.48	0.44
6	0.80	0.71	0.75	0.67

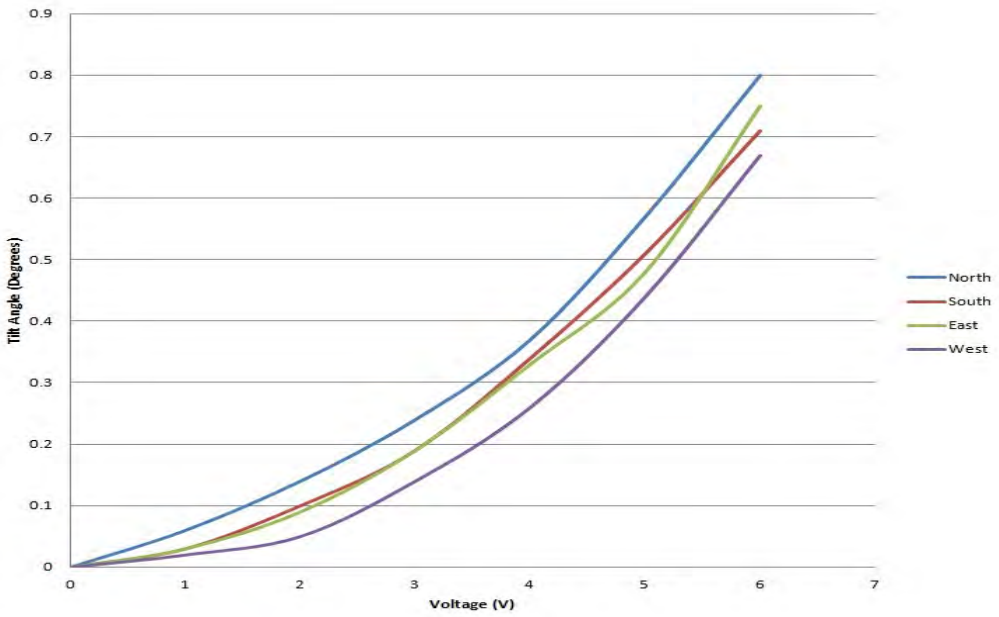

Figure 81. Plot of the multidirectional micromirror tilt angle vs. applied voltage.

4.8 Summary

This chapter provided the results of analytic and FEM modeling of the buckled membranes as well as measured data of the fabricated devices. These results demonstrate that the analytic analysis and FEM modeling are good predictors of the actual behavior of the fabricated membranes. The results of a detailed study on bonding methods were presented. Results of the a study into the use of SU-8 photoresist for bonding and packaging MEMS devices as well as integrating the buckled membranes into larger scale devices was presented. Additionally, it was shown that multidirectional actuation of the buckled membrane can be achieved through selectively heating specific regions of the membrane in order to generate a localized deflection in that specific region. The following chapter will provide detailed analysis of the results presented in this chapter.

V. Analysis

This section provides an analysis of the results presented in Chapter IV. Comparisons between the analytic modeling, FEM modeling, and measured results are presented first. Analysis of the buckled membranes response to applied temperature and applied pressure are is provided as well as analysis of the pressure sensitivity response of each different pressure sensor. Statistical analysis of the relationship between the degree of SU-8 cross linking and its bond strength is provided along with analysis of the etch resiliency results provided in the previous chapter. Finally, analysis of the results of the multidirectional actuator testing are discussed.

5.1 Modeling vs. Measured Data

A comparison of three data sources (Analytic modeling, FEM modeling, and measurement) for the membrane deflection vs. its size are shown in Figure 82 for a 1.0mm, 1.5mm, and 2.0mm membrane with a 5μm thick and Figure 83 for the 6μm thick membranes.

These figures show that both the analytic equations and the FEM modeling are good predictors of experimental data. The FEM model consistently overestimates the membrane deflection by approximately 12% for each size and thickness membrane. FEM simulation assumes a defect free material where in reality small structural defects present throughout the membrane may serve to limit it's deflection.

The analytic model also consistently overestimated the deflection of the membrane. This can be attributed to the same reasons that the FEM modeling overestimated. The analytic model does not take into account any defects in the material or any additional stiffness contributed by the electrothermal heaters fabricated on top of the membrane. The analytic modeling also does not take into account the mass effects

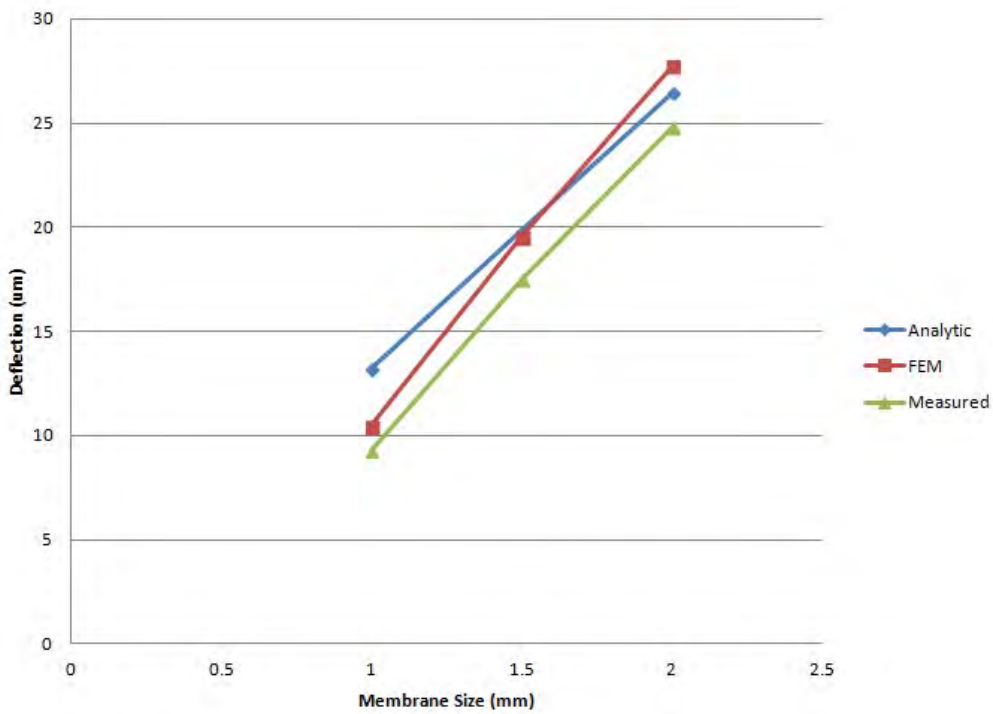

Figure 82. Plot of the analytic modeling (blue), FEM modeling (red), and measured deflections (green) for the 5μm thick, 1.0mm x 1.0mm, 1.5mm x 1.5mm, and 2.0 x 2.0mm membranes.

of the membrane. As the membrane size increases, so does its mass. As this mass increases, the membrane deflection decreases. This explains the decreasing variance of the analytic model as the membrane size increases. Table 22 provides a comparison between the results of the analytic modeling, FEM modeling, and measured results as well as the error of each type of modeling compared to the measured results.

The membranes tendency to increase in deflection as its size is increased makes sense from an analytic standpoint. Recall from equation 3 that the key factor in determining the membranes initial deflection is the critical stress σ_{cr} and that from equation 7 that the critical stress is dependent on membrane size, and thickness. Keeping the thickness constant, the critical stress then becomes solely dependent on varying membrane size. Combining both equations 7 and 3 we see that the deflection is directly proportional to the membrane size. Additionally, the decrease in deflection

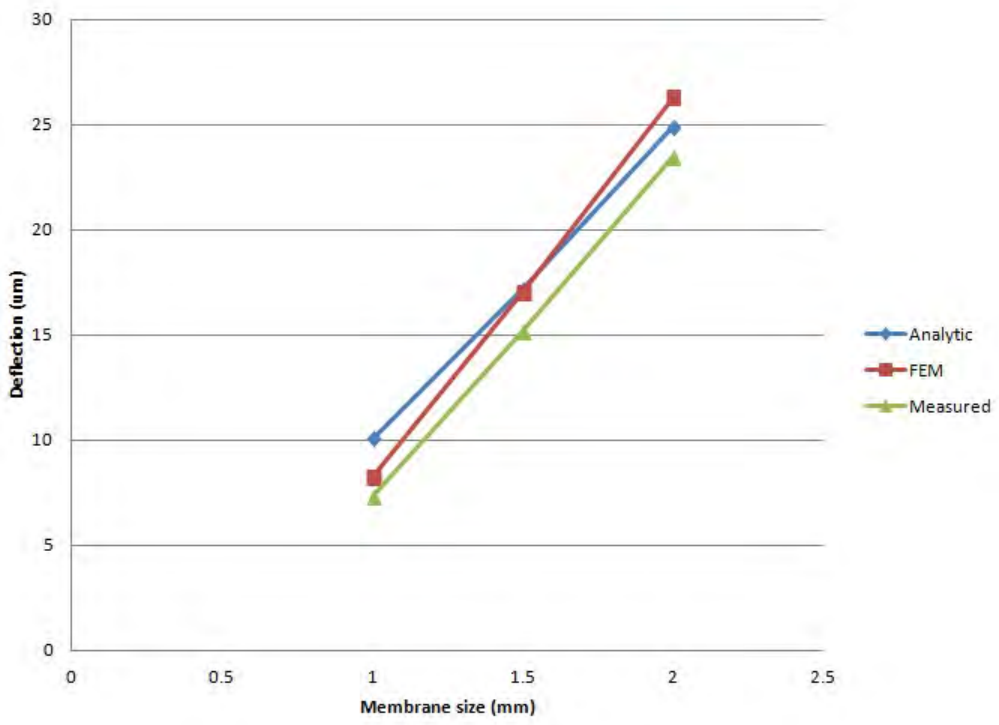

Figure 83. Plot of the analytic modeling (blue), FEM modeling (red), and measured deflections (green) for the 6μm thick, 1.0mm x 1.0mm, 1.5mm x 1.5mm, and 2.0 x 2.0mm membranes.

resulting from increasing thickness also makes sense from an analytic standpoint. When keeping the membrane size constant, it can be seen that the deflection of the membrane is inversely proportional to the flexural rigidity (D) of the membrane, which increases with thickness.

5.1.1 Deflection vs. Pressure.

Membrane pressure vs. deflection results indicated that smaller the membrame, the less it deflects for a given pressure increase. Table 23 summarizes the change in deflection of each membrane across an applied pressure range of 10 psi. For example, a 5μm thick, 1.0mm x 1.0mm membrane will deflect 6.57μm from its initial position when 10psi is applied to it.

Table 22. Table of membrane deflection results for analytic modeling, FEM modeling, and measured data.

Membrane Thickness (μm)	5			6		
Membrane Size (mm)	1.0	1.5	2.0	1.0	1.5	2.0
Measured (μm)	9.30	17.50	24.80	7.36	15.20	23.48
FEM (μm)	10.46	19.60	27.78	8.24	17.03	26.29
FEM Error (%)	12.4	12.0	12.0	11.9	12.0	11.9
Analytic (μm)	13.24	19.87	26.49	10.09	12.20	24.90
Analytic Error (%)	42.3	13.5	6.8	37.1	13.1	6.04

Table 23. Deflection ranges between 0 psi and 10 psi for all membranes.

	5μm	6μm
1.0mm	6.57	5.66
1.5mm	10.73	7.78
2.0mm	14.33	13.56

Looking down the columns of table 23 and comparing the different sized membranes of the same thickness, we see that as the size of the membrane increases, so does its deflection over a given pressure range. This is attributed to two factors. First, as the membranes increase in size, their overall stiffness decreases, making them less resistant to an applied force. Secondly, as the membranes increase in size, the same amount of pressure on a larger surface area results in a greater applied force to the membrane causing it to deflect further.

Looking across the rows of table 23 and comparing the same sized membranes of different thicknesses, we see that the 6μm thick membranes deflect less than the 5μm membranes of the same size. This can be directly attributed to the flexural rigidity of the membranes. Looking back at equations 8-11 we see that as the thickness of the membrane is increased, so is its flexural rigidity. This greater flexural rigidity results in thicker membranes having a "flatter" response than a thinner membrane would to the same applied pressure.

5.1.2 Deflection vs. Temperature.

Membrane temperature vs. deflection results indicated that smaller the membrane, the less it deflects for a given temperature increase. Table 24 summarizes the change in deflection of each membrane over a given temperature range.

Table 24. Deflection ranges over applied temperature range for each different membrane.

	5μm	6μm
1.0mm	8.568	4.896
1.5mm	12.857	5.735
2.0mm	15.768	9.040

Looking down the columns of table 24 and comparing the different sized membranes of the same thickness, we see that as the size of the membrane increases, so does its deflection over a given temperature range. Referring back to equation 7 we see that the critical stress of the membrane decreases as its size increases. According to equation 3, as the critical stress decreases with respect to the applied stress, deflection will increase. In other words, a membrane with a lower critical stress will deflect more than a membrane with a higher critical stress for the same applied temperature. The relation between the membrane size and its deflection for the same applied temperatures is summarized in table 25.

Table 25. Summary of the relation between membrane size and deflection for the same applied temperature.

Membrane Size	Critical Stress	Deflection
$\uparrow$	$\downarrow$	$\uparrow$
$\downarrow$	$\uparrow$	$\downarrow$

Looking across the rows of table 24 we see that as the thickness increases, the deflection range decreases. Again referring to equation 7 we see that the critical stress of the membrane increases as the flexural rigidity of the membrane increases. The membrane deflection will be smaller for a greater critical stress critical stress

at same applied temperature. The relation between the membrane thickness and its deflection for the same applied temperatures is summarized in table 25.

Table 26. Summary of the relation between membrane thickness and deflection for the same applied temperature.

Membrane Thickness	Critical Stress	Deflection
$\uparrow$	$\uparrow$	$\downarrow$
$\downarrow$	$\downarrow$	$\uparrow$

5.1.3 Pressure Sensor Sensitivity.

Figure 84 is a plot of all the sensitivity for all six pressure sensors over the range of applied temperature and pressure. It can be seen here that two pressure sensors made from the 2.0mm by 2.0mm membranes have the greatest overall range of sensitivity while the pressure sensors made from 1.0mm by 1.0mm membranes have the least overall range of sensitivity. Additionally, the 6μm thick pressure sensors exhibit a "flatter" response to applied pressure than the 5μm thick pressure sensors do for the same applied temperature. For each size membrane, there is a cross-over point of the sensitivity response curves. This happens because as pointed out earlier, the thinner membranes will have a greater initial deflection, but since they have a wider sensitivity response than the flatter sensitivity response of their 6μm counterparts, they will eventually cross over.

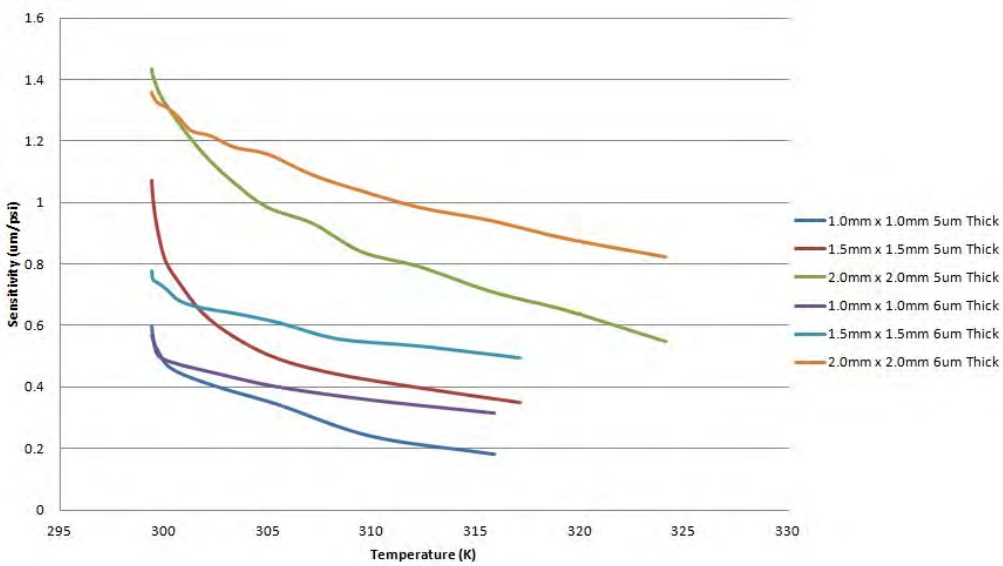

Figure 84. Plot of the pressure sensitivity vs. applied pressure 5μm and 6μm thick, 1.0mm, 1.5mm, and 2.0mm membranes. The 2.0mm pressure sensors exhibit the widest range of sensitivity, with the 5μm thick pressure sensor having the widest of all.

5.2 Bonding and Integration Analysis

The results of the seperation force testing performed on the bonded SU-8 samples was presented earlier in chapter IV. Further statistical analysis is required in order to make any valid inferences about this data. This analysis is presented here.

5.2.1 SU-8 Bonding Analysis.

Further examination of the residuals by plotting the semi-studentized residuals against the predictor variable of UV exposure time revealed a non-constancy of variance and a non-normal distribution illustrated by Figure 85. This megaphone shape of the residual plot indicates the error variance is larger for longer UV exposure doses.

$$F = -\frac{Y^{-0.2} - 1}{-0.29815} \tag{28}$$

In order to remedy the non-constant variance and non-normality, a Box-Cox transformation (Equation 28) was performed on the raw data where Y' is the transformed

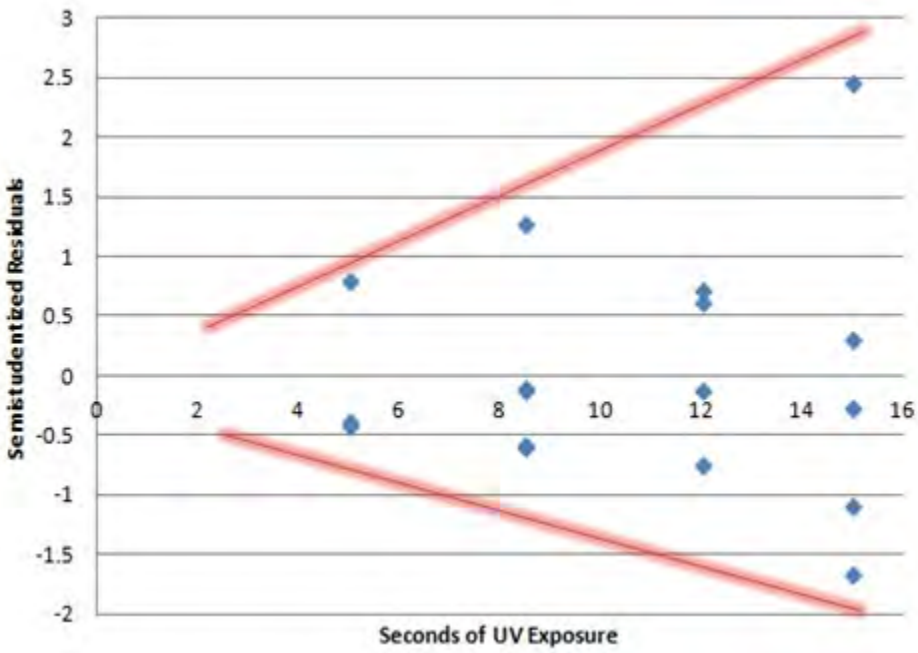

Figure 85. Plot of the semi-studentized residuals versus the predictor variable of UV exposure time indicate a non-constant error variance. The outlined "megaphone" shape indicates that the error variance increases as UV exposure times are increased.

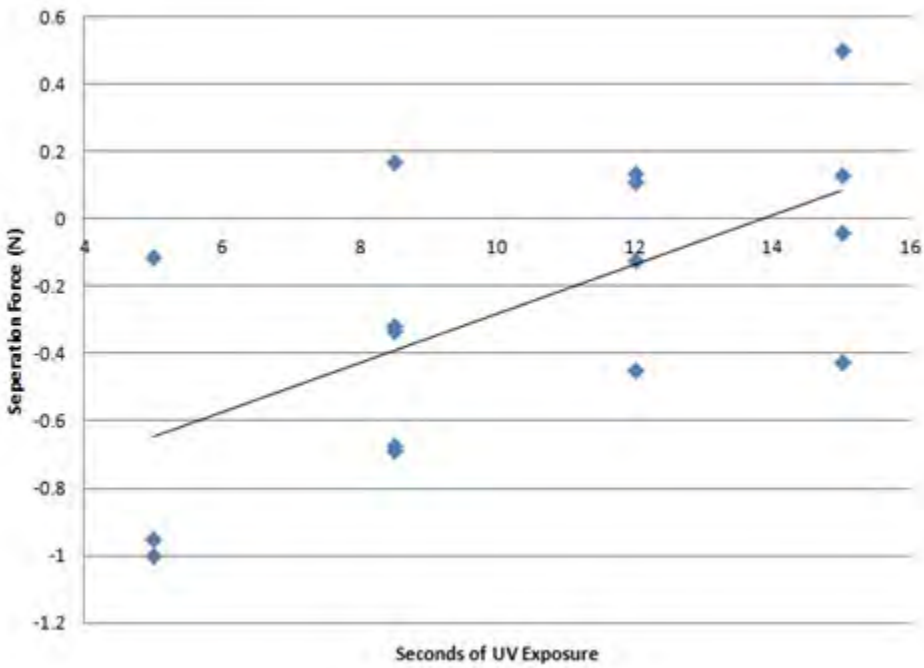

Figure 86. A predictor trend-line fitted to the transformed data of the separation testing was found to be non-zero with 95% confidence.

data for the separation force and Y is the original separation force. Equation 29 is the resulting trend-line for the transformed data.

$$Y = -1.0093 + 0.073X, \tag{29}$$

The new trend-line, shown in Figure 86, analyzed with a two-sided t-test, corroborated the initial analysis revealing an improved 95% confidence level that the raw data exhibited a non-zero slope. Additionally, the new R^2 value was 0.39 meaning that 39% of the variability of the separation force can be attributed to the UV exposure dose. Residual analysis for this new trend-line model shows a constancy of variance and normal distribution of residuals (Figure 87) indicating that the inferences made about this model are valid. Further analysis of the semi-studentized residuals of this transformed data revealed no statistical outliers in the raw data.

Additional analysis of the transformed data reveals that the residuals now fall on a normal distribution, further emphasizing that the inferences about the non-zero slope of the relation between the UV exposure time and separation force are valid. A Shapiro-Wilks test on these residuals also indicates that they are normally distributed.

The power of the test when the slope of the predictor trend-line of 0.073 is found to be approximately 96% meaning that if β_1 is 0.073 we are almost certain to conclude that there is a linear relation between UV exposure time and separation force.

Since the only variable examined in this experiment was UV exposure dosage, the remaining 60% cannot be definitively determined, however, we speculate that the remaining variability may be attributed to stochastic factors such as PEB temperature, film thickness, and data collection uncertainty. SU-8 robustness to etching, a necessary attribute for materials used in MEMS assembly and packaging, was investigated next.

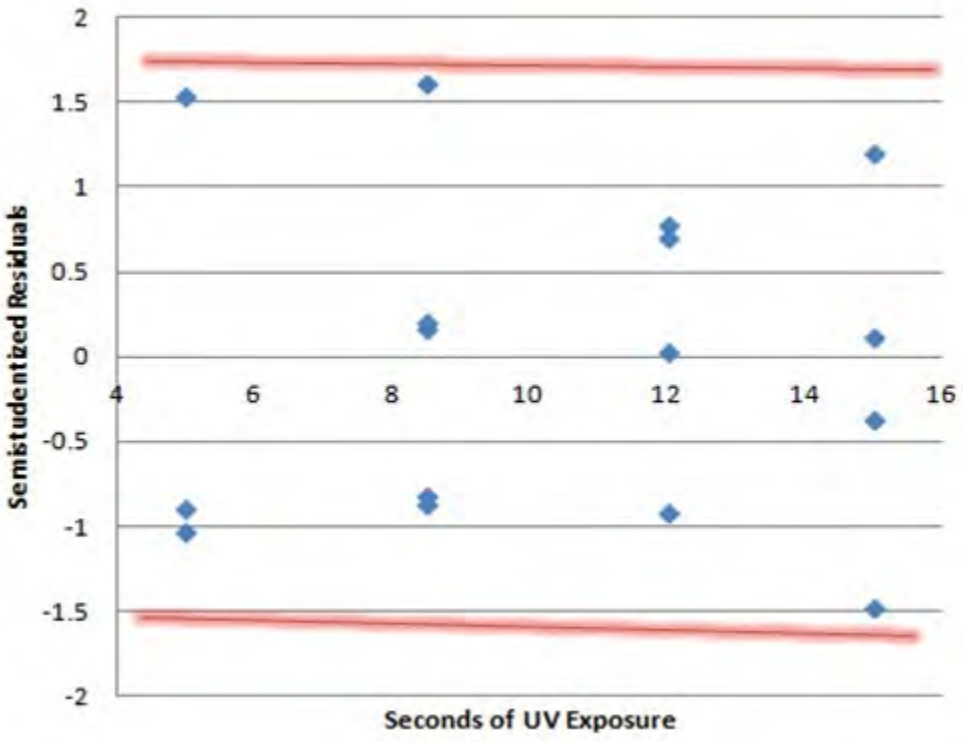

Figure 87. Plot of the semi-studentized residuals of the transformed data versus the predictor variable of UV exposure time show a constancy of variance indicating that inferences made about this data set are valid.

5.2.2 Etch Resiliency of Cross-linked SU-8.

Etch rates were determined by examining the difference between the initial and post-etch thicknesses. The overall negative slope of the data shows a lowered thickness delta indicating that increased levels of UV dosage (and higher degrees of cross-linking) resulted in higher SU-8 etch resiliency. Similar results were observed regardless of the post-exposure etch time. The 15 minute etch line, shown in Figure 89, reveals a 37 nm/min etch rate with 5 sec of UV exposure and 21 nm/min etch rate with a 15 sec exposure resulting in an improved etch resiliency of 43.2%. The 5 minute etch line revealed a 58.3% increase in etch resiliency with increased UV exposure.

Based on these initial results SU-8 appears to be an excellent material for flip-chip bonding and packaging MEMS and other microelectronic devices that will be

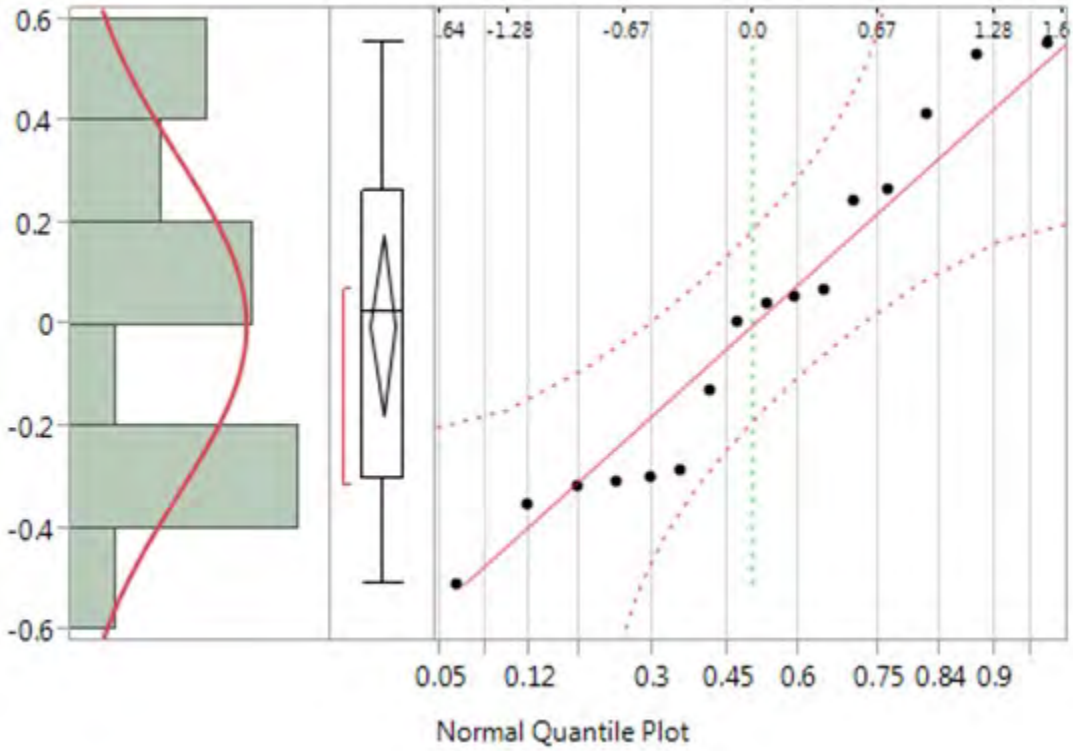

Figure 88. Distribution plot of the residuals of the transformed data. The close fit of data points to the line indicate a normalcy of distribution.

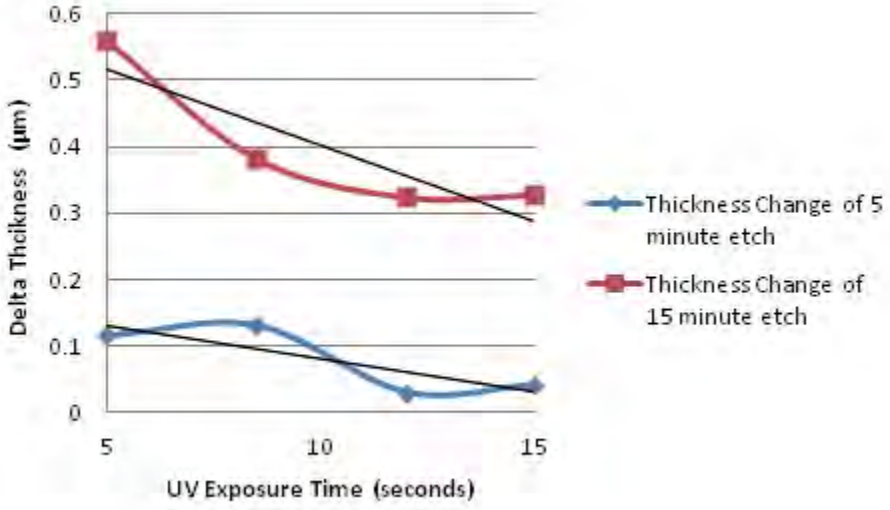

Figure 89. Plot of the thickness delta as it relates to UV exposure time. The negative slope of the trend-lines indicate that higher UV dosages decrease the etch rate of SU-8.

investigated in this research effort. However, this bonding method did not integrate well with the released membranes. While suitable for packaging of other MEMS structures that have the entire substrate to support them, the buckled membranes proved to be too fragile for the bonding pressures required for bonding with SU-8. After multiple attempts, the membrane would be destroyed each time.

5.3 Multidirectional actuator

The multidirectional heater, with one quadrant being heated demonstrated localized deflection 13μm higher than the membrane center which peaked 300μm from the membrane's center point. Based on these measurements, analysis predicts that the best tilt angle of a micromirror bonded to the membrane would be 2.48° with 7 volts applied to that quadrants heater as illustrated by Figure 90.

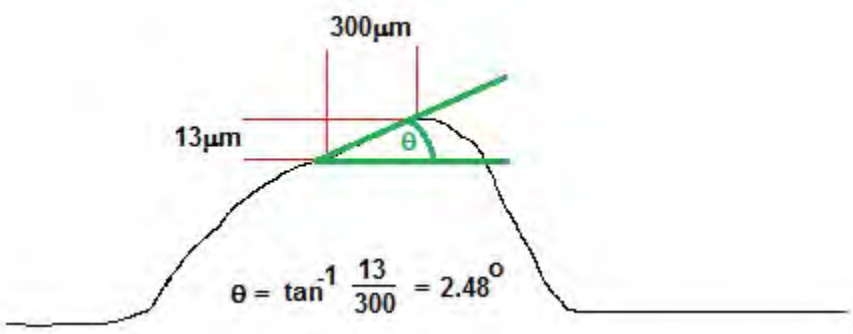

Figure 90. Figure illustrating the calculation of the expected tilt angle of the micromirror based on the measured profiled of the membrane under localized heating.

The actual measured tilt angle for 7 volts applied was an average of 0.73°. When the micromirror pillar is bonded to the center of the membrane, it deforms the shape of the membrane slightly causing the peak of the membrane to flatten out. This deformation is a new source of stress within the membrane which counteracts the stressed induced by the increase in temperature causing a smaller localized deflection.

5.4 Summary

This chapter provided an analysis of the results of analytic and FEM modeling of the buckled membranes as well as measured data of the fabricated devices. With this analysis, behavior of these membranes is related to and explained by the theory outlined in Chapter II. Additionally, the results of the SU-8 bonding studied were analyzed to show the statistically significant relationship between the degree of SU-8 cross linking and its bond strength and etch resiliency.

The following chapter will provide conclusions and recommendations such as possible future research as well as contributions generated by this research.

VI. Conclusions and Recommendations

This chapter will summarize this research effort. The individual accomplishments of this research will be stated and a brief description provided. Following this, recommendations of future work will be provided based on both observations of what could be improved with the current design, as well as new ideas within the realm of MEMS buckled membranes.

6.1 Contributions

Several contributions have been made as a direct result of this research effort. These contributions are listed as follows.

6.1.1 Tunable Pressure Sensor.

A tunable pressure sensor was designed, fabricated, and characterized. It was found that by electrothermally tuning and increasing the stiffness of a membrane, it's sensitivity to an applied pressure is decreased. This has applications to situations where there maybe be a "noisy" pressure environment such as on a test set up with a leaky valve, or a lab environment where there environmental pressure fluctuates. The ability to decrease the sensitivity of a pressure sensor will allow this pressure noise to be filtered out of any measurements [113, 114]

6.1.2 Volumetric Actuator.

A volumetric actuator was realized out of a MEMS buckled membrane. An variable volume cavity has applications in the field of microfluidics, specifically as a tunable microfluidics capacitor for use in microfluidics circuits. In typical microfluidic circits, the volume, and thus capacitance, of a cavity is a fixed value. The ability

to adjust this capacitance could be useful in resonant circuits or situations where the pressure must be maintained within a high degree of precision [115].

6.1.3 Multidirectional Thermal Actuator.

A multidirectional electrothermal actuator was designed, fabricated, and characterized. It was found that by heating a specific quadrant of a buckled membrane, localized heating results in a localized deflection of that quadrant of the membrane. This is useful in the area of electro-optics for beam steering applications.

6.1.4 MEMS Bonding and Packaging with SU-8.

The effects of SU-8 cross-linking was correlated to its bond-strength and etch resiliency was investigated and characterized. It was found that higher degrees of cross-linking resulting from increased UV exposure increased both the bond strength and etch resiliency of SU-8 when it is used as a bonding and packaging material. While the use of SU-8 for bonding ultimately was not applicable for assembling structures incorporating buckled membranes, this knowledge is ultimately useful for other MEMS packaging and assembly applications [116].

6.2 Future Work Recommendations

While this research characterized the performance of different sized buckled membranes and and successfully characterized three different devices which incorporated these membranes, there is still much room for future work and improvement.

6.2.1 Micromirror Actuator Optimization.

The devices demonstrated in this research effort were successful proofs-of-concept, but there is room for improvement in their design. A possible improvement to the

design of the multidirectional actuator would be mount the mirror using four smaller pillars oriented over the points of maximum deflection in each of the quadrants instead of the single 300μm by 300μm pillar situated in the center of the membrane as illustrated by Figure 91. This could potentially increase the degree of tilt of the design, resulting in a more useful device.

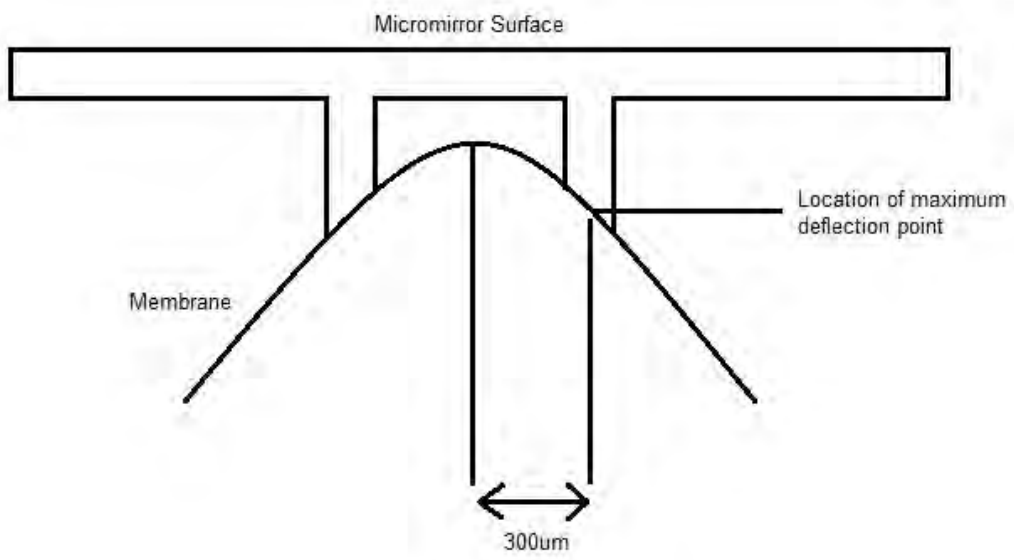

Figure 91. Diagram of a multipillar micromirror with pillars located over the points of maximum deflection of the multidirectional actuated membrane.

6.3 Summary

This chapter has provided a discussion of the overall results and contributions of this research effort. Additionally, recommendations for future research and applications were made. The following appendices provide more detailed information pertinent to this research such as the fabrication processes, photolithographic mask layouts, and data tables of collected measurements results.

Appendix A.

A-1 Heater Fabrication Process Follower

Init.	Process Step	Notes	Date Time
	INSPECT SAMPLE o Note any defects	**Start Date** **Start Time**	
	SETUP o Start MJB3 to step 4 wait till suss power shows 275W o Start DUV system, needs 10 min to warm up.		
	SOLVENT CLEAN o 20 sec acetone rinse o 20 sec methanol rinse o 20 sec isopropyl rinse o Dry with nitrogen at 500 rpm o Dry wafer with nitrogen on clean texwipes o 1 min 65°C hot plate bake o 1 min 95°C hot plate bake		
	APPLY SF11 o Dropper SF11 over sample o Ensure sample is completely covered to the edges o 4 sec 500 rpm o 30 sec 4000 rpm o 3 min 110°C hot plate bake		
	APPLY 1818 o Dropper 1818 over sample o Ensure sample is completely covered to the edges o 4 sec 500 rpm o 30 sec 4000 rpm o 3 min 110°C hot plate bake		
	EXPOSE 1818 o Finish setting up MJB3 o Clean Mask (ensure cap is on the spinner) o Put mask on the holder o Carefully raise stage to see height, adjust appropriately o Center sample within one inch window for alignment. Use the resistor mask. o 8 sec expose, may need longer depends on thickness. SU-8 manual lists the amount of energy necessary to fully expose.		
	DEVELOP o 45 sec spin at 500 rpm, spray with 351 (5/1 351/DI) developer. o 30 sec spin at 500 rpm and spray DI H_2O. o Rinse sample and dry with nitrogen.		
	EXPOSE SF11 o 200 sec flood expose, may need longer depends on thickness.		
	DEVELOP o Partially fill small container with SAL 101 developer. (enough to cover sample). o Submerge sample in developer for 1 minute. Slight agitation. o Rinse sample and dry with nitrogen.		
	EVAPORATE TI/AU o Need 500A of Ti and 3000A of Au deposited on top side of sample. o Follow backside etch process after evaporation and before release.		
	RELEASE o Fill beaker with ¼ inch of 1165 stripping agent. o 120°C heat on hot plate until liquid reaches 90°C, cover with foil. o 20 min sample soak in acetone. Slight agitation ok. NO ULTRASONIC, samples will break o Submerge sample in developer for 10 minutes. Slight agitation. o Rinse sample and dry with nitrogen.		
	Inspect resistors turned out as expected.	**Finish Date** **Finish Time**	

Figure A-1. Process follower for heater fabrication

A-2 Membrane Fabrication Process Follower

Init.	Process Step	Notes	Date Time
	INSPECT SAMPLE o Note any defects	**Start Date** **Start Time**	
	SETUP o Start MJB3 to step 4 wait till suss power shows 275W		
	SOLVENT CLEAN o 20 sec acetone rinse o 20 sec methanol rinse o 20 sec isopropyl rinse o Dry with nitrogen at 500 rpm o Dry wafer with nitrogen on clean texwipes o 1 min 65°C hot plate bake o 1 min 95°C hot plate bake		
	Apply SU8 o Dropper SU8 over sample (do not let dropper touch edge of bottle) o Ensure sample is completely covered to the edges o 4 sec 500 rpm o 30 sec 2800 rpm gives 17microns approx (2000 rpm as backup) o Clean back of sample with acetone on a swab after sample finishes spinning o 3 min 65°C hot plate bake o 7 min 65°C hot plate bake o Inspect		
	Expose o Finish setting up MJB3 o Clean Mask (ensure cap is on the spinner) o Put mask on the holder o Carefully raise stage to see height, adjust appropriately o 23 sec expose, may need longer depends on thickness. SU-8 manual lists the amount of energy necessary to fully expose. o 1 min 65°C hot plate bake o 3 min 95°C hot plate bake		
	Develop o Partially fill small container with SU-8 developer. (enough to cover sample). o Submerge sample in developer for 4 minutes. Slight agitation. o Rinse sample and dry with nitrogen.		
	Develop o 3 min 65°C hot plate bake o 30 min 110°C hot plate bake		
	Inspect finished etch holes under optical microscope.	**Finish Date** **Finish Time**	

Figure A-2. Process follower for membrane fabrication

A-3 Mask Fabrication Process Follower

	Load Design ☐Load selected mask design onto Heidelberg Software ☐Verify design is correct in Layout Editor ☐Set mask writer to 8mW power with a 90% duty cycle ☐Load a mask blank (photoresist side up) ☐Turn on vacuum chuck ☐Run the program		
	Develop ☐Once program is complete, remove the mask ☐Shut down Heidelberg software if no more masks to be written ☐Submerge mask in developer solution (3:1 DI Water:351 Developer) with agitation for 30 seconds ☐Rince with DI water for 30 seconds ☐Inspect for full development under microscope		
	Chrome Etch ☐Submerge mask in CR44 chrome etchant for 80 seconds with agitation ☐Rinse with DI water for 30 seconds ☐Inspect for etch completeness under microscope		
	Resist Removal ☐30 sec acetone rinse ☐30 sec methanol rinse ☐30 sec isopropyl rinse ☐Dry with nitrogen at 500 rpm ☐Dry wafer with nitrogen on clean texwipes☐ ☐Plasma ash mask for 5 minutes at 75W to remove any remaining photoresist		
		Finish Date **Finish Time**	

Figure A-3. Process follower for photomask fabrication

Appendix B.

B-1 1.0mm, 1.5mm, and 2.0mm Heater Mask

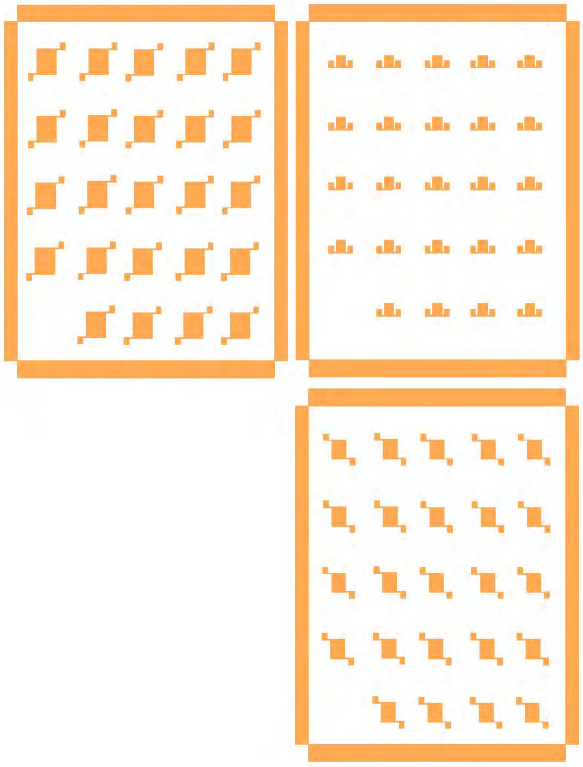

Figure B-1. Mask pattern for fabrication of 1.0mm, 1.5mm, and 2.0mm Heaters

B-2 1.0mm, 1.5mm, and 2.0mm Membrane Mask

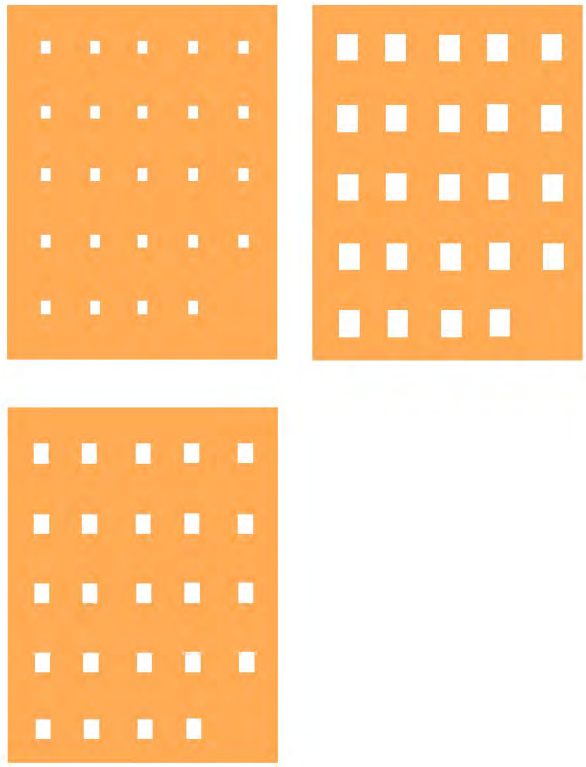

Figure B-2. Mask pattern for fabrication of 1.0mm, 1.5mm, and 2.0mm Membranes

B-3 Multidirectional Heater Mask

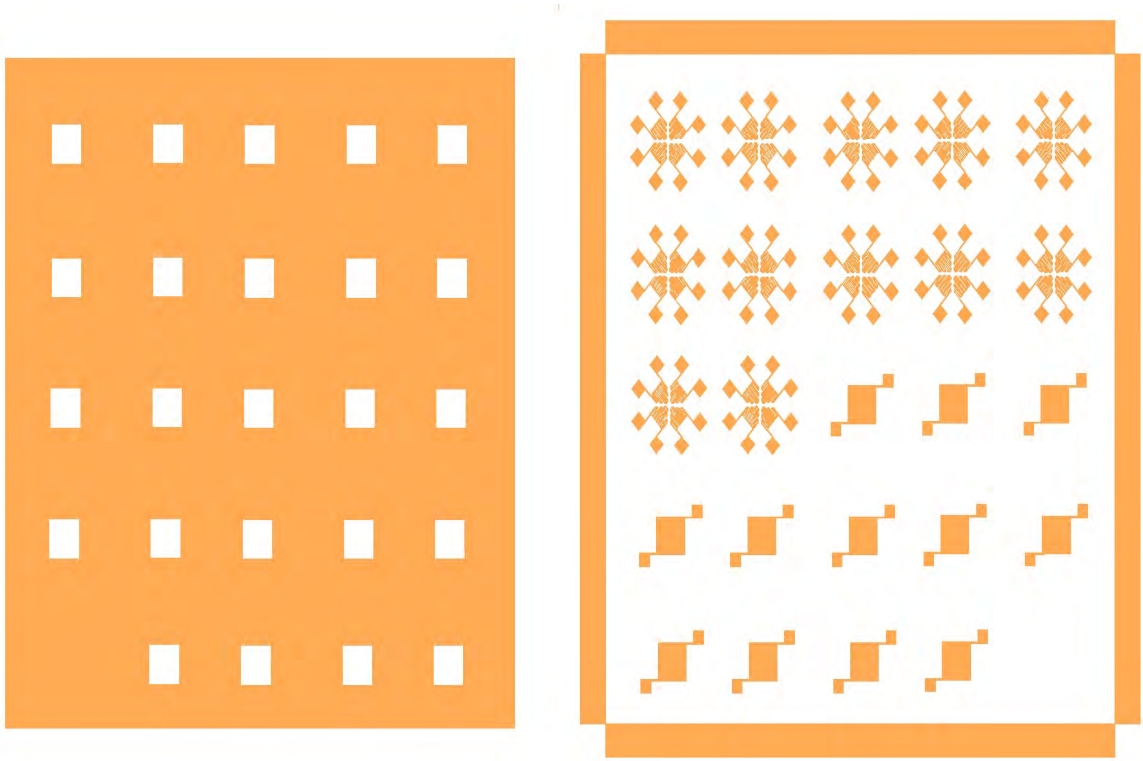

Figure B-3. Mask pattern for fabrication of multidirectional heaters and membranes.

B-4 Spacer Assembly Method Mask

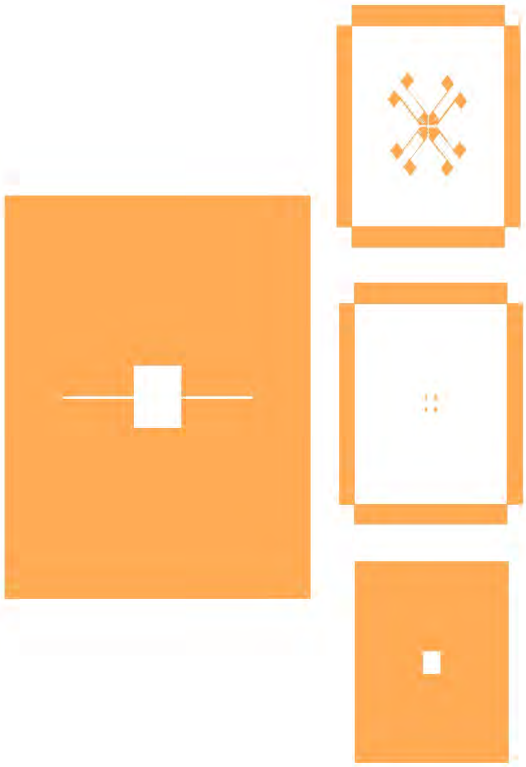

Figure B-4. Mask pattern for spacer assembly.

B-5 Pillar Mask

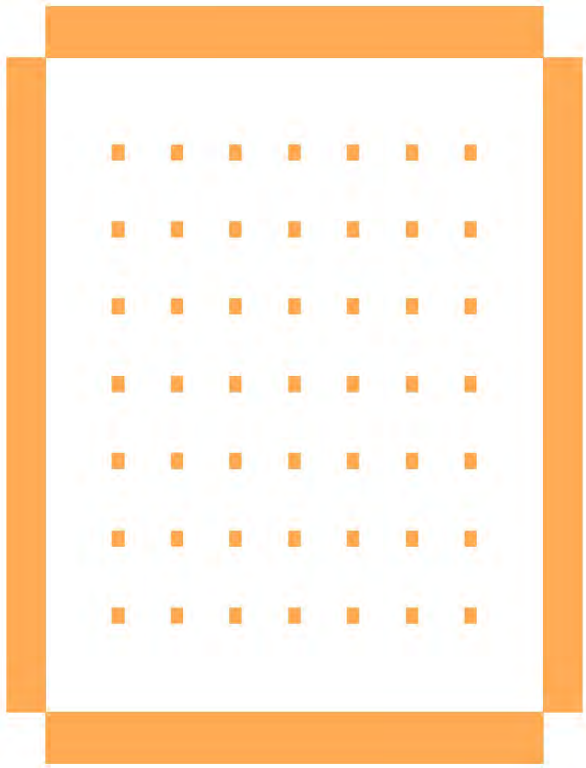

Figure B-5. Mask pattern for the fabrication of 300μm pillars.

Appendix C.

C-1 Solvent Hood

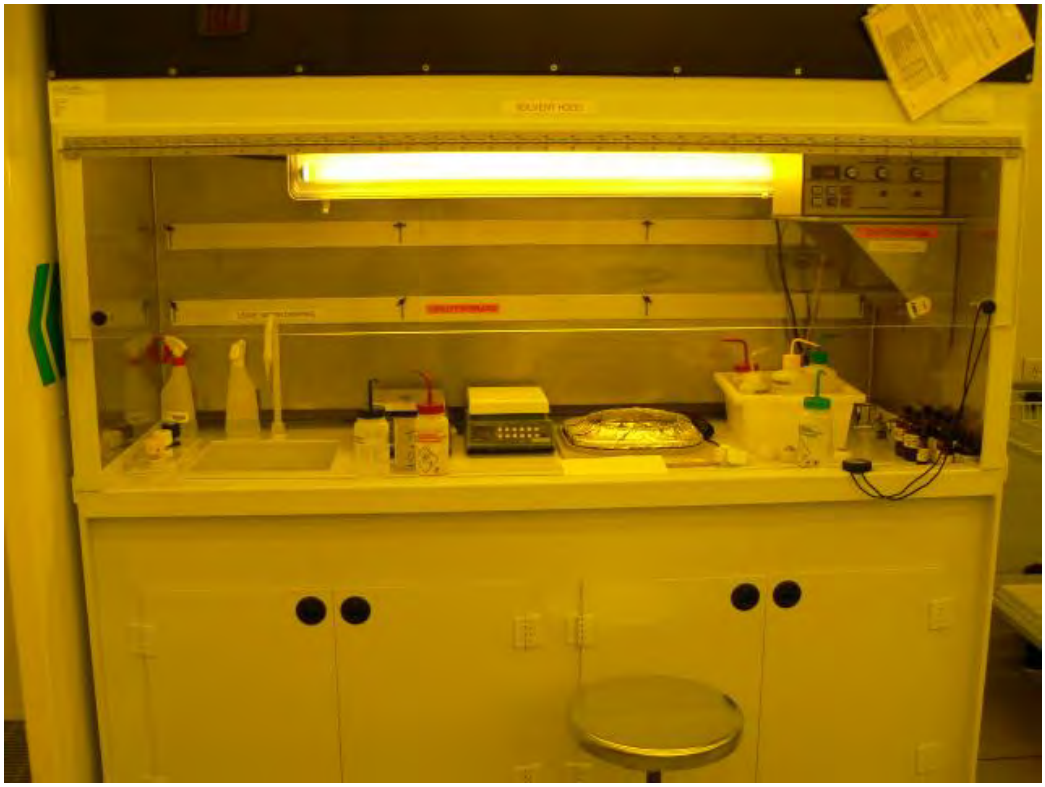

Figure C-1. Solvent hood used for photolithography steps and any use of solvents for cleaning.

C-2 Heidelberg μPG 101 Mask Writer

Figure C-2. Heidelberg μPG 101 direct write mask writer used for making 4" photomasks used during photolithography.

C-3 Karl Suss MJB-3 Mask Aligner

Figure C-3. MJB-3 mask aligner used for exposing photoresist during the lithographic process. Exposure time is variable depending on the type and thickness of photoresist being exposed.

C-4 STS Pegasus Deep Reactive Ion Etcher

Figure C-4. STS Pegasus deep reactive ion etcher at the University of Michigan, Lurie Nanofabrication Facility.

C-5 Anatech USA SP-100 Plasma Asher

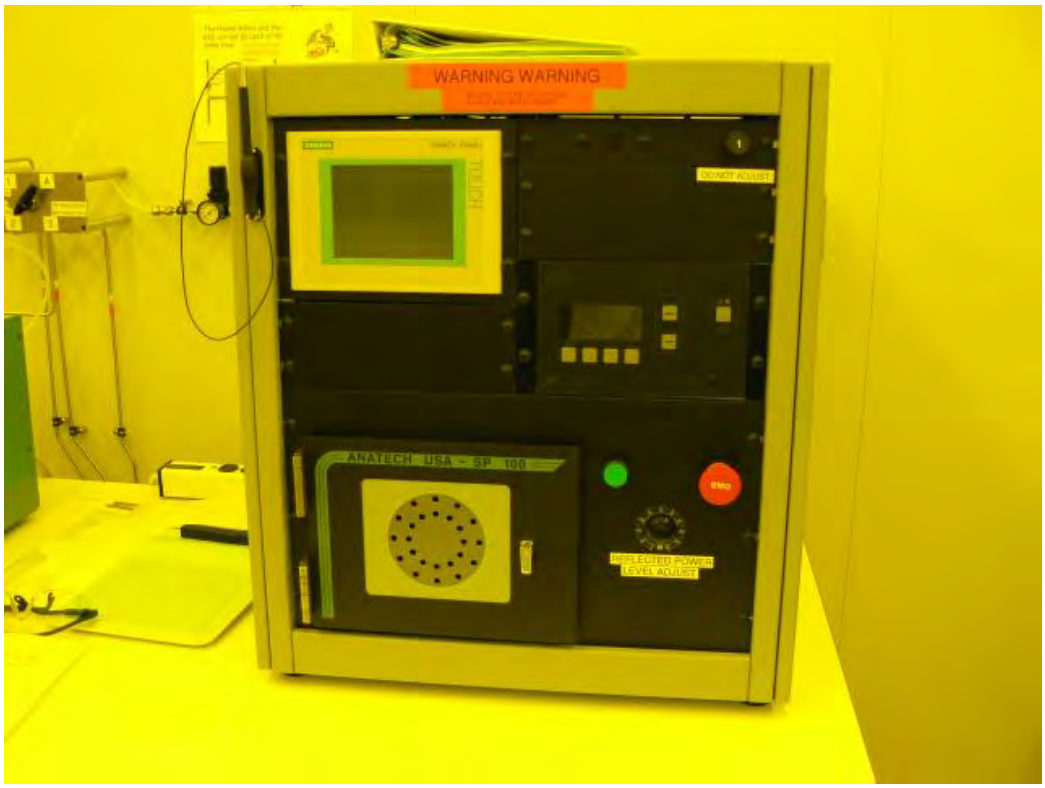

Figure C-5. This tool is used to clean samples to prepare them for subsequent steps such as photolithography or metal evaporation.

C-6 Semiconductor Equipment Corp. 860 Eagle Bonder

Figure C-6. This tool is used for flip bonding two samples together. It is capable of providing precise alignment, variable bond pressure, and variable temperature.

C-7 Quanta 3D 200i Scanning Electron Microscope

Figure C-7. Quanta 3D 200i scanning electron microscope used to provide SEM images of devices.

Appendix D.

D-1 Visual Bibliography

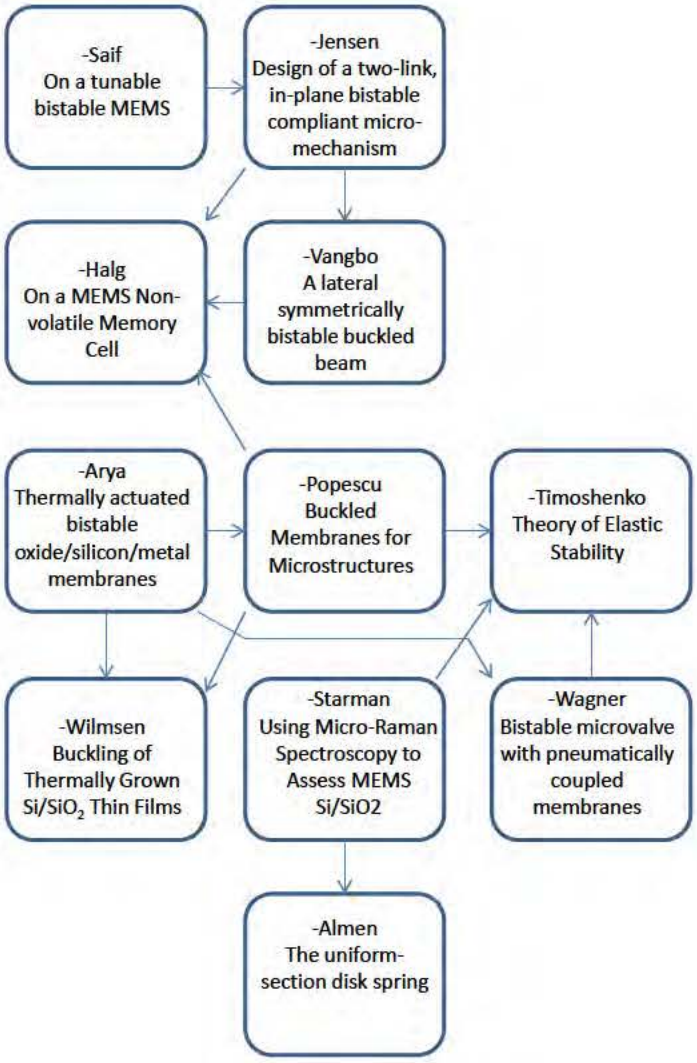

Figure D-1. Visual Bibliography.

Appendix E.

E-1 Mass-Deflection Study

An experiment was performed to study the ability of the membrane to serve as an actuator. A silicon mass was fabricated out of five silicon chips (2.0mm long by 2.0mm wide by 1.0mm thick) bonded together with SU-8. Given the density of silicon (2.33g/cm^3) this creates a mass of 0.0093g which would result in a force of 91.34μN.

The total height of the mass was measured at 500.08μm using the Zygo. The mass was then bonded to the top of the 1.5mm by 1.5mm square membrane. Having a measured stiffness of approximately 500μN/μm, this is expected to cause the membrane to deflect downward by 0.18μm. This deflection was to be determined by measuring the height of the top of the mass with respect to the substrate, and subtracting the known height of the mass. This would give the height of the membrane. By comparing that amount to the non-weighted deflection of the membrane, the amount of deflection due to the mass could be determined. Unfortunately, with the Zygo configured to measure from the top of a 5mm tall mass, a deflection of .18μm is within the noise floor, and not possible to get a reliable measurement. Future study of the effect of mass on these membranes would require the use of either more sensitive equipment.

One important takeaway from this experiment is the validation of the scaling laws and how they relate to mass in MEMS devices. In the macro world, mass is an important factor for consideration, however, when scaled down to the MEMS level, mass becomes far less significant of a factor to consider.

Bibliography

1. C. Liu, *Foundations of MEMS*. Pearson Hall, 2006.

2. G. Kovacs, *Micromachined Transducers Sourcebook*. McGraw Hill, 1998.

3. R. C. Johnson, "MEMS breed a new batch of consumer pleasing devices," *EE Times*, November 2007.

4. Microposit S1800 series photoresits. [Online]. Available: www.microchem.com

5. G. May and S. Sze, *Fundamentals of Semiconductor Fabrication*. John Wiley and Sons, 2004.

6. Georgia Tech, department of electrical and computer engineering. [Online]. Available: www.ece.gatech.edu

7. SU-8 2000 permanent epoxy photoresist processing guidelines. [Online]. Available: www.microchem.com

8. S. Ostrow II and R. A. Coutu Jr., "Novel microelectromechanicalsystems image reversal fabrication process based on robust su-8 masking layers," *Journal of Micro/Nanolithography, MEMS, and MOEMS (JM3)*, 2011.

9. H. Lorenz, M. Despont, N. Fahrni, N. LaBianca, P. Renaud, and P. Vettiger, "Su-8: A low-cost negative resist for MEMS," *J. Micromech. Microeng*, 1997.

10. M. J. Madou, *Fundamentals of Microfabrication*, 2nd ed. CRC Press, 2002.

11. J. M. Bustillo, R. T. How, and R. S. Muller, "Surface micromachining of microelectromechanical systems," in *Proc. of the IEEE*, vol. 86, no. 8, August 1998.

12. J. Carter *et al.*, *PolyMUMPS Design Handbook*, 11th ed., MEMSCAP Inc., 1992-2005.

13. *SUMMiT V: Five Level Surface Micromachining Technology Design Manual*, 3rd ed., Sandia National Laboratories, October 2012.

14. T. Hsu, *MEMS and Microsystems Design and Manufacture*. McGraw Hill, 2002.

15. G. Kovacs, N. Maluf, and K. Petersen, "Bulk micromachining of silicon," in *Proc. of the IEEE*, vol. 86, no. 8, August 1998.

16. W. Ehrfeld, "Fabrication of microstructures using the liga process," in *Proc. IEEE Micro Robots and Teleoperators Workshop*.

17. . (2015) Memsnet fabrication. [Online]. Available: https://www.memsnet.org/mems/fabrication.html

18. Step by step LIGA process. [Online]. Available: www.lafayette.edu/es101-06-fa14/files/2014/12/LIGA-steps-1024x565.png

19. SOI for MEMS: A promising material. [Online]. Available: http://www.advancedsubstratenews.com/2011/03/soi-for-mems-a-promising-material/

20. M. Gad-el-Hak, *The MEMS Handbook*. CRC Press, 2002.

21. M. S. Rahman, M. M. Chitteboyna, D. P. Butler, Z. Celik-Butler, and S. P. Pacheco, "Device level vacuum packaging for RF mems," *J. Microelectromech. Syst.*, 2010.

22. Y. T. Chng, L. Lin, and K. Najafi, "Localized silicon fusion and eutectic bonding for MEMS fabrication and packaging," *J. Microelectromech. Syst.*, 2000.

23. B. Lee, S. Seok, and K. Chun, "A study on wafer level vacuum packaging for MEMS devices," *J. Micromech. Microeng.*, 2003.

24. J. Mitchel, G. R. Lahiji, and K. Najafi, "Encapsulation of vacuum sensors in a wafer level package using a gold-silicon eutectic bonding," in *Proc. Transducers*.

25. J. Mitchel, G. R. Lahiji, and K. Najafi, "An improved performance Poly-Si pirani vacuum gauge using heat distribution structural supports," *J. Microelectromech. Syst.*, 2008.

26. D. Sparks, S. Massoud-Ansariand, and K. Najafi, "Long term evaluation of hermetically glass frit sealed silicon to pyrex wafers with feedthroughs," *J. Micromech. Microeng.*, 2000.

27. H. Kim and K. Najafi, "Characterization of low-temperature wafer bonding using thin-film parylene," *J. Microelectromech. Syst.*, 2005.

28. L. Lin, "MEMS post-packaging by localized heating and bonding," *IEEE Trans. On Advanced Packaging*, 2000.

29. C. Wang, A. Brown, and I. DeWolf, "Low temperature polymer bonding processes for MEMS encapsulation," Heriot Watt University, Tech. Rep., 2007.

30. C. T. Pan, H. Yang, S. C. Shen, M. C. Chou, and H. P. Chou, "A low-temperature wafer bonding technique using patternable materials," *J. Micromech. Microeng.*, 2002.

31. E. Ochoa, L. Starman, and R. A. Coutu Jr., "Flip bonding with su-8 for hybrid $Al_xGa_{1-x}As$-polysilicon MEMS tunable filter," *J. Micro./Nanolith. MEMS/-MOEMS*, 2007.

32. N. Glauvitz, L. Starman, and R. A. Coutu Jr., "Effects of SU-8 cross-linking on flip-chip bond strength when assembling and packaging mems," in *Proc. Eurosensors XXV*.

33. R. Jaeger, *Introduction to Microelectronic Fabrication*, 2nd ed. Prentice Hall, 2002.

34. . (2015) Reactive ion etching. [Online]. Available: http://www.cleanroom.byu.edu/rie_etching.phtml

35. Si DRIE for through-wafer via fabrication. [Online]. Available: www.electroiq.com/blog/2006/03/si-dire-for-through-wafer-via-fabrication

36. M. Puech *et al.*, "Achievements and perspectives of the DRIE technology for the microsystems market," in *Proc. 14th International Conference on Solid-State Sensors, Actuators, and Microsystems*, Lynon France, June 2007.

37. Find MEMS. [Online]. Available: http://www.findmems.com

38. K. Millar, M. Li, K. Walsh, and X. Fu, "The effects of DRIE operational parameters on vertically aligned micropillar arrays," *Journal of Micromaching and Microengineering*, vol. 23, no. , 2013.

39. G. Kaltas, A. Nassiopoulou, M. Siakavellas, and E. Anastassakis, "Stress effect on suspended polycrystalline silicon membranes fabricated by micromachining of porous silicon," *Sensors and Actuators*, vol. 68, no. 1-3, 1998.

40. J. Laconte, D. Flandre, and J. Raskin, *Micromachined Thin-Film Sensors for SOI-CMOS Co-Integration*. Springer, 2006.

41. T. Iida, T. Itoh, D. Noguchi, and Y. Takano, "Residual lattice strain in the silicon-on-insulator bonded wafers: Termal behavior and formation mechanisms," *Journal of Applied Physics*, vol. 87, no. 2, January 2000.

42. M. F. Doerner and W. D. Nix, "Stresses and deformation processes in thin films on substrates," *Critical Reviews in Solid State and Materials Science*, vol. 14, no. 3, 1998.

43. I. De Wolf, "Micro-raman spectroscopy to study local mechanical stress in silicon integrated circuits," *Semiconductor Science and Technology*, vol. 11, no. , 1995.

44. S. Best, "Detection of residual stress in multi-crystalline silicon wafers using swept-sine frequency response data," Ph.D. dissertation, University of South Florida, 2005.

45. L. Starman and R. A. Coutu Jr., "Using micro-raman spectroscopy to assess MEMS Si/SiO_2," *Experimental Mechanics*, vol. 53, no. 4, April 2013.

46. C. Wilmsen, E. Thompson, and G. Meissner, "Buclking of thermally-grown Si/SiO_2 thin films," *IEEE Transactions on Electron Devices*, January 1972.

47. R. Mott, *Applied Stength of Materials.* Prentice Hall Inc., 1996.

48. (2015) Climate change is slowing our trains. [Online]. Available: http://digitalpicture.com.au/climate-change-slowing-trains/

49. O. Tabata, K. Kawahata, S. Sugiyama, and I. Igarashi, "Mechanical property measurements of thin films using load-deflection of composite rectangular membranes," *Sensors and Actuators*, vol. 20, 1989.

50. D. Maier-Schneider, J. Maibacj, and E. Obermeier, "A new analytical solution for the load-deflection of square membranes," *Journal of Microelectromechanical Systems*, vol. 4, no. 4, December 1995.

51. V. Ziebart, O. Paul, and H. Baltes, "Strongly buckled square micromachined membranes," *Journal of Microelectromechanical Systems*, vol. 8, no. 4, December 1999.

52. S. P. Timoshenko, *Theory of Elastic Stability.* McGraw-Hill, 1961.

53. D. S. Popescu, T. S. Lammerink, and M. Elwenspoek, "Buckled membranes for microstructures," in *Proc. IEEE Conference on Microelectromechanical Systems*, 1994.

54. R. Szilard, *Theories and Applications of Plate Analysis*, ed. Wiley, 2004.

55. D. GIancoli, *Physics for scientists and engineers.* Prentice Hall, 2009.

56. J. P. Baugher and R. A. Coutu Jr., "Microelectromechanical structure with stable linear positive and negative stiffness," in *MEMS and Nanotechnolgy*, ser. Conference Proceedings of the Society for Experimental Mechanics, vol. 4, 2011.

57. J. Almen and A. Laszlo, "The uniform-section disk spring," *Transactions of the American Society of Mechanical Engineers*, vol. 58, no. 10, 1936.

58. Belleville spring stiffness. [Online]. Available: http://www.shimrestackor.com/Physics/stack_stiffness/shim_stiffness/shim-stiffness.htm

59. Little known uses of bellville washers. [Online]. Available: http://www.bellevilleintl.com/2013/05/little-known-uses-of-belleville-washers

60. U.S. Department of the Interior: Facilities Engineering Branch, Denver Office. (2000) Facilities instructrions, standards, and techniques: Electrical connections for power circuits. [Online]. Available: http://www.usbr.gov/power/data/fist/fist3_3/vol3-3.pdf

61. B. Hansen, C. Carron, B. Jensen, A. Hawkins, and S. Schultz, "Plastic latching accelerometer based on bistable compliant mechanisms," *Smart Materials and Structures*, vol. 16, no. 5, 2007.

62. B. Hälg, "On a microelectromechanical nonvolatile memory cell," *IEEE Transactions on Electron Devices*, vol. 37, no. 10, 1990.

63. M. Freudenreich, U. Mescheder, and G. Somogyi, "Design considerations and realization of a novel micromechanical bi-stable switch," in *12th International Conference on Solid State Sensors, Actuators, and Microsystems*, Boston, June 2003.

64. N. Masters and L. Howell, "A self-retracting fully compliant bistable micromechanism," *Journal of Microelectromechanical Systems*, vol. 12, no. , 2003.

65. C. Lee and Y. Wu, "Study of electrothermal v-beam actuators and latched mechanism for optical switch," *Journal of Micromechanics and Microengineering*, vol. 15, no. 1, 2005.

66. R. Receveur, C. Marxer, R. Woering, V. Larik, and N. de Rooij, "Lateral moving bistable MEMS DC switch for biomedical applications," *Journal of Microelectromechanical Systems*, vol. 14, no. 5, 2005.

67. E. Kruglick and K. Pister, "Bistable MEMS relays and contact characterization," in *Solid-state Sensors and Actuators Workshop*, Cleveland, 1998.

68. T. Gomm, L. Howell, and R. Selfridge, "In-plane linear displacement bistable microrelay," *Journal of Micromechanics and Microengineering*, vol. 12, no. 3, 2005.

69. J. Qiu, J. Lang, and A. Slocum, "A bulk micromachined bistable relay with u-shaped thermal actuators," *Journal of Microelectromechanical Systems*, vol. 14, no. 5, 2005.

70. B. Wagner, H. J. Quenzer, S. Hoerschelmann, T. Lisec, and M. Juerss, "Bistable microvalve with pneumatically coupled membranes," in *9th Anual International Workshop on Microelectromechanical Systems*, 1996.

71. B. D. Jensen, L. L. Howell, and L. G. Salmon, "Design of two-link, in-plane, bistable compliant micro-mechanisms," *Transactions of the American Society of Mechanical Engineers*, vol. 121, September 1999.

72. D. Wilcox and L. L. Howell, "Fully compliant tensural bistable micromechanisms," *Journal of Microelectromechanical Systems*, vol. 14, no. 6, December 2005.

73. M. Schenk, J. L. Herder, and S. D. Guest, "Design of statically balanced tensegrity mechanism," in *Proc. of the ASME Design Engineering Technical Conference*, 2006.

74. L. Howell, *Compliant Mechanisms*. John Wiley and Sons, 2001.

75. K. Hoetmer, G. Woo, C. Kim, and J. herder, "Negative stiffness building blocks for statically balanced compliant mechanisms: Design and testing," *Journal of Mechanics and Robotics*, vol. 2, November 2010.

76. G. Chen and S. Zhang, "Fully-compliant statially balanced mechanisms without prestressing assembly: concepts and case studies," *Mechanical Sciences*, vol. 2, no. , 2011.

77. B. Li, G. Zhang, D. Yang, F. Hou, and Y. Hai, "The effect of diaphragm on performance of mems pressure sensor packaging," in *11th International Conference on Electronic Packaging Technology and High Density Packaging*.

78. T. Toriyama and S. Sugiyama, "Analysis of piezoresistance in p-type silicon for mechanical sensors," *Journal of Microelectromechanical Systems*, vol. 11, no. 5, 2002.

79. R. S. P. for Microsystems, "A. barlian, and w. park, and j. mallon, and a. rastegar, and b. pruitt," *Proceedings of the IEEE*, 2009.

80. M. Zarnik, D. Rocak, and S. Macek, "Resisdual stresses in a pressure sensor package induced by adhesive material during curing: a case study," *Sensors and Actuators A*, vol. 116, no. 3, 2004.

81. R. Krondorfer and Y. Kim, "Packaging effects on MEMS pressure sensor performance," *IEEE Transactions on Components and Packaging Technologies*, vol. 30, no. 2, 2007.

82. Measure laser power with a modified mems pressure sensor. [Online]. Available: http://www.radiolocman.com/review/article.html?di=148185

83. Pressure sensors for automotive and wireless boost mems market. [Online]. Available: http://www.siliconsemiconductor.net/article/77244-Pressure-sensors-for-automotive-and-wireless-boost-MEMS-market.php

84. W. S. Janna, *Engineering Heat Transfer*. CRC Press, 2009.

85. . [Online]. Available: http://www.atmosedu.com/meteor/images/HeatTransfer.jpg

86. S. Bouwstra, P. Kemna, and P. Legtenberg, "Thermally excited resonating membrane mass flow sensor," *Sensors and Actuators*, vol. 20, no. , 1989.

87. M. Chiao and L. Lin, "Self-buckling of micromachined beams under resistive heating," *Journal of Microelectromechanical Systems*, vol. 9, no. 1, 2000.

88. R. Coutu and S. Ostrow, "Microelectromechanical systems resistive heaters as circuit protection devices," *IEEE Transactions on Components, Packaging, and Manufacturing Technology*, vol. 3, no. 12, 2013.

89. M. Pecht, *Handbook of Electronic Package Design.* CRC Press, 1991.

90. M. Vangbo, "An analytical analysis of a compressed bistable buckled beam," *Sensors and Actuators*, vol. 69, 1998.

91. J. Qiu, J. H. Lang, and A. H. Slocum, "A curved-beam bistable mechanism," *Journal of Microelectromechanical Systems*, vol. 13, no. 2, April 2004.

92. J. Qiu, J. H. Lang, and A. H. Slocum, "A centrally-clamped parallel-beam bistable MEMS mechanism," in *The 14th IEEE International Conference on Microelectromechanical Systems*, 2001.

93. M. Taher and A. Saif, "On a tunable bistable MEMS - theory and experiment," *Journal of Microelectromechanical Systems*, vol. 9, June 2000.

94. M. Vangbo and Y. Backlund, "A lateral symmetrically bistable buckled beam," *Journal of Micromechanics and Microengineering*, vol. 8, 1998.

95. J. Qiu, J. H. Lang, A. H. Slocum, and R. Strumpler, "A high-current electrothermal bistable MEMS relay," in *16th Annual International Conference on Microelectromechanical Systems*, 2003.

96. J. Casals-Terre and A. Shkel, "Dynamic analysis of a snap-action micromechanism," in *Proc. of IEEE Sensors*, 2004.

97. M. Sulfridge, T. Saif, N. Miller, and M. Meinhart, "Nonlinear dynamic study of a bistable MEMS: Model and experiment," *Journal of Microelectromechanical Systems*, vol. 13, no. 5, October 2004.

98. B. Wagner, H. J. Quenzer, S. Hoerschelmann, T. Lisec, and M. Juerss, "Micromachined bistable valves for implantable drug delivery systems," in *18th Annual International Conference of the IEEE Engineering in Medicine and Biology Society*, 1996.

99. R. Arya, M. M. Rashid, D. Howard, S. D. Collins, and R. L. Smith, "Thermally actuated bistable oxide/silicon/metal membranes," *Journald of Micromachines and Microengineering*, vol. 16, 2006.

100. R. S. Lake, "Extreme damping in composite materials with a negative stiffness phase," *Physical Review Letters*, vol. 86, no. 13, March 2001.

101. D. L. Platus, "Negative stiffness mechanism vibration isolation systems," *SPIE: Vibration Control in Microelectronics, Optics, and Metrology*, vol. 1619, 1991.

102. C. M. Lee, V. N. Goverdovskiyand, and A. I. Temnikov, "Design of springs with negative stiffness to improve vehicle driver vibration isolation," *Journal of Sound and Vibration*, no. 302, 2007.

103. S. Hu, Z. Jin, H. Zhu, H. Wang, and M. Ma, "A slot-structured MEMS gyroscope working at atmosphere with tunable electrostatic spring constant," *Journal of Microelectromechanical Systems*, vol. 22, no. 4, August 2013.

104. E. H. Tay, R. Kumaran, B. L. Chua, and V. J. Logeeswaran, "Electrostatic spring effect on the dynamic performance of microresonators," Natinoal University of Singapore.

105. B. Yang, Y. Guan, S. Wang, Q. Zou, X. Chu, and H. Xue, "A new hybrid gyroscope with electrostatic negative stiffness tuning," *Sensors*, May 2013.

106. A. A. Ma'Radzi and B. Y. Majlis, "Non-crossing differential capacitive MEMS accelerometer with electrostatic spring tuning," in *IEEE International Conference on Semiconductor Electronics*, December 2006.

107. J. N. M. Hunter, C. Nachtsheim, *Applied Linear Regression Models.* McGraw-Hill, 2004.

108. University of Michigan: Lurie Nanofabrication Facility. (2015) Lnf wiki. [Online]. Available: http://ssel-sched.eecs.umich.edu/wiki/Public.MainPage.ashx

109. S. Lepi, *Practical Guide to Finite Elements.* Marcel Decker, 1998.

110. . [Online]. Available: http://mathworld.wolfram.com/RiemannSum.html

111. CoventorWare, *CoventorWare Analyzer Reference*, 2010.

112. K. K. Ziegler, "Selectively tuning a buckled Si/SiO_2 mems membrane through joule heating actuation and mechanical restriction," Master's thesis, Air Force Institute of Technology, 2014.

113. R. Lake, K. K. Ziegler, and R. Coutu Jr., "Thermal tuning of mems buckled membrane actuator stiffness," *Proc. 28th European Conference on Solid-State Transducers*, 2014.

114. R. Lake and R. Coutu Jr., "Tunable pressure sensing applications of a MEMS buckled membrane," in *Proc. 2015 IEEE National Aerospace and Electronics Conference.*

115. H. Stone, "Microfluidics: Tuned-in flow control," *Nature Physics*, 2009.

116. R. A. Lake and R. A. Coutu Jr., "Using cross-linked su-8 to flip-chip bond, assemble, and package mems devices," *IEEE Transactions on Components, Packaging, and Manufacturing Technology*, vol. 5, no. 3, 2015.

Vita

Captain Robert A. Lake was born and raised in Wakefield Massachusetts. He graduated from Bishop Fenwick High School in Peabody Massachusetts in 1999. He went on to earn his first undergraduate degree in engineering technology from Wentworth Institute of Technology where he graduated magna cum laude in 2003. He then went on to work in industry while earning his second undergraduate degree in electrical engineering from the University of Massachusetts, Lowell in 2008 where he graduated cum laude. While at U-Mass, he was a member of the university's Air Force ROTC detachment and received his commission as a second lieutenant in the Air Force in 2008.

Robert's first assignment upon commissioning was as a masters student at the Air Force Institute of Technology at Wright Patterson Air Force Base in Dayton Ohio where he studied electrical engineering with a concentration in solid state microelectronics and MEMS. His following assignment was at the Air Force Research Laboratory Space Vehicles Directorate at Kirtland Air Force Base in Albuquerque New Mexico. There he worked as a project manager for next generation, radiation hardened electronics. In 2012, Captain Lake returned to the Air Force Institute of Technology as a PhD student. He is a member of Tau Beta Pi and Eta Kappa Nu.

REPORT DOCUMENTATION PAGE

Form Approved
OMB No. 0704–0188

The public reporting burden for this collection of information is estimated to average 1 hour per response, including the time for reviewing instructions, searching existing data sources, gathering and maintaining the data needed, and completing and reviewing the collection of information. Send comments regarding this burden estimate or any other aspect of this collection of information, including suggestions for reducing this burden to Department of Defense, Washington Headquarters Services, Directorate for Information Operations and Reports (0704–0188), 1215 Jefferson Davis Highway, Suite 1204, Arlington, VA 22202–4302. Respondents should be aware that notwithstanding any other provision of law, no person shall be subject to any penalty for failing to comply with a collection of information if it does not display a currently valid OMB control number. **PLEASE DO NOT RETURN YOUR FORM TO THE ABOVE ADDRESS.**

1. REPORT DATE *(DD–MM–YYYY)*	2. REPORT TYPE	3. DATES COVERED *(From — To)*
09-17-2015	Doctoral Dissertation	Sept 2012 — Sept 2015

4. TITLE AND SUBTITLE

Novel Applications of a Thermally Tunable Bistable Buckling Silicon-on-Insulator (SOI) Microfabricated Membrane

5a. CONTRACT NUMBER

5b. GRANT NUMBER

5c. PROGRAM ELEMENT NUMBER

6. AUTHOR(S)

Robert A. Lake, Capt, USAF

5d. PROJECT NUMBER

5e. TASK NUMBER

5f. WORK UNIT NUMBER

7. PERFORMING ORGANIZATION NAME(S) AND ADDRESS(ES)

Air Force Institute of Technology
Graduate School of Engineering and Management (AFIT/EN)
2950 Hobson Way
WPAFB OH 45433-7765

8. PERFORMING ORGANIZATION REPORT NUMBER

AFIT-ENG-DS-15-S-013

9. SPONSORING / MONITORING AGENCY NAME(S) AND ADDRESS(ES)

10. SPONSOR/MONITOR'S ACRONYM(S)

11. SPONSOR/MONITOR'S REPORT NUMBER(S)

12. DISTRIBUTION / AVAILABILITY STATEMENT

DISTRIBUTION STATEMENT A. APPROVED FOR PUBLIC RELEASE; DISTRIBUTION UNLIMITED.

13. SUPPLEMENTARY NOTES

This material is declared a work of the U.S. Government and is not subject to copyright protection in the United States.

14. ABSTRACT

Buckled membranes are commonly used microelectromechanical systems (MEMS) structures. Recent work has demonstrated that the deflection and stiffness of these membranes can be tuned through localized joule heating. These devices were implemented into the design and fabrication of two novel device applications, a tunable pressure sensor and a steerable micromirror. A differential pressure across the membrane causes deflection, up or down, which can be measured and related to a specific pressure. By tuning the stiffness of the membrane, its pressure response is varied providing a wider range of application for the pressure sensor. A 2.0mm by 2.0mm square membrane demonstrated a 60 percent decrease in pressure sensitivity from 1.433m/psi to 0.55m/psi. A steerable micromirror was realized by selectively heating a single quadrant of a buckled membrane, localized heating results in membrane deflection constrained to that quadrant.

15. SUBJECT TERMS

MEMS, Buckled Membrane, Tunable Stiffness, Tunable Pressure Sensor

16. SECURITY CLASSIFICATION OF:			17. LIMITATION OF ABSTRACT	18. NUMBER OF PAGES	19a. NAME OF RESPONSIBLE PERSON
a. REPORT	b. ABSTRACT	c. THIS PAGE			Dr. Ronald A. Coutu, Jr.
U	U	U	U	174	19b. TELEPHONE NUMBER *(include area code)* (937) 255-3636, x7230; ronald.coutu@afit.edu